Compressive Response of Tapered Curved Composite Plates

Shaikh Mohammed Akhlaque-E-Rasul

A Thesis

in

The Department

of

Mechanical and Industrial Engineering

Presented in Partial Fulfillment of the Requirements

for the Degree of Doctor of Philosophy at

Concordia University

Montreal, Quebec, Canada

December 2010

CONCORDIA UNIVERSITY
SCHOOL OF GRADUATE STUDIES

This is to certify that the thesis prepared

By: Shaikh Mohammed Akhlaque-E-rasul

Entitled: Compressive Response of Tapered Curved Composite Plates

and submitted in partial fulfillment of the requirements for the degree of

complies with the regulations of the University and meets the accepted standards with respect to originality and quality.

Signed by the final examining committee:

Dr. Nawwaf Kharma, Dept. of Elect. & Comp. Eng. Chair

Dr. Ronald Gibson, Dept. of Mech. Eng., U. of Nevada-Reno External Examiner

Dr. M. Soleymani, Dept. of Elect. & Comp. Eng. External to Program

Dr. S. V. Hoa Examiner

Dr. M. Medraj Examiner

Dr. R. Ganesan Thesis Supervisor

Approved by

Chair of Department or Graduate Program Director

Dean of Faculty

ABSTRACT

Compressive Response of Tapered Curved Composite Plates

Shaikh Mohammed Akhlaque-E-Rasul, Ph.D.
Concordia University, 2010

Tapered laminated structures have considerable potential for creating significant weight savings in engineering applications. In the present thesis, the ply failure and global buckling failure of internally-tapered curved laminates are considered. For the buckling analysis, four different analytical approaches are employed: (1) classical shell theories using Ritz method, (2) first-order shear deformation shell theories using Ritz method, (3) linear finite element analysis based on first-order shear deformation shell theories, and (4) non-linear finite element analysis. Due to the variety of tapered curved composite plates and the complexity of the analysis, no closed-form analytical solution is available at present regarding their response to compressive loading. Therefore, the Ritz method is used for the global buckling analysis considering uniaxial compressive load. Linear buckling analysis of the plates is carried out based on eight classical shell theories and six first-order shear deformation shell theories. To apply the first-order shear deformation shell theories, an appropriate set of shear correction factors has been determined. The buckling loads obtained using Ritz method are compared with the existing experimental and analytical results, and are also compared with the buckling loads obtained using finite element method. The strength characteristics and load carrying capability of the tapered curved plates are investigated considering the first-ply failure and delamination failure.

The commercial software ANSYS® is used to analyze these failures. Based on the ply failure and buckling analyses, the critical sizes and parameters of the tapered curved plates that will not fail before global buckling are determined.

Linear buckling analysis is insufficient to take into account the effect of large deflections on the buckling loads. This effect can only be considered in the non-linear buckling analysis. However, very large number of load steps is required to determine the buckling load based on the non-linear analysis in which the stability limit load is calculated from the non-linear load-deflection curve. In the present thesis, a simplified methodology is developed to predict the stability limit load that requires the consideration of only two load steps. The stability limit loads calculated using the present simplified methodology are shown to have good agreement with that calculated from the conventional non-linear load-deflection curve.

Parametric studies are carried out using the above mentioned four different types of analytical methods. In these studies, the effects of boundary conditions, stacking sequence, taper configurations, radius, and geometric parameters of the plates are investigated.

ACKNOWLEDGMENTS

I would like to express my gratitude to all those who gave me the possibility to complete this thesis. First and foremost, I want to express my most sincere gratitude to my supervisor Dr. Rajamohan Ganesan, not only for his guidance in writing this thesis, but also for his advice, concern, patience, and encouragement during my study and research in Concordia University.

I would like to acknowledge the financial support provided to this work by the supervisor from his NSERC research grant.

I would like to tribute my late father, Professor Shaikh Moslem Uddin, for his encouragement to pursue my PhD degree.

Finally, I would also like to express my heartfelt appreciation to my wife, Doctor Shameema Chowdhury. Without her support and encouragement, this work would not have been possible.

TABLE OF CONTENTS

LIST OF FIGURES

LIST OF TABLES

CHAPTER 1

Introduction

1.1 GENERAL

Laminated composite structures are increasingly being used in many engineering applications due to their high specific stiffness and strength, low weight, and elastic tailoring design capabilities. In some specific applications the composite structure needs to be stiff at one location and flexible at another location. It is desirable to tailor the material and structural arrangements so as to match the localized strength and stiffness requirements by dropping the plies. Such a laminate is referred to as tapered laminate. Tapered laminated structures have received much more attention from researchers for creating significant weight savings in engineering applications. Complex structures like rotary blades, shovels, gun barrels and other taper-walled structures are frequently used and the loading conditions of these structures are complex in nature. The uniaxial compressive strength of fiber-reinforced polymer (FRP) composites is a very complex issue. Although FRP composites characteristically possess excellent ultimate and fatigue strength when loaded in tension in the fiber direction, compressive properties are typically not as good. This behavior is due to the fact that while tensile properties are fiber dominated, compressive properties are dependent upon other factors such as matrix modulus and strength, fiber/matrix interfacial bond strength, and fiber misalignment. An example of tapered plate under compressive load is shown in the Fig. 1.1.

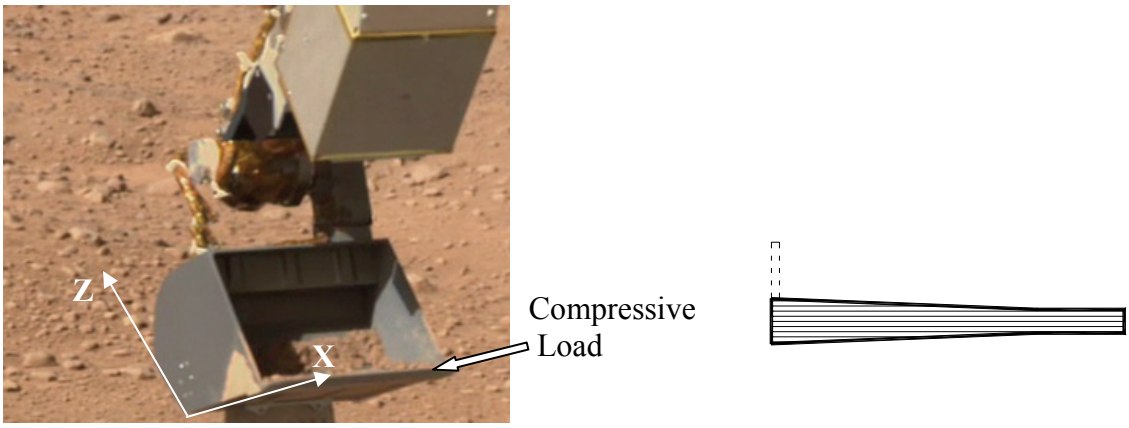

(a) Shovel of Phoenix Mars Lander (b) Cross section along X-axis

Figure 1.1: A simple application and loading condition of tapered plate.

Changes in the geometry of a structure or a mechanical component under compression result in the corresponding loss of its ability to resist loading. The behavior of structures under compression can be grouped into two main categories: (1) instability associated with a bifurcation of equilibrium or a limit point, and (2) local failure that is associated with material failure. The first category is called buckling. The point of transition from the usual deflection mode under load to an alternative deflection mode is referred to as the point of bifurcation of equilibrium. The lowest load at the point of bifurcation is called critical bifurcation buckling load. The second category can further be divided into two for a composite structure: ply failure and failure due to interface delamination. The above mentioned behavior of structures can be called as Type-I, Type-II and Type-III failures, which are caused by buckling, ply failure and delamination respectively. The failure types and the corresponding analyses are shown in the Fig. 1.2.

In the Fig. 1.2 two types of buckling are mentioned, that are, linear and non-linear. One major characteristic of non-linear buckling, as opposed to linear buckling (bifurcation buckling), is that non-linear buckling (snap through buckling) phenomenon includes a region of instability in the post-buckling region whereas linear buckling only involves linear, pre-buckling behavior up to the bifurcation (critical loading) point. In Fig. 1.3, the stability limit point is the non-linear buckling load. The linear buckling load is larger than that of the non-linear buckling load, because the equations for the strains of non-linear theory have more non-linear terms compared to the linear theory. The comparison of linear and non-linear buckling loads is given in the chapter five of the present thesis. Fig. 1.3 shows the differences between linear and non-linear buckling wherein F denotes the force and u denotes the deflection.

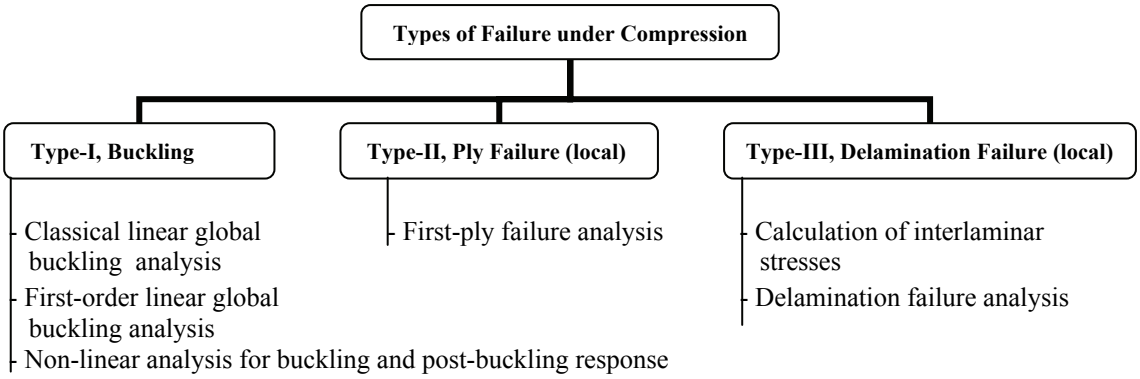

Figure 1.2: Different types of failure of tapered curved plates under compressive load and corresponding analyses.

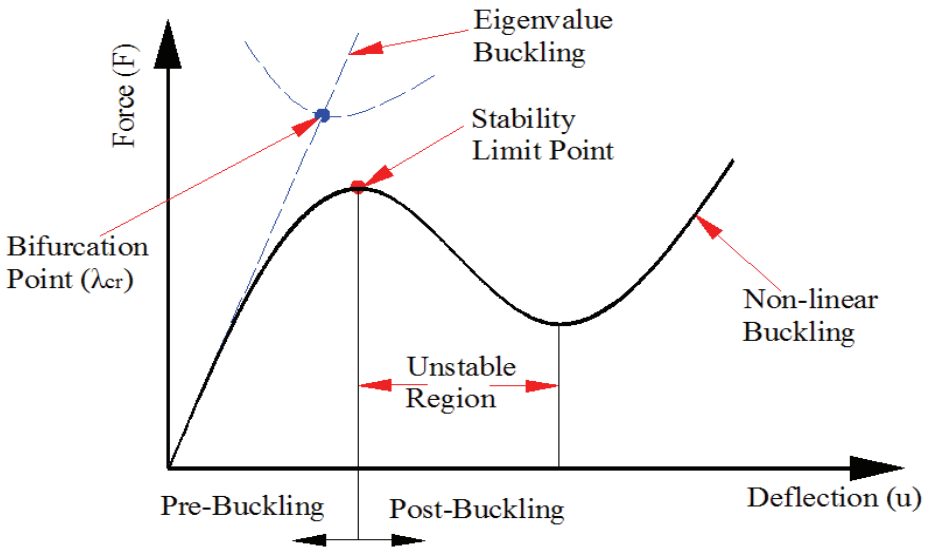

Figure 1.3: Non-linear versus linear buckling behavior.

1.2 LITERATURE REVIEW

In the following, a review of existing works on the i) analysis of tapered composite structures, ii) linear buckling analysis of shells, iii) analysis of shells using Ritz method, vi) buckling analysis of shells using finite element method, v) first-ply failure analysis of composite structures, vi) interlaminar stress and delamination failure analyses of composite structures, vii) non-linear buckling analysis of shells, and viii) prediction of critical load, is given.

1.2.1 Analysis of Tapered Composite Structures

A review of recent developments in the analysis of tapered laminated composite structures with an emphasis on interlaminar stress analysis, delamination analysis and parametric study has been presented by He et al [1]. From earlier research works concerning this type of structure, two major categories of work on tapered composites

can be identified. The first is to understand failure mechanisms encompassing the determination of the interlaminar stresses in the vicinity of ply drop-off, the calculation of strain-energy release rate associated with delamination within the tapered region, and the direct modeling of delamination progression by using finite elements. A large number of investigators have been engaged in conducting research on this subject. The list includes the works of Curry et al [2] and Hoa et al [3]. The second category is the investigations of the parameters of the tapered composite structures that have substantial influences on the structural integrity. Parametric studies of tapered composites were conducted by Daoust and Hoa [4], Llanos and Vizzini [5], and Thomas and Webber [6].

A limited number of scientists have conducted research on tapered composite curved plates. Piskunov and Sipetov [7] have proposed a laminated tapered shell structure which accounts for the effects produced by transverse shearing strain. They have developed a shearing strain model to minimize the differences between the physicomechanical parameters (the values of the elasticity modulus, the shear modulus, the Poisson ratio, the thermal conductivity coefficient, the linear expansion coefficient, etc.) of the composite layers. Another work on tapered laminated shell structure was conducted by Kee and Kim [8], where the rotating blade is assumed to be a moderately thick, width-tapered in longitudinal direction and open cylindrical shell that includes the transverse shear deformation and rotary inertia, and is oriented arbitrarily with respect to the axis of rotation to consider the effects of disc radius and setting angle. The finite element method is used for solving the governing equations.

1.2.2 Linear Buckling Analysis of Shells

A brief history of shell buckling is discussed by Lars and Eggwertz [9]. Euler's formulae for determining the critical load of a compressed straight bar were published in the middle of the 18th century. The theory was further developed during the latter half of the 19th century, when the stability of thin plates was also analyzed in an analogous way, Lars and Eggwertz [9]. A theory of shell buckling was first proposed in the beginning of the 20th century, by Lorenz [10] and Timoshenko [11], who presented solutions for axially compressed circular cylindrical shells. Ambartsumyan [12] has pioneered the anisotropic thin shell analysis and he has also considered the local stability and vibration in his formulations. Viswanathan et al [13] investigated elastic stability of thin laminated, flat and curved, long rectangular plates subjected to combined in-plan loads. Hilburger and Starnes [14] have worked on buckling behavior of compression-loaded composite thin cylindrical shells with reinforced cutouts. Michael [15] has presented non dimensional parameters and equations for buckling of symmetrically laminated thin elastic shallow shells.

R. C. Tennyson [16] has conducted a brief review on static buckling theory for both geometrically perfect and imperfect anisotropic composite circular thin cylinders for various loading configurations. For comparison purposes, relevant experimental data are discussed, including combined loading test results and recommendations are made concerning the design of composite cylinders. A review work on the problem of buckling of uniform-thickness and moderately-thick, laminated, composite shells subjected to destabilizing loads has been carried out by Simitses [17]. The loads consist of uniform

axial compression, uniform lateral pressure and torsion applied individually or in combination. The analysis is based on higher-order shear deformation (HOSD) shell theory and/or first-order shear deformation (FOSD) shell theory with or without a shear correction factor. Recommendations are also given for the moderately thick laminated shells to check the failure strength, delamination initiation and growth and their effect on the critical buckling loads.

1.2.3 Analysis of Shells Using Ritz Method

The problems of mechanics are solved by exact analytical methods, or approximate methods (energy methods, variational methods, numerical methods). First preference is given to exact solution; if it is not possible due to complexity of the structure then 'approximate analytical or numerical solutions' are used. The variational methods of approximation include those of Rayleigh and Ritz, Galerkin, Petrov-Galerkin (weighted-residuals), Kantorovich and the Finite Element Method (numerical method) which is a "piecewise" application of the Ritz and Galerkin methods. Analytical solutions such as Ritz solutions are of growing interest among scientists.

Buragohain and Velmurugan [18] have developed an energy-based smeared stiffener model (SSM) to obtain equivalent stiffness coefficients of a composite lattice cylindrical thin shell with hexagonal lattice patterns. Using the equivalent stiffness coefficients, buckling analysis is carried out using Ritz method. Extensive finite element modeling covering different sizes have also been carried out to compare the buckling results with that of the Ritz method. Wong et al [19] have developed an analytical model using Ritz

method for the instability of orthotropic thin composite tubes subject to biaxial compressive loads under clamped-clamped boundary conditions. Six E-glass woven fabric-epoxy composite tubes with the same internal radius and different thicknesses and longitudinal lengths were fabricated and subjected to various combinations of external hydrostatic pressure and axial compressive load simultaneously. They have concluded that the buckling envelopes in normalization form provide useful design data on the strength of orthotropic composite tubes under a realistic range of biaxial loading conditions.

Rao and Meyer-Piening [20] have conducted the buckling analysis of a simply supported and uniform-thickness fiber reinforced plastic (FRP) faced cylindrical anisotropic sandwich panel subjected to combined action of axial compression and bending and shear using the Rayleigh-Ritz method. The values of the buckling coefficient are evaluated by varying the aspect ratio, fiber orientation angle, core-to-face thickness ratio, radius of cylindrical edge, bending load coefficient and shear load coefficient. Jaunky and Knight [21] have obtained buckling loads of uniform-thickness circular cylindrical composite panels using Sanders-Koiter's, Love's and Donnell's shell theories with first-order shear-deformation approach and Rayleigh-Ritz method that accounts for different boundary conditions and material anisotropy. Results obtained using the shell theories are compared with those obtained from finite element simulations, where the curved panels are modeled using nine node quadrilateral continuum based shell elements that are independent of any shell theory. The authors have compared the results obtained using Ritz method with that of the finite element method and have concluded that Donnell's

theory could be in error for some lamination schemes and geometrical parameters. Barai and Durvasula [22] have studied the vibration and the buckling of uniform-thickness and simply-supported curved plates, made of hybrid (Graphite/epoxy, Kevlar/epoxy and Glass/epoxy) laminated composite materials, using first-order shear deformation theory and Reissner's shallow shell theory. The natural frequencies and critical buckling loads are calculated using Ritz method. The effects of curvature, aspect ratio, stacking sequence and ply-orientation are studied.

1.2.4 Buckling Analyses of Shells Using Finite Element Method

Since the time of mid-1960s when the curved shell finite elements were invented, the published literature on modeling of plates and shells analysis of structures has grown extensively. In the last four decades, numerous theoretical models have been developed and applied to various practical circumstances. It may be reasonable to state that no single theory has proven to be general and comprehensive enough for the entire range of applications. The pros and cons of different finite elements have been evaluated by the several reviewers. Yang et al [23] have reviewed the advances of the formulations for thin shell finite elements in the form of flat plates, axisymmetrical shells and curved shells. They also illustrated with some extensions and applications to cases such as static and dynamic responses, static and dynamic bucklings, laminated composites, random loadings and random structural and material properties. The review work of Kapania [24] deals with the development of various theories of modeling the thick laminated shells, development of various finite elements to model these shells, buckling and post-buckling analyses of perfect and imperfect laminated shells, and vibration and dynamic response

analyses of various laminated shells. Gilewski [25] has surveyed about 350 publications related to the finite element models of moderately thick shells, concentrating on those related to consistent displacement and stress/mixed/hybrid models. Noor and Burton [26] have assessed the computational models for multilayered composite shells. In their work, they have listed several references on finite element analysis of shells. Reddy and Robbins [27] have presented a review work on equivalent-single-layer and layerwise laminated plate theories, and their finite element models. Mackerle [28] has surveyed the linear and non-linear, static and dynamic analyses of structural elements; his listed papers have been published between 1992 and 1995. Yang et al [29] have summarized the important literature on shell finite elements over 15 years (1985-2000). Their survey includes the degenerated shell approach, stress-resultant-based formulations and Cosserat surface approach, reduced integration with stabilization, incompatible modes approach, enhanced strain formulations, 3-D elasticity elements, drilling degree of freedom elements, co-rotational approach, and higher-order theories for composites.

Nine-node shell elements have advantages compared to eight-node elements. Nine-node elements can pass the constant curvature patch test with bilinear element geometry while eight-node shell elements cannot. A comparative study between these two types of elements has been carried out by MacNeal and Harder [30]. Parisch [31] has discussed special aspects of the nine-node Lagrange element. A modification of the stiffness is proposed which allows the application of the element like a Kirchhoff-type model to any plate problem. A case study of a variety of proposed element models is presented, and the accuracy is shown for various plate and shell problems. Belytschko et al [32] have

described the implementation of a nine-node Lagrange element with uniform reduced quadrature and spurious mode control for plates and shells. They have compared their results with that of full integration and selective reduced integration versions of the element. Lee and Hobbs [33] have suggested an automatic adaptive refinement procedure for the analysis of shell structures using the nine-node degenerated solid shell element. Chang et al [34] have examined a nine-node Lagrange shell element using a strain-based mixed method. Kebari and Cassell [35] have presented a nine-node degenerate stress-resultant shell element with six degrees of freedom at each node. Yeom et al [36] have combined a nine-node shell element based on the assumed displacement formulation and an eight-node shell element based on a modified version of the Hellinger-Reissner principle with assumed linear transverse shear strain in order to eliminate locking . The results of their analysis are compared with the classical thin plate theory and other reference solutions. Jayasankar et al [37] have extended a nine-node degenerated shell element developed earlier for stress analysis to the free vibration analysis of thick laminated composites. In the present thesis work, a nine-node Lagrange shell element is used.

MacNeal [38] has examined the cause of failure of finite elements and its remedy. It includes quantitative analyses of failure modes and illustrations of possible side effects found in proposed remedies, providing a practical understanding of finite element performance. This book is designed to enable users and practitioners to identify and circumvent the major flaws of finite elements, such as locking, patch-test failure, spurious modes, rigid-body failure, induced anisotropy and shape sensitivity. Chapellet

and Bathe [39] have presented fundamental considerations regarding the finite element analysis of shell structures.

1.2.5 First-ply Failure Analysis of Composite Structures

Reddy and Pandey [40] have developed finite-element computational procedure for the first-ply failure analysis of composite plates. The procedure is based on the first-order shear deformation theory and a tensor polynomial failure criterion that contains the maximum stress, maximum strain, Hill, Tsai-Wu and Hoffman failure criteria. According to their conclusions, all failure criteria that they have analyzed are equivalent in predicting the failure when laminates are subjected to in-plane loads. For laminates subjected to transverse load, the maximum strain and Tsai-Hill criteria predict different failure location. Tsai [41] has compared the popular failure criteria of fiber-reinforced composite materials. These criteria are empirical and should only be judged from the standpoint of the fitness to data and the ease of application. The criteria for orthotropic plies of unidirectional composites are extensions of those for isotropic materials. The quadratic criteria are considered to be the most suitable for both isotropic and composite materials. Macroscopic criteria are essential for design and for providing guidelines for materials improvements. He has concluded that the failure criteria for multidirectional laminates are valid up to the first-ply failure (before transverse cracking and delamination occur). Nahas [42] has reviewed the existing theories of failure of laminated fiber-reinforced composite materials. He has mentioned that there exist at least 30 failure theories for laminated composites. Some of these theories are applied directly to the laminate while the rest of the theories are applied to the individual layers of the laminate.

In addition, he has reviewed the theories of the post-failure behavior of laminated composites, that is, the behavior of laminated composites beyond first-ply failure. For post-failure analysis there exist at least twelve theories, which are included in his survey. The World-Wide Failure Exercise (WWFE) contained a detailed assessment [43] of 19 theoretical approaches for predicting the deformation and failure response of polymer composite laminates when subjected to complex states of stress. The leading five theories (Zinoviev, Bogetti, Puck, Cuntze and Tsai) are explored in greater detail to demonstrate their strengths and weaknesses in predicting various types of structural failure. According to the investigations of WWFE, Tsai-Wu theory is the best one that can be used to predict the first-ply failure of unidirectional laminates and any of the above mentioned five failure theories can be used for multidirectional laminates. In the present thesis work, Tsai-Wu failure theory is used to predict the first-ply failure of tapered curved plates.

1.2.6 Interlaminar Stress and Delamination Failure Analyses of Composite Structures

Interlaminar stress analysis can be divided into four distinct categories: considering an isotropic thin resin layer at the middle of two plies, analytical solutions obtained from equilibrium equations, numerical solutions and layerwise theory. Mortensen [44], He et al [45], and Fish and Lee [46] have analyzed the laminates using embedded resin layer. Analytical solutions include the works of Kassapoglou [47], and Waltz and Vinson [48]. Pipes and Pagano [49] have employed finite-difference solution techniques for interlaminar stresses in the composite laminates under uniform axial extension. Results for material properties typical of a high modulus graphite-epoxy composite material

system are presented which explain the mechanism of shear transfer within a symmetric laminate. Curry [50], and Ganesan and Liu [51] have carried out the investigation of interlaminar stresses using finite element method. To accurately calculate the in-plane and transverse stresses, without integrating the equilibrium equations, Reddy's [52] layerwise theory can be used. Kant and Swaminathan [53] have reviewed the different methods used for the estimation of transverse/interlaminar stresses in laminated composite plates and shells. Both analytical and numerical methods are considered. The aspects considered by them are: effects of variation in geometric and material parameters, transverse shear and normal deformation, interface stress continuity and the interfacial bonding on the accuracy of prediction of transverse/interlaminar stresses. Salamon [54] has presented a review and assessment of the interlaminar delamination problem common to layered composite materials. The work covers calculation of interlaminar stresses from a homogeneous and microstructural material viewpoint. The observation of edge delamination and experimental efforts are discussed together with the fracture mechanics studies.

A large-size defect, or stress concentration is the primary cause of delamination. The manufacturing errors or in-service and accidental loads lead to the delamination of the laminates. Dropped plies result in an abrupt change of thickness and produce a concentration of stresses which may cause delamination as explained by Curry [50]. The Compression After Impact (CAI) refers to the sequence of events whereby a low velocity transverse impact on a composite plate may also be the cause of internal delaminations. When the plate is subsequently loaded by in-plane compression, local buckling may

occur around these delaminations, reducing the residual compressive strength of the plate. Publications focusing on the after-impact evaluation and on the after-impact repair of damaged structures are reviewed by Resnyansky [55]. Bolotin [56] has distinguished two kinds of delaminations, depending on their position in a structural member. Delaminations situated within the bulk of the material are rather like the cracks studied in conventional fracture mechanics. The edge delaminations in thick members may also be partially attributed to this type of delamination. Delaminations situated near the surface of a structural member are a special kind of crack-like defect. The behavior of surface delaminations is accompanied by their buckling. The local instability and crack growth may produce the global instability of structural components such as columns, plates and shells under compression. Therefore, he suggested the joint analysis of damage, fracture, local buckling and global stability to predict the load-carrying capacity of composite structures with delaminations. Bolotin [57] has surveyed the literature and the mechanical aspects of delaminations in laminate composite structures. He discussed the surface and internal delaminations of various origin, shape and location. He also analyzed the origination, stability, and post-critical behavior of delaminations under quasi-static, cyclic, and dynamic loads.

In the present thesis work, interlaminar stresses are analyzed using the two methods: considering an isotropic thin resin layer at the middle of two plies and numerical solutions. Using the later, the origination of delamination, if any, is analyzed. But the local instability and crack growth are not considered in the present analyses. Considering the above mentioned isotropic thin resin layer, transverse interlaminar normal and shear

stresses developed at the locations of the ply drop-off are also calculated to see the stress state at those locations.

1.2.7 Non-linear Buckling Analysis of Shells

Linearized formulations are insufficient to explain and to account for many important phenomena such as the effect of large deformations, amplitude-dependent frequency, the catastrophic jump phenomena, subharmonic oscillations, and post-buckling behavior of structures. In large-deflection (non-linear) theory, the deflections are assumed to be finite though small. They are relatively large, however, when compared with that of small-deflection theory. The strain-displacement relations include non-linear terms and therefore the equilibrium equations in terms of displacements are non-linear in nature. Donnell and Wa [58], in their approximate analysis of the effects of initial imperfections on the buckling behavior of compressed cylinders, derived a set of large-deflection equilibrium equations which is an extension of that derived by Von-Karman [59] for large deflections of flat plates. Donnell and Wa [58] are the first to suggest a simple non-linear theory for analyzing the stability of cylindrical shells.

Two distinct approaches have been followed in the literature in developing non-linear finite element analysis of laminated structures: i) laminate theory and ii) 3-D continuum formulation. In the laminate theory, the 3-D description is reduced to a 2-D description based on the assumption of small strains and moderate rotations, no change of geometry during loading, and the geometric non-linearity is in the form of Von-Karman strains. Analysis based on this theory can be found in the Ref. [60]. In the 3-D continuum

formulation full non-linear strains or only the Von-Karman non-linear strains are included as desired. There are two incremental continuum formulations that are used to determine the deformation and stress states: a) the total Lagrangian formulation in which the Green-Lagrange strain tensor and 2nd Piola-Kirchhoff stress tensor are used, and b) the updated Lagrangian formulation in which the Cauchy stress tensor and the infinitesimal Almansi strain tensor are used. Liao and Reddy [61] and Reddy [62] have investigated shell structures using 3-D continuum formulation. In the present thesis work, laminate theory is used in the formulation of non-linear buckling analysis.

In the literature five types of solution methods have commonly been used to solve the non-linear problems of shell theory: i) The small parameter method, ii) The successive approximation method, iii) the Picard iteration (or direct iteration) method, iv) the Newton-Raphson iteration method, and v) the Riks method (or the incremental/iterative solution method). The small parameter method was used by Kayuk [63-64]. The successive approximation method was used by Vorovich [65-66] in the non-linear shell theory to prove the solvability of boundary value problems. To the iteration algorithms used in the vicinity of regular shell states belong the Newton and Raphson methods [67-68], which are based on the idea of linearization [69] in which one constructs a linearized operator at each iterative step. The convergence of Newton's method depends to a large extent on how successfully the initial approximation of the deformation matrix has been selected. This method was used in the Refs. [70] and [71] to solve the problems of shell theory. Application of Newton-Raphson method to complex structural systems has been carried out by Haeseler and Peitgen [72]. Originally and independently Riks [73] and

Wempner [74] proposed the earliest version of arc-length method. This arc-length method is also known as incremental/iterative solution method. Based on the conventional arc-length method, an improved arc-length method was proposed by Zhu and Chu [75]. Bruce and Siegfried [76] have introduced a general formulation for all arc-length procedures. They have also compared their results with that of the Crisfield's procedure [77]. Concerning the incremental strategies to solve the non-linear set of algebraic equations, a new arc-length-type method was formulated by Carrera [78]. In this work, he has compared the various types of path-following methods: the load control, the displacement control, and the arc-length-type methods. In the present non-linear analyses, the Crisfield's procedure [77] is applied.

To investigate the non-linear deformation and stability of shell structures, it is convenient to apply the Bubnov-Galerkin method [79]. Its implementation in the non-linear shell stability problems has been discussed by Vol'mir [80]. Karman and Tsien [81] implemented the non-linear statement of the problem for smooth cylindrical shells by using the Donnell's equations. The review studies related to further development of stability investigations are contained in the monographs of Vol'mir [80] and Grigolyuk and Kabanov [82]. Riks [83] and Ramm [84] have given an overview of different path-following methods with a broad literature review. Sze et al [85] have presented popular benchmark problems for geometric non-linear analysis of shells wherein eight sets of popularly employed benchmark problems were proposed and solved. Andrade et al [86] have formulated and implemented an eight-node hexahedral isoparametric element with one-point quadrature for the geometrically non-linear static and dynamic analysis of

plates and shells made of composite materials. Han et al [87] have presented the formulation of a non-linear composite nine-node modified first-order shear deformable element-based Lagrangian shell element for the solution of geometrically non-linear analysis of laminated composite thin plates and shells. Pradyumna et al [88] have employed a higher order finite element formulation for the non-linear transient analysis of functionally graded curved panels.

1.2.8 Prediction of Critical Load

Three types of buckling loads were defined by Chang and Chen [89], and Li [90]. These three types of buckling loads include, i) the classical buckling load (the bifurcation point or linear buckling load) of an ideal linear elastic structure, ii) the linearized buckling load, and iii) fully non-linear buckling load. The basic assumption of the linearized buckling analysis is that the structure behaves linearly before the critical load is reached. The linearized buckling load is estimated on a stressed structure under a certain load and considering the singularity of the tangent stiffness matrix. The details of the calculation of linearized buckling load are explained in the book of Bathe [91]. The fully non-linear buckling analysis employs a non-linear static analysis with gradually increasing loads to seek the load level at which the structure becomes unstable which is known as the stability limit load (snap through buckling). There have been few studies into the effectiveness of the above-mentioned different types of buckling loads. Batdorf [92] first idealized the cylindrical shell structure by neglecting the pre-buckling rotation and the hoop stress and calculated the critical stress for the axially loaded cylinders. Croll [93] has estimated the lower bound for the critical loads of cylindrical shells by neglecting the strain energy due to membrane action of the structure. Brush [94] has considered the

effect of pre-buckling rotations and improved the Batdorf's approximation [92]. Li [90] has assumed the linear relation of load-displacement in pre-buckling state. He has also presented a survey of concepts and methods that have been used in the non-linear analysis of instability and collapse of structures. Almroth and Brogan [95] have discussed the practical applicability of the bifurcation buckling theory. Several example cases were presented in which results from a bifurcation buckling analysis were compared to the results obtained from a rigorous non-linear analysis.

An improved scheme for critical load prediction has been developed by Brendel and Ramm [96] using the total Lagrangian formulation. Based on their methodology, Chang and Chen [89] combined the linear buckling loads with the loads obtained based on the minimum number of non-linear analyses to predict the critical loads of shell structures. They have estimated stability limit load by predicting and using the various linearized critical loads corresponding to respective pre-stress loads (in their analysis a pre-stress load is considered as the base load). In the present work, an improved methodology for the prediction of stability limit load is developed that requires the consideration of only two load steps instead of several load steps as in the case of existing methodology.

1.3 OBJECTIVES OF THE THESIS

None of the previously mentioned authors has worked on the response characteristics of tapered curved composite plates under compression. In the present thesis work, this response is considered for the purpose of studying the fundamental behavior of tapered curved composite plates. On the other hand, a large number of load steps are required to

calculate the stability limit load from the conventional non-linear load-deflection curve. A simplified methodology is introduced using two load steps to calculate the stability limit load of a curved plate.

In the present thesis work, the buckling response of curved laminated plates with longitudinal internal ply-drop-off configuration is investigated. Longitudinal ply-drop-off tapers are identified as those in which the internal discontinuities of the laminate are parallel to the direction of the applied load. Taking account the findings of He et al [1], and Daoust and Hoa [4], different types of longitudinal cross sections as shown in Fig. 1.4 are investigated. In the Fig. 1.4, h_{tk} and h_{tn} denote the thicknesses at the thick end and thin end respectively; L_{tk}, L_{tap} and L_{tn} denote the lengths of thick, taper and thin section respectively; R, b and b' denote the radius, the width and the cord of curved plates respectively; and (u_o, v_o, w_o) denotes the mid-plane displacement field with reference to the global coordinate system (x, y, z). The taper configuration A is a simplified taper configuration having only one large resin pocket. The taper configuration B has five resin pockets: four small resin pockets are distributed symmetrically with respect to mid-plan and the fifth one is designed combining the two small resin pockets. Every small resin pocket is formed by dropping-off three composite plies and there are continuous composite plies above and below each resin pocket. The hybrid configuration is modeled combining the uniform-thickness and tapered sections as shown in the Fig. 1.4.

The first objective of the present thesis work is to conduct the linear global buckling analysis of the tapered curved plates shown in Fig. 1.4 using Ritz method. Linear global

buckling analysis includes the classical and first order shear deformation shell theories. For the buckling analysis based on classical shell theory, namely Donnell's, Love's, Mushtari's, Timoshenko's, Vlasov's, Sander's, Koiter's and Novozhilov's theories are used. Six shell theories are used in the analysis based on first-order shear deformation theory, namely Donnel's, Love's, Moreley's, Loo's, Sander's and Koiter's theories. The relative efficiency and accuracy of these shell theories are assessed based on critical buckling loads obtained using Ritz method and finite element method. Buckling analysis results obtained using Ritz method are compared with the existing experimental and analytical results, and are also evaluated with that of the results obtained using ANSYS. *The second objective* is to determine the failure loads corresponding to local material failure of the tapered curved plates using ANSYS®. The first-ply failure load is calculated considering the first instance at which any layer or more than one layer fails at the same load. The initiation of delamination, if any, is analyzed using the transverse interlaminar stresses under compressive load. *The third objective* is to determine the critical sizes and parameters of the tapered curved plates based on the failure and buckling analyses. *The fourth objective* is to evaluate the stability limit load and ultimate strength of the tapered curved plate beyond the initial buckling. The mechanical structures undergo large deflection after they buckle. The effect of large deflection is considered in the non-linear analysis. A simplified methodology for non-linear buckling analysis is introduced to find out the stability limit load which requires only two load steps instead of large number of load steps. Non-linear buckling analysis is carried out using FEM. *A parametric study* that encompasses the effects of boundary conditions, stacking sequence, taper

configurations, radius and other geometric parameters of the plate is conducted. *Finally*, design guidelines for the tapered curved composite plates are established.

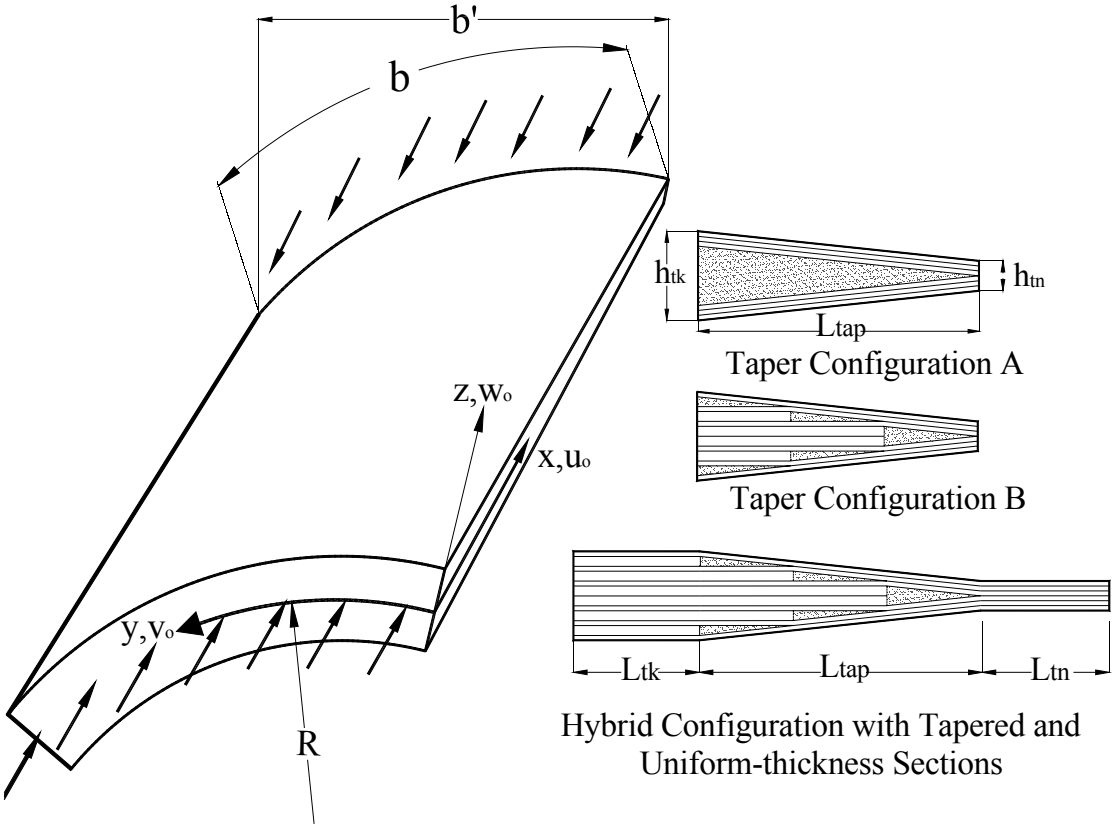

Figure 1.4: Different longitudinal cross sections of curved plate.

1.4 LAYOUT OF THE THESIS

In the present chapter, a general discussion about the compressive strength of tapered curved composite plates, literature review on the a) analysis of tapered composite structures, b) linear buckling analysis of shells, c) analysis of shells using Ritz method, d) buckling analysis of shells using finite element method, e) first-ply failure analysis of composite structures, f) interlaminar stress and delamination failure analyses of composite structures, g) non-linear buckling analysis of shells, and h) prediction of

critical load, objectives of the present thesis, and finally, the layout of the present thesis, are given.

In chapter two, the Ritz method and eight classical shell theories are used for the global linear buckling analysis of thickness-tapered curved composite plates subjected to uniaxial compressive load. The results that obtained using Ritz method are compared with that of the existing studies. Finally, a parametric study is carried out.

In chapter three, the Ritz method is used for the global buckling analysis based on six first-order shear deformation shell theories. To apply the first-order shear deformation shell theories to analyze the plates, an appropriate set of shear correction factors have been determined. The critical sizes and parameters of the tapered curved plates that will not fail before global buckling are determined. At the end, a parametric study is accomplished.

In chapter four, a nine-node tapered curved finite element is developed based on six first-order shear deformation shell theories. To apply the first-order shear deformation shell theories to analyze the tapered plates, an appropriate set of shear correction factors have been determined. Various boundary conditions are considered for different laminate and lay-up configurations. The buckling loads obtained using FEM are also compared with that of the existing experimental and analytical results. At the end, a parametric study is concluded.

In chapter five, non-linear buckling analysis is carried out using finite element method. To find out the stability limit load, a simplified methodology is introduced which requires only two load steps. Three types of plates are analyzed: uniform curved, tapered curved and hybrid (uniform and tapered) curved plates.

In chapter six, conclusions, a summary of contributions, and suggestions for the future work are given.

Chapter 2

Compressive Response of Thickness-Tapered Shallow Curved Composite Plates Based on Classical Shell Theory

2.1 INTRODUCTION

In this chapter, the compressive response of shallow curved composite plates with longitudinal internal ply-drop-off configurations is investigated. The Ritz method is used for the global buckling analysis considering uniaxial compressive load. Linear buckling analysis is carried out based on eight well-known classical shallow shell theories, namely Donnell's, Love's, Mushtari's, Timoshenko's, Vlasov's, Sander's, Koiter's and Novozhilov's theories. The strength characteristics and load carrying capability of the tapered curved plates are investigated considering the first-ply failure analysis using ANSYS®. Based on the failure and buckling analyses, the critical sizes and parameters of the tapered curved plates that will not fail before global buckling are determined. A parametric study is conducted that encompasses the effects of boundary conditions, stacking sequence, taper configurations, radius, and geometric parameters of the plates.

2.2 FORMULATION

Total potential energy criterion is used in order to analyze the stability problems. The curved plates of the Fig. 1.4 are considered to conduct the buckling analysis. Resin pockets are assumed to be the combination of hypothetical resin plies. Following assumptions are considered in the buckling analyses:

- The plate consists of arbitrarily laminated composite layers.
- Material is homogeneous and elastic.
- The plate is thin, shallow (h_{tk} / R « 1) and has no imperfection.

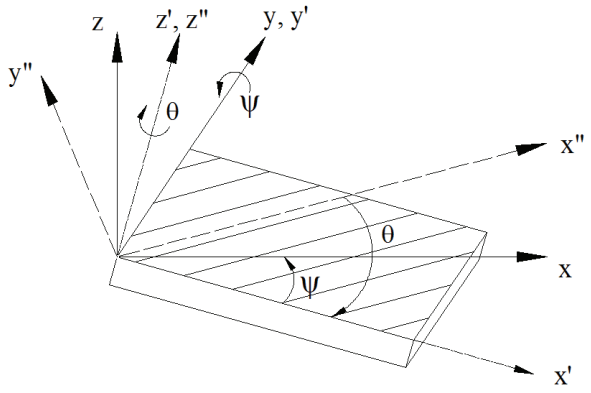

Figure 2.1: Orientation of fibers and laminate

The tracer coefficients c_1, c_2, c_3 and c_4 are introduced to implement the eight different shell theories for shallow curved plates. The strain-displacement functions for different theories can be applied in the case of small deformations with the displacement fields (u_o, v_o, w_o) that refer to the global coordinate system (x, y, z) as shown in Fig. 2.1:

$$[\varepsilon_{xx}, \varepsilon_{yy}, \gamma_{xy}]^T = [\varepsilon^o_{xx}, \varepsilon^o_{yy}, \gamma^o_{xy}]^T + z[\kappa_{xx}, \kappa_{yy}, \kappa_{xy}]^T \tag{2.1}$$

with

$$\begin{Bmatrix} \varepsilon^o_{xx} \\ \varepsilon^o_{yy} \\ \gamma^o_{xy} \end{Bmatrix} = \begin{Bmatrix} \dfrac{\partial u_o}{\partial x} \\ \dfrac{\partial v_o}{\partial y} + \dfrac{w_o}{R} \\ \dfrac{\partial u_o}{\partial y} + \dfrac{\partial v_o}{\partial x} \end{Bmatrix} \tag{2.2}$$

and

$$\begin{Bmatrix} \kappa_{xx} \\ \kappa_{yy} \\ \kappa_{xy} \end{Bmatrix} = \begin{Bmatrix} -\dfrac{\partial^2 w_o}{\partial x^2} \\ -\dfrac{\partial^2 w_o}{\partial y^2} - \dfrac{c_1}{R^2} w_o + \dfrac{c_2}{R}\dfrac{\partial v_o}{\partial y} \\ -2\dfrac{\partial^2 w_o}{\partial x \partial y} + \dfrac{1}{R}\left(c_3 \dfrac{\partial v_o}{\partial x} - c_4 \dfrac{\partial u_o}{\partial y} \right) \end{Bmatrix} \tag{2.3}$$

where $[\varepsilon^0_{xx}, \varepsilon^0_{yy}, \gamma^0_{xy}]^T$ and $[\kappa_{xx}, \kappa_{yy}, \kappa_{xy}]^T$ are the mid-surface strains and curvatures respectively. The superscript '*T*' stands for transpose of the matrix.

By setting,

i) $c_1 = c_2 = c_3 = c_4 = 0$, equations that correspond to Donnel's [97], Mushtari's [97], Timoshenko's [97] and Love's [98] shell theories are obtained.

ii) $c_1 = c_3 = c_4 = 1$ and $c_2 = 0$, equations that correspond to Vlasov's [99] shell theory is obtained.

iii) $c_1 = c_2 = 0$ and $c_3 = c_4 = 1/2$, equations that correspond to Sander's [100] and Koiter's [101] shell theories are obtained.

iv) $c_1 = c_4 = 0$, $c_2 = 1$ and $c_3 = 2$, equations that correspond to Novozhilov's [102] shell theory is obtained.

The Fig. 2.1 describes the orientation of fibers and laminate. x'', y'' *and* z'' are the principal material directions oriented by θ (fiber orientation angle) degrees with respect to the x', y' *and* z' directions respectively. The local coordinate system (x', y', z') makes an angle of ψ (taper angle) degrees with the global coordinate system (x, y, z).

Hooke's law for orthotropic materials in the principal material directions can be written as:

$$\begin{Bmatrix} \sigma_{x''x''} \\ \sigma_{y''y''} \\ \sigma_{z''z''} \\ \tau_{y''z''} \\ \tau_{x''z''} \\ \tau_{x''y''} \end{Bmatrix} = \begin{bmatrix} C''_{11} & C''_{12} & C''_{13} & 0 & 0 & 0 \\ C''_{12} & C''_{22} & C''_{23} & 0 & 0 & 0 \\ C''_{13} & C''_{23} & C''_{33} & 0 & 0 & 0 \\ 0 & 0 & 0 & C''_{44} & 0 & 0 \\ 0 & 0 & 0 & 0 & C''_{55} & 0 \\ 0 & 0 & 0 & 0 & 0 & C''_{66} \end{bmatrix} \begin{Bmatrix} \varepsilon_{x''x''} \\ \varepsilon_{y''y''} \\ \varepsilon_{z''z''} \\ \gamma_{y''z''} \\ \gamma_{x''z''} \\ \gamma_{x''y''} \end{Bmatrix} \tag{2.4}$$

where σ''_{ij} and τ''_{ij} are the normal stresses and shear stresses respectively and, ε''_{ij} and γ''_{ij} are the normal strains and shear strains respectively with i, j = x'', y'', z'' in the material coordinate system (x'', y'', z''). $C''_{11}, C''_{12} ....etc$ are the corresponding stiffness coefficients.

Eq. (2.4) can be expressed as:

$$\{\sigma''\} = [C'']\{\varepsilon''\} \tag{2.5}$$

The stress transformation matrix due to fiber orientation angle θ is of the following form [103]:

$$[T_{\sigma\theta}] = \begin{bmatrix} \cos^2\theta & \sin^2\theta & 0 & 0 & 0 & -2\cos\theta\sin\theta \\ \sin^2\theta & \cos^2\theta & 0 & 0 & 0 & 2\cos\theta\sin\theta \\ 0 & 0 & 1 & 0 & 0 & 0 \\ 0 & 0 & 0 & \cos\theta & \sin\theta & 0 \\ 0 & 0 & 0 & -\sin\theta & \cos\theta & 0 \\ \cos\theta\sin\theta & -\cos\theta\sin\theta & 0 & 0 & 0 & \cos^2\theta - \sin^2\theta \end{bmatrix} \tag{2.6}$$

The stress transformation matrix due to taper angle ψ can be written as:

$$[T_{\sigma\psi}] = \begin{bmatrix} \cos^2\psi & 0 & \sin^2\psi & 0 & 2\cos\psi\sin\psi & 0 \\ 0 & 1 & 0 & 0 & 0 & 0 \\ \sin^2\psi & 0 & \cos^2\psi & 0 & -2\cos\psi\sin\psi & 0 \\ 0 & 0 & 0 & \cos(\psi) & 0 & -\sin\psi \\ -\cos\psi\sin\psi & 0 & \cos\psi\sin\psi & 0 & \cos^2\psi - \sin^2\psi & 0 \\ 0 & 0 & 0 & \sin\psi & 0 & \cos\psi \end{bmatrix} \tag{2.7}$$

The elastic properties of a layer are given in its principal material directions by the Eq. (2.4) but the final form of the governing equations are in the global coordinate system

(x,y,z). The layer properties should be transformed to global directions from the principal material directions as follows:

--First, coordinate transformation corresponding to the rotation of x" and y" about z" axis (see Fig. 2.1)

--Second, coordinate transformation corresponding to the rotation of x' and z' about y' axis (see Fig. 2.1)

Therefore, the stress tensor for a ply in the tapered laminate is formulated as:

$$\{\sigma\} = [T_{\sigma\psi}][T_{\sigma\theta}][C''][T_{\sigma\theta}]^T [T_{\sigma\psi}]^T \{\varepsilon\} \tag{2.8}$$

where $[T_{\sigma\theta}]$ and $[T_{\sigma\psi}]$ are the stress transformation matrices due to fiber orientation angle θ and taper angle ψ respectively.

The above equation can be expressed in a short form:

$$\{\sigma\} = [C]\{\varepsilon\} \tag{2.9}$$

Thus, the stiffness matrix [C] in the global coordinate system (x, y, z) can be expressed by the stiffness matrix [C"] in the principal material coordinate system (x'', y'', z'') and the transformation matrices as:

$$[C] = [T_{\sigma\psi}][T_{\sigma\theta}][C''][T_{\sigma\theta}]^T [T_{\sigma\psi}]^T \tag{2.10}$$

The reduced stiffness matrix is in the form:

$$\begin{Bmatrix} \sigma_{xx} \\ \sigma_{yy} \\ \tau_{xy} \end{Bmatrix} = \begin{bmatrix} Q_{11} & Q_{12} & Q_{16} \\ Q_{12} & Q_{22} & Q_{26} \\ Q_{16} & Q_{26} & Q_{66} \end{bmatrix} \begin{Bmatrix} \varepsilon_{xx} \\ \varepsilon_{yy} \\ \gamma_{xy} \end{Bmatrix} \tag{2.11}$$

where, $Q_{ij} = C_{ij} - C_{i3}\, C_{j3} / C_{33}$, $i, j = 1,2,6$ (2.12)

and C_{ij} is the coefficient of material stiffness matrix in the global coordinate system given by the Eq. (2.10).

The equations for coefficients of matrices [A], [B] and [D] for tapered laminate can be written as

$$(A_{ij}, B_{ij}, D_{ij}) = \int_{-h/2}^{h/2} Q_{ij}(1, z, z^2)dz \qquad \text{i , j = 1,2,6} \tag{2.13}$$

In which, A_{ij} is the stretching stiffness matrix coefficient, B_{ij} is the coupling stiffness matrix coefficient, D_{ij} is the bending stiffness matrix coefficient, and Q_{ij} is calculated from the Eq. (2.12).

The strain energy of the tapered shell structure is written in Cartesian co-ordinates as follows:

$$\Pi = \frac{1}{2}\int_0^b \int_0^{L_{tap}} \left\{ [\varepsilon]^T \begin{bmatrix} A & B \\ B & D \end{bmatrix} [\varepsilon] \right\} dxdy \tag{2.14}$$

where $[\varepsilon] = [\varepsilon_{xx}^0, \varepsilon_{yy}^0, \gamma_{xy}^0, \kappa_{xx}, \kappa_{yy}, \kappa_{xy}]^T$ (2.15)

The potential energy due to the uniaxial compression is [104]:

$$F = -\lambda \int_0^b \int_0^{L_{tap}} \left\{ \frac{\partial u_o}{\partial x} + \frac{1}{2}\left[\left(\frac{\partial v_o}{\partial x} \right)^2 + \left(\frac{\partial w_o}{\partial x} \right)^2 \right] \right\} dxdy \tag{2.16}$$

where, λ is the inplane normal compressive load in x direction.

The approximate solutions for the displacements are expressed as a double series:

$$u_o(x, y) = \sum_{m=1}^{M} \sum_{n=1}^{N} U_{mn} U_m(x) U_n(y) \tag{2.17}$$

$$v_o(x, y) = \sum_{m=1}^{M} \sum_{n=1}^{N} V_{mn} V_m(x) V_n(y) \tag{2.18}$$

$$w_o(x, y) = \sum_{m=1}^{M} \sum_{n=1}^{N} W_{mn} W_m(x) W_n(y) \tag{2.19}$$

The functions $U_m(x)$, $U_n(y)$, $V_m(x)$, $V_n(y)$, $W_m(x)$, and $W_n(y)$ are so chosen as to satisfy the boundary conditions which are given in the Appendix A and the coefficients U_{mn}, V_{mn} and W_{mn} are determined by the following stationary conditions:

$$\frac{\partial \Pi}{\partial U_{mn}} = \frac{\partial F}{\partial U_{mn}} \tag{2.20}$$

$$\frac{\partial \Pi}{\partial V_{mn}} = \frac{\partial F}{\partial V_{mn}} \tag{2.21}$$

$$\frac{\partial \Pi}{\partial W_{mn}} = \frac{\partial F}{\partial W_{mn}} \tag{2.22}$$

where Π and F are given by the Eqs. (2.14) and (2.16) respectively.

The Eqs. (2.20) through (2.22) are, respectively, rewritten as:

$$\begin{bmatrix}[L_{IJ}^{11}] & [L_{IJ}^{12}] & [L_{IJ}^{13}]\end{bmatrix}\begin{Bmatrix}U_{IJ}\\ V_{IJ}\\ W_{IJ}\end{Bmatrix} = -\lambda\begin{bmatrix}[0] & [0] & [0]\end{bmatrix}\begin{Bmatrix}U_{IJ}\\ V_{IJ}\\ W_{IJ}\end{Bmatrix} \tag{2.23}$$

$$\begin{bmatrix}[L_{IJ}^{12}] & [L_{IJ}^{22}] & [L_{IJ}^{23}]\end{bmatrix}\begin{Bmatrix}U_{IJ}\\ V_{IJ}\\ W_{IJ}\end{Bmatrix} = -\lambda\begin{bmatrix}[0] & [G_{IJ}^{22}] & [0]\end{bmatrix}\begin{Bmatrix}U_{IJ}\\ V_{IJ}\\ W_{IJ}\end{Bmatrix} \tag{2.24}$$

$$\begin{bmatrix}[L_{IJ}^{13}] & [L_{IJ}^{23}] & [L_{IJ}^{33}]\end{bmatrix}\begin{Bmatrix}U_{IJ}\\ V_{IJ}\\ W_{IJ}\end{Bmatrix} = -\lambda\begin{bmatrix}[0] & [0] & [G_{IJ}^{33}]\end{bmatrix}\begin{Bmatrix}U_{IJ}\\ V_{IJ}\\ W_{IJ}\end{Bmatrix} \tag{2.25}$$

Eqs. (2.23) through (2.25) are rearranged into matrix form:

$$\begin{bmatrix}[L_{IJ}^{11}] & [L_{IJ}^{12}] & [L_{IJ}^{13}]\\ [L_{IJ}^{12}] & [L_{IJ}^{22}] & [L_{IJ}^{23}]\\ [L_{IJ}^{13}] & [L_{IJ}^{23}] & [L_{IJ}^{33}]\end{bmatrix}\begin{Bmatrix}U_{IJ}\\ V_{IJ}\\ W_{IJ}\end{Bmatrix} = -\bar{\lambda}\begin{bmatrix}[0] & [0] & [0]\\ [0] & [G_{IJ}^{22}] & [0]\\ [0] & [0] & [G_{IJ}^{33}]\end{bmatrix}\begin{Bmatrix}U_{IJ}\\ V_{IJ}\\ W_{IJ}\end{Bmatrix} \tag{2.26}$$

Further details about the matrices $[L_{IJ}^{11}]$, $[L_{IJ}^{12}]$, $[G_{IJ}^{22}]$, $[G_{IJ}^{33}]$, and so on are given in the Appendix A. The eigenvalues $\bar{\lambda}$ are the values of buckling loads. The following indicial expressions were introduced [105] and used in Eq. (2.26):

$$I = (m-1)M + n \quad \text{and} \quad J = (i-1)N + j \tag{2.27}$$

where $i, m = 1,2.....M$ and $j, n = 1,2.....N$.

Eq. (2.26) can be written in the short form:

$$\left|[K] + \bar{\lambda}[Z]\right| = 0 \tag{2.28}$$

where, [K] and [Z] are the stiffness matrix and geometric stiffness matrix respectively.

Eq. (2.28) is solved using MATLAB® program as an eigenvalue problem for which the eigenvalues $\bar{\lambda}$ are the values of buckling loads. The smallest value of $\bar{\lambda}$ is the critical buckling load, λ_{cr}.

2.3 VALIDATION

To the author's knowledge, no results are available yet in the literature on the buckling loads of the tapered curved composite plates under the action of uni-axial compression. Therefore the comparison with the existing works could not be made. In order to validate the formulation and analysis, first, the taper angle is set to be zero, and the resulting uniform-thickness laminates have been analyzed and the results have been compared with that available in the literature for the uniform-thickness laminates. For this purpose, a uniform-thickness cylindrical panel made of Morganite II/4617 having the mechanical properties of $E_{x"}$ =137.89 x10^9 Pa (20.0 x10^6 psi), $E_{y"}$ = 14.48 x10^9 Pa (2.1 x10^6 psi), $G_{x"y"}$ = 5.86 x 10^9 Pa (0.85x10^6 psi), $\upsilon_{x"y"}$ = 0.21 and the geometrical properties of length L = 0.3048 m (12 inches), width b = 0.2032 m (8 inches), radius R = (0.3048 - h/2) m, thickness h = 1.50368 x 10^{-03} m (0.0592 inches) and taper angle ψ = 0 degree which has been investigated by Wilkins [106] is considered. The plate is clamped at four edges (C4-C4) and the boundary conditions (C4-C4) are given in the Appendix A. In the work of

Wilkins [106], experiments were carried out applying the experimental procedures of Southwell (S) and Moiré (Mo). Results of the present work are compared with that of the Ref. [106] for different laminate configurations in the Tables 2.1 and 2.2.

From the Table 2.1 it is found that the result is converged when 9 terms are taken in the Ritz series. Most of the buckling problems in the present work have converged with 9 terms. The results based on different shell theories are close to each other but the Novozhilov's theory provides the most conservative result. As can be seen from Tables 2.1 and 2.2, the present analytical results differ from that of the experimental ones with a maximum error of 15.9 percent, which is nominal for a linear buckling analysis.

Table 2.1: The comparison of buckling load of uniform-thickness cylindrical panel

Laminate Configurat-ion	No. of Terms in the Series (N x M)	Wilkins [106] ($x10^4$ N/m)	Present ($x\ 10^4$ N/m)			
			Donnell, Love, Doubly, Mushtari, Timoshenko	Vlasov	Sander, Koiter	Novozhilov
		Exp.	Ritz Solution	Ritz Solution	Ritz Solution	Ritz Solution
$[0/90]_{2s}$	1x1	15.5162 (S)	634.6769	633.2735	634.5210	632.3378
	2x2		118.0114	117.7504	117.9824	117.5764
	3x3		20.6453	20.5996	20.6402	20.5692
	4x4		18.5656	18.5246	18.5611	18.4972
	5x5		18.1300	18.0899	18.1255	18.0632
	6x6		17.8980	17.8584	17.8936	17.8320
	7x7		17.8629	17.8234	17.8585	17.7971
	8x8		17.8235	17.7841	17.8191	17.7578
	9x9		17.8191	17.7797	17.8148	17.7535

Table 2.2: The comparison of buckling loads for uniform-thickness cylindrical panel of different configurations

Laminate Configuration	Wilkins [106] ($x\ 10^4$ N/m)	Present, Novozhilov ($x\ 10^4$ N/m)
	Exp.	Ritz Solution
$[0/45/90/-45]_s$	15.5425 (Mo)	15.9825
$[0]_{6s}$	47.1485 (S)	54.6658

Next, uniform-thickness cylindrical panel made of T300/5208 graphite/epoxy having the mechanical properties of $E_{x"} = 141.34$ GPa (20.5 x10^6 psi), $E_{y"} = 8.96$ GPa (1.3 x10^6 psi), $G_{x"y"} = 5.17$ GPa (0.75 x10^6 psi) and $\upsilon_{x"y"} = 0.335$ which is clamped (C3) in transverse direction and simply supported (S3) in longitudinal direction is considered. The boundary conditions (C3-S3) are given in the Appendix A. The dimensions of the plate are taken to be: length L = 0.3048 m (12 inches), the cord length $b^{'} = 0.3048$ m, radius of the plate R = 0.3048 m, thickness h = 1.016x10^{-03} m (0.04 inches). Becker [107] has conducted the bifurcation (obtained from eigenvalue solution) buckling analysis of this curved plate using STAGS computer code. In the present study, the buckling analysis is carried out using Ritz method based on various shell theories and the results are compared with that given in the work of Becker [107]. The normalized buckling load is given in the Table 2.3 where λ_{cr} is the critical buckling load.

Table 2.3: The comparison of buckling loads of uniform-thickness curved plates applying different shell theories

Laminate Configuration	Becker [107] $(\lambda_{cr}L^2)/(E_{x"}h^3)$		Present $(\lambda_{cr}L^2)/(E_{x"}h^3)$			
	Theory	Exp.	Donnell, Love, Doubly Mushtari, Timoshenko	Vlasov	Sander, Koiter	Novozhilov
$[90/0]_{2s}$	33.30	24.50	34.950	34.866	34.949	34.816

As can be observed from the Table 2.3, the present result is in good agreement with the theoretical buckling load given in the reference work. The present results are higher than that of the experimental results. According to Ref. [107], the bifurcation buckling loads may be 23 to 45 percent higher than the experimental buckling results because the occurrence of elastic instability is strongly influenced by the geometric nonlinearity,

geometric imperfections and the boundary conditions in the orthotropic laminates [16]. The results based on different shell theories are close to each other and the Novozhilov's theory provides the most conservative result which is also observed from Table 2.1. Hence in the present chapter, the Novozhilov's theory is used to calculate the buckling load using Ritz method.

Further, a tapered plate with only two internally dropped plies has been analyzed using Ritz method based on Novozhilov's theory. The mechanical properties and the dimensions are same as the last mentioned problem (Ref. [107]) and the clamped-simply supported (C3-S3) boundary conditions are considered. The results are compared with that of two uniform-thickness composite plates with lay-up configurations $[90/0]_{2s}$ and $[90/0/90]_s$, respectively. The buckling loads for these three laminates under uni-axial compressive load are given in Table 2.4. As can be observed, the result for tapered laminate is between that of the 8-layers uniform-thickness laminate and that of the 6-layers uniform-thickness laminate.

Table 2.4: Critical buckling loads for tapered and uniform-thickness composite plates

Plate	Critical Buckling Load (x 10^4 N/m)
8-Layers Uniform Plate $[90/0]_{2s}$	5.5532
Tapered Plate $[90/0]_{2s}$ - $[90/0/90]_s$	4.0214
6-Layers Uniform Plate $[90/0/90]_s$	2.9161

2.4 FIRST-PLY FAILURE ANALYSIS

The load carrying capability of the tapered curved plates is studied considering first-ply failure load. This type of failure analysis is considered in the present work to determine whether a layer has failed due to compressive loading before global buckling. The commercial software ANSYS® has been chosen to model the curved composite plates. Element SHELL99 is used for the first-ply failure analysis using ANSYS®. SHELL99 is an 8-node, 3-D shell element with six degrees of freedom (three translations and three rotations) at each node. It is designed based on the degenerated solid approach with shear deformation effect and to model thin to moderately-thick plate and shell structures with a side-to-thickness ratio of roughly 10 or greater. The tapered curved plates are meshed by eighty-one elements which are shown by numbering in the Fig. 2.2. The first-ply failure analysis is carried out using ANSYS® based on the 3-D version of Tsai-Wu failure criterion. The first-ply failure refers to the first instant at which any layer or more than one layer fails at the same load. The same criterion is applied for both the composite ply and the resin pocket, the resin pocket is considered (imagined) to be made up of layers of isotropic resin material. Material properties [45] of composite ply and epoxy are given in the Tables 2.5 and 2.6 respectively, where X^t, Y^t, Z^t are the normal tensile strengths in the principal material directions $x", y", z"$ respectively; R_{yz}, S_{xz}, T_{xy} are the shear strengths in the $y"z"$, $x"z"$, $x"y"$ planes respectively; X^c, Y^c, Z^c are the normal compressive strengths in the principal material directions $x", y", z"$ respectively.

Table 2.5: Material properties of NCT/301 graphite-epoxy composite material

Mechanical Property	Value	Strength Property	Value
$E_{x''}$	113.900 GPa	X^t	1621 MPa
$E_{y''} = E_{z''}$	7.985 GPa	X^c	-1250 MPa
$G_{x''y''} = G_{x''z''}$	3.137 GPa	$Y^t = Z^t$	48.28 MPa
$G_{y''z''}$	2.852 GPa	$Y^c = Z^c$	-200 MPa
$\nu_{x''y''} = \nu_{x''z''}$	0.288	R_{yz}	25.00 MPa
$\nu_{y''z''}$	0.400	$S_{xz} = T_{xy}$	33.30 MPa

Table 2.6: Material properties of epoxy material used in NCT/301

Mechanical Property	Value	Strength Property	Value
$E_{x''} = E_{y''} = E_{z''}$	3.930 GPa	$X^t = Y^t = Z^t$	57.00 MPa
$G_{x''y''} = G_{x''z''} = G_{y''z''}$	1.034 GPa	$X^c = Y^c = Z^c$	-104 MPa
$\nu_{x''y''} = \nu_{x''z''} = \nu_{y''z''}$	0.370	$R_{yz} = S_{xz} = T_{xy}$	22 MPa

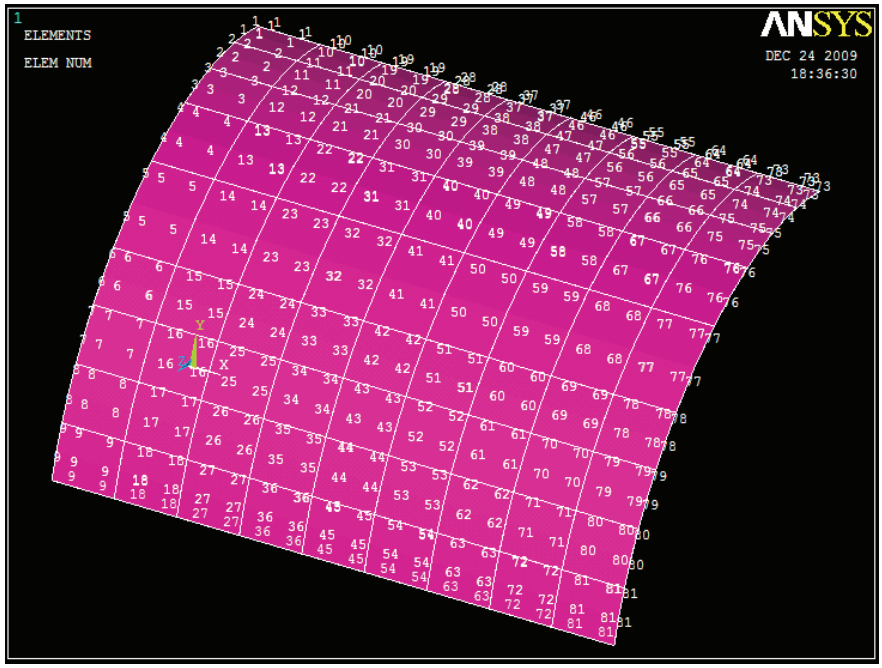

Figure 2.2: Finite element mesh.

Four different sizes of square tapered composite plates with taper configuration B and made of NCT/301 graphite-epoxy composite material is considered. The lay-up is $[0/90]_{9s}$ at the thick end and $[0/90]_{3s}$ at the thin end which is defined as lay-up

configuration LC_1 in the Table 2.7. The mechanical properties of the composite and epoxy material are given in Tables 2.5 and 2.6 respectively. The geometric properties of the plates are: side length of the square plates varies from 85.9 to 859.4 mm, plate thickness at thick end h_{tk} = 4.5 mm and the radius R = 500 mm. The clamped-clamped (C4-C4) boundary conditions given in the Appendix A are considered. The results of failure analysis are tabulated in the Table 2.8.

Table 2.7: List of lay-up configurations

Lay-up Configuration	Ply Staking Sequence			Lengths of the Hybrid Configuration (m)		
	Thick Section	Tapered Section	Thin Section	Thick Section	Tapered Section	Thin Section
LC_1	$[0/90]_{9s}$	Config. B	$[0/90]_{3s}$	0.0382	0.1146	0.0382
LC_2	$[\pm45]_{9s}$	Config. B	$[\pm45]_{3s}$	0.0382	0.1146	0.0382
LC_3	$[0_2/\pm45_8]_s$	Config. B	$[0_2/\pm45_2]_s$	0.0382	0.1146	0.0382

Table 2.8: Critical buckling load and first-ply failure load of tapered curved laminates with lay-up configuration LC_1 and taper configuration B

Taper Angle in Degree	Side Length of the Square Plate (m)	Buckling Load Using Ritz Method (x 10^4 N/m)	First-ply Failure Load Using ANSYS® (x 10^4 N/m)	Failure Location (FEN, FLN)*
0.10	0.8594	14.20	48.05	1, 2
0.50	0.1719	43.81	42.00	1, 2
0.75	0.1146	70.69	43.50	9, 3
1.00	0.0859	100.23	45.60	9, 3

* FEN and FLN denote the failed element number and failed layer number at first-ply failure.

The side length of square plates corresponding to taper angles is given in the Table 2.8. The first-ply failure loads are compared with the buckling loads. As can be seen from the

Table 2.8, the tapered curved plates corresponding to taper angles of 0.50, 0.75 and 1.0 degrees will fail by first-ply failure before the global buckling. On the other hand, the plate corresponding to taper angle of 0.1 degree will fail first by buckling failure. Therefore, the maximum plate size should be (0.1754 x 0.1754) which is corresponding to taper angle of 0.49 degree and the critical length-to-height ratio (L_{tap} / h_{tk}) is to be 38.9. The failed layer numbers 2 and 3, respectively, are the second layer and the third layer at the thick end of the plates. All the tapered curved plates failed at the thick end where the minimum numbers of plies above or below the resin pockets.

Next, the tapered plates of the Table 2.8 are analyzed for different radii using the same boundary conditions (C4-C4), ply-configuration (LC_1) and material properties (Table 2.5 and Table 2.6). The critical sizes of the tapered curved plates are determined corresponding to various radii. For the calculation of critical length-to-height ratio, the same procedure is applied as mentioned in the previous problem for the radius of 500 mm. In the Fig. 2.3, radius versus critical length-to-height ratio of tapered curved plates is plotted. In this figure, L_{tap} denotes the taper length and h_{tk} denotes the thickness at the thick end. The stiffness of the tapered curved plate increases with the decrease of radius. Therefore, critical length-to-height ratio is to be increased with the decrease of radius to avoid the material failure. It can also be seen in the Fig. 2.3 that the critical length-to-height ratio increases with the decrease of radius. The critical length-to-height ratio varies non-linearly with the change of radius. The design limit of the tapered curved composite plates with the lay-up configuration LC_1 and the taper configuration B is determined and represented as the hatched area in the Fig. 2.3. Beyond this limit, tapered curved plate

with lay-up configuration LC_1 and taper configuration B will not fail by first-ply failure before global buckling.

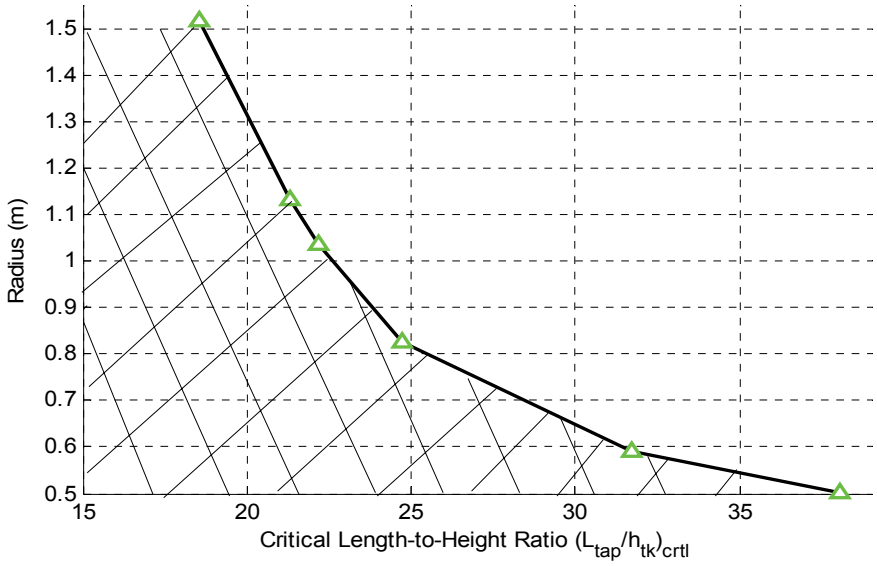

Figure 2.3: The effect of critical length-to-height ratio on radius of the tapered curved composite plates with the ply configuration LC_1 and the taper configuration B.

2.5 PARAMETRIC STUDY

In the parametric study two types of longitudinal cross-sections of the curved plates are considered, that are, taper configurations A and B and hybrid configuration as shown in the Fig. 1.4. The buckling analyses are carried out using Ritz method based on Novozhilov's theory. The material properties of composite ply and epoxy that are the same as given in the Tables 2.5 and 2.6 respectively are used.

2.5.1 Buckling Analyses of Tapered Curved Plates

Tapered models shown in the Fig. 1.4 are considered with 36 and 12 plies at thick and thin ends respectively, which results in 24 drop-off plies. The configuration at the thick

end is $(0/90)_{9s}$, and that of the thin end is $(0/90)_{3s}$; this lay-up configuration is defined as LC_1. In the analyses of taper configurations, the height of thick end h_{tk} = 4.5 mm and the radius of curved plate R = 500 mm are considered. For the analyses of tapered curved plates only LC_1 ply-configuration with clamped-clamped (C4-C4) boundary conditions are considered. Various parameters, namely ply drop-off, taper angle and length-to-radius ratio are investigated to see the effects of these parameters on buckling load of tapered curved plates. The results are shown in the following Figs. 2.4 through 2.6.

2.5.1.1 Influence of Ply Drop-Off

The effect of ply drop-off on critical buckling load is shown in the Fig. 2.4. To investigate this effect, the side length of square tapered plate is considered as 859.4 mm corresponding to taper angle of 0.1 degree. The thickness of the thick end is not changed and the taper angle is varied with the corresponding increase in the number of drop-off plies. The plate can be considered as a uniform-thickness plate when the number of ply drop-off is set to zero and the taper configuration A is obtained by dropping-off twenty four plies. The plates are clamped-clamped (C4-C4) at four edges and the lay-up configuration is LC_1. In the Fig. 2.4, λ_{cr} denotes the critical buckling load.

From the Fig. 2.4, it is observed that the uniform-thickness curved plate is stiffer than the uniform-thickness flat plate in terms of buckling behavior. It is also observed that the tapered flat plate is less stiff than uniform flat, but this behavior of the plate can be inverted if the tapered flat plate is made into a curved one. Buckling load of flat and curved plates varies linearly with the drop-off plies. It can be concluded from the Fig. 2.4 that the tapered flat plate is more flexible than uniform flat plate, but the tapered curved

plate provides a better design option in terms of saving the material without any compromise of the strength. Similar type of conclusions can also be made for other types of taper configurations.

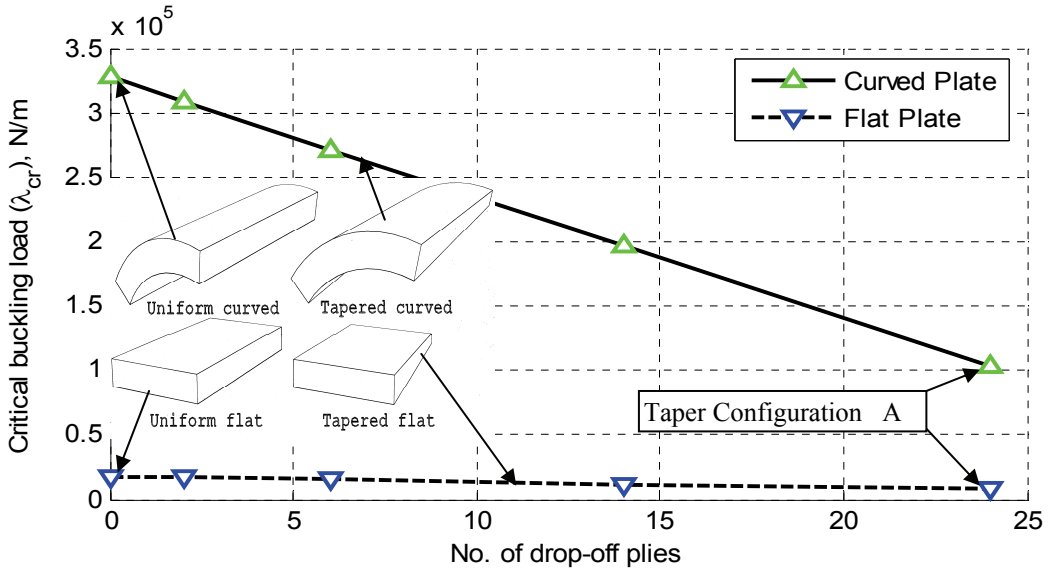

Figure 2.4: The effect of ply drop-off on buckling load for clamped-clamped (C4-C4) plates.

2.5.1.2 Influence of Taper Angle

The effect of taper angle on buckling load of tapered curved plates using Ritz method is compared with the two different taper configurations, A and B. The comparison is shown in the Fig. 2.5 where the size of the plate is decreased with the increase of taper angle while keeping the thickness of thick section unchanged. The maximum and minimum edge lengths of the tapered curved square plate are 859.4 mm corresponding to the taper angle of 0.1 degree and 171.9 mm corresponding to the taper angle of 0.5 degree respectively. In the Fig. 2.5, λ_{t_r} denotes the critical buckling load.

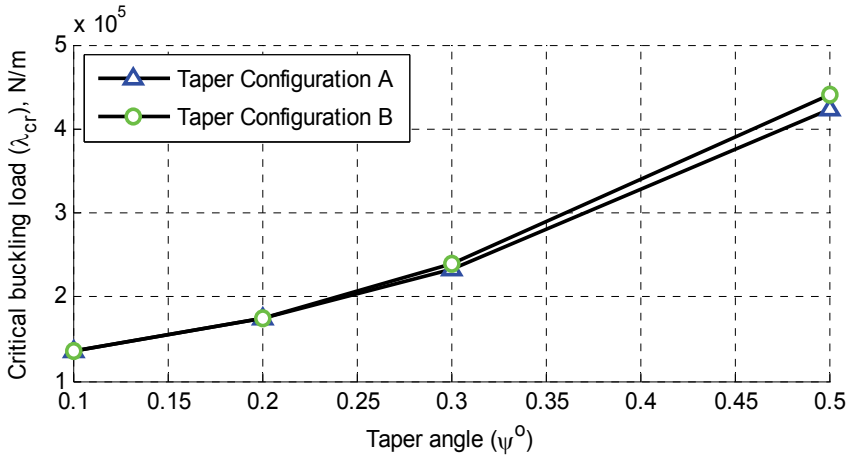

Figure 2.5: Effect of taper angle on buckling load for clamped tapered curved laminates with the lay-up configuration LC_1 and taper configuration B.

As can be observed from Fig. 2.5, the critical buckling loads of two taper configurations increase with the increase of taper angle, because the plates become shorter (without changing the thickness) with the increase of taper angle. Taper configuration A has a large resin pocket at the core. Alternatively, taper configuration B has distributed five small resin pockets with the continuous plies above and below the resin pockets. For that reason, the buckling load of taper configuration B is higher than that of taper configuration A. At lower values of taper angle, buckling loads do not vary significantly. On the other hand, at the higher values of taper angle buckling loads disperse away from each other. The critical buckling load depends on both taper configuration and taper angle. The critical buckling load varies nonlinearly with the variation of taper angle.

2.5.1.3 Influence of Length-to-Radius Ratio

Effect of length-to-radius ratio on normalized buckling loads for the clamped tapered curved laminate with the taper configurations A and B is shown in the Figure 2.6. The

lay-up configuration is LC_1 and the clamped-clamped (C4-C4) boundary conditions are considered. The material properties of composite and epoxy are used same as given in the Tables 2.5 and 2.6 respectively. In the Fig. 2.6, R denotes the radius, h_{tk} denotes the thickness at thick end, λ_{cr} denotes the critical buckling load, L_{tap} denotes the length of tapered plates and $E_{x"}$ denotes the elastic modulus of composite material in the fiber direction.

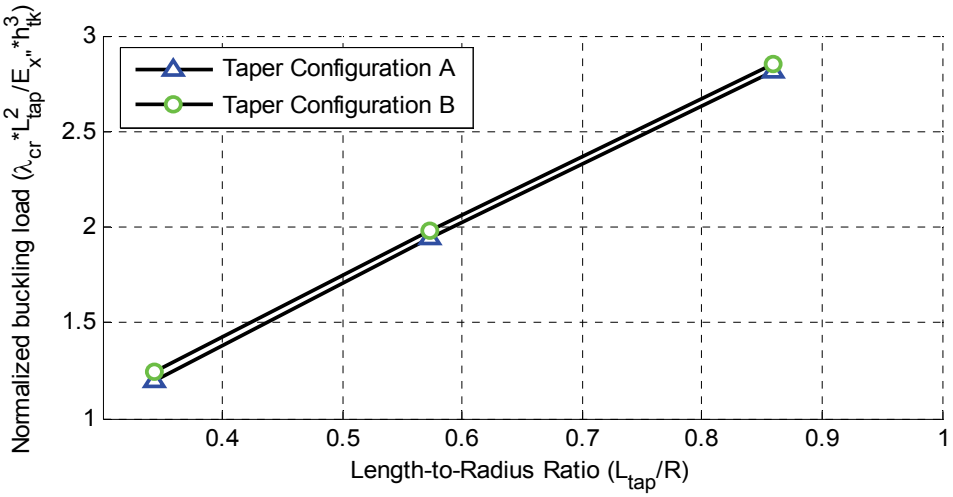

Figure 2.6: Effect of length-to-radius ratio on buckling load for the clamped tapered curved laminate with the lay-up configuration LC_1 and the taper configuration B.

As observed from Fig. 2.6, the normalized buckling loads increase with the increase of length-to-radius ratio. But the buckling coefficients of the taper configurations are close to each other and do not significantly differ from each other. The buckling coefficient is more dependent on length- to-radius ratio than the taper configuration.

2.5.2 Buckling Analyses of Hybrid Curved Plates

Laminates with only taper section have been studied in the previous sections and the hybrid (combinations of tapered and uniform-thickness) sections are taken into account in the present sub-section of thesis. The tapered part of hybrid plates is modeled using the configuration B. For the analysis of hybrid configuration three types of lay-up configurations, namely LC_1, LC_2 and LC_3 given in the Table 2.7 are considered. For the buckling analysis, total plate length L = 229.2 mm, width b = 114.6 mm and the material properties of Tables 2.5 and 2.6 are considered. According to the first-ply failure analysis, the hybrid plates with the above mentioned lay-up configurations will not fail by first-ply failure before global buckling. Two parameters, namely radius-to-thickness ratio and boundary conditions are considered to see the influences of these parameters on buckling load of hybrid curved plates. The results are shown in the following Figs. 2.7 through 2.11.

2.5.2.1 Influence of Lay-Up Configurations

The normalized buckling loads of three lay-up configurations are calculated using Ritz method as shown in the Figs. 2.7 - 2.8. The buckling loads are calculated for clamped-clamped (C4-C4) boundary conditions. The buckling load is considered in the Figs. 2.7 - 2.8 to see the influence of the lay-up configurations on R/h_{tk}. In these figures, R denotes the radius, h_{tk} denotes the thickness at thick end, λ_{cr} denotes the critical buckling load, L denotes the total length of hybrid plates and $E_{x"}$ denotes the elastic modulus of composite material in the fiber direction. From Figs. 2.7 - 2.8, the following observations are made:

a) The lay-up configuration LC_2 is the weakest one among all other lay-up configurations.

b) The rate of change of buckling load of lay-up LC_3 is lesser than that of lay-up configuration LC_1. Due to this type of characteristic, the critical buckling load of LC_1 is higher than that of LC_3 for the smaller radius-to-thickness ratio ($R/h_{tk} <$ 230 for clamped plate and $R/h_{tk} < 265$ for simply-supported plate). In case of larger radius-to-thickness ratio ($R/h_{tk} > 230$ for clamped plate and $R/h_{tk} > 265$ for simply-supported plate), LC_3 is stronger than LC_1.

c) In all the cases, the normalized buckling loads decrease nonlinearly with the increase of radius-to-thickness ratio. The buckling coefficient becomes close to each other at the larger value of R/h_{tk} as the plate becomes thinner.

d) All the lay-up configurations are R/h_{tk} dependent.

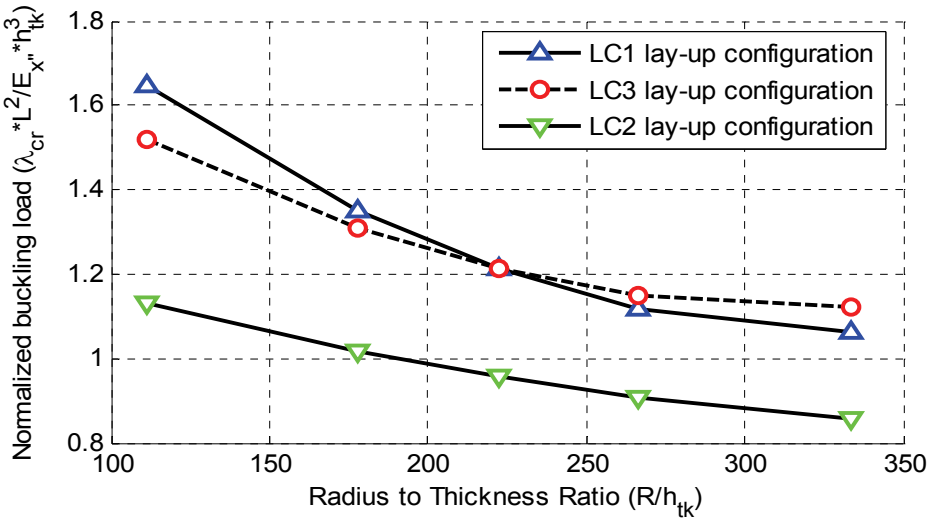

Figure 2.7: Variation of buckling load with the change of radius-to-thickness ratio of the clamped-clamped (C4-C4) hybrid plates for different lay-up configurations.

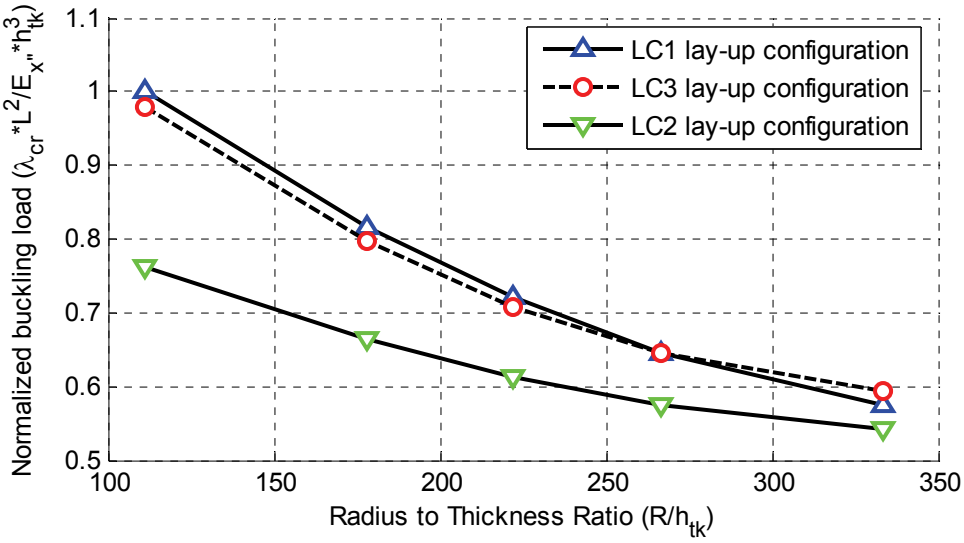

Figure 2.8: Variation of buckling load with the change of radius-to-thickness ratio of simply supported (S4-S4) hybrid plates for different lay-up configurations.

2.5.2.2 Influence of Boundary Conditions

Normalized buckling load is calculated for the rectangle hybrid plates (with a length/width ratio of 2.0) under uniaxial compression. The buckling analysis is performed using Ritz method based on Novozhilov's shell theory. Two boundary conditions are considered, that are, clamped at four edges (C4-C4) and simply supported at four edges (S4-S4). These boundary conditions are given in the Appendix A. The effect of radius-to-thickness ratio on buckling coefficient for the above mentioned plates is shown in the Figs. 2.9 - 2.11.

As observed from Figs. 2.9 - 2.11, boundary condition has a drastic effect on buckling coefficient. In terms of buckling load, the fully clamped plate has the higher buckling

load than the simply-supported plate. Simply supported plates have more degrees of freedom than the clamped ones which is the reason for less strength. All the lay-up configurations are both R/h_{tk} and boundary condition dependent.

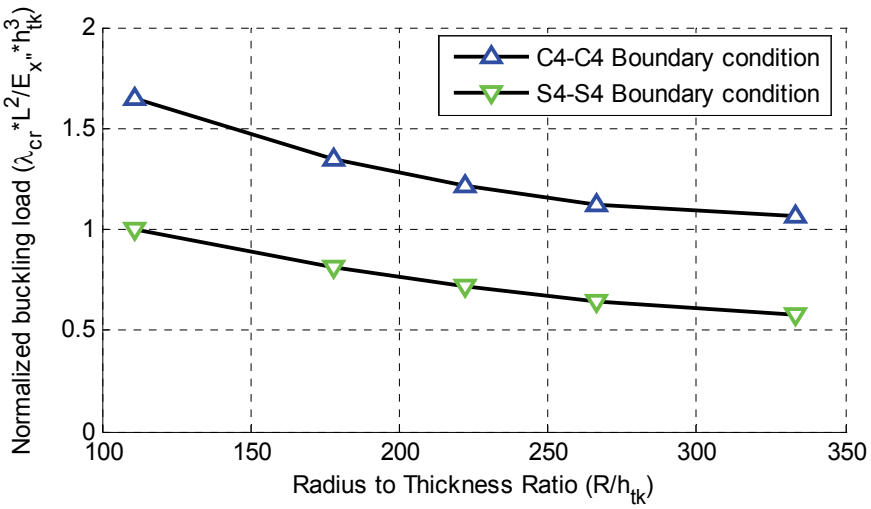

Figure 2.9: Comparison of buckling load of the hybrid plate with LC_1 lay-up configuration for different boundary conditions.

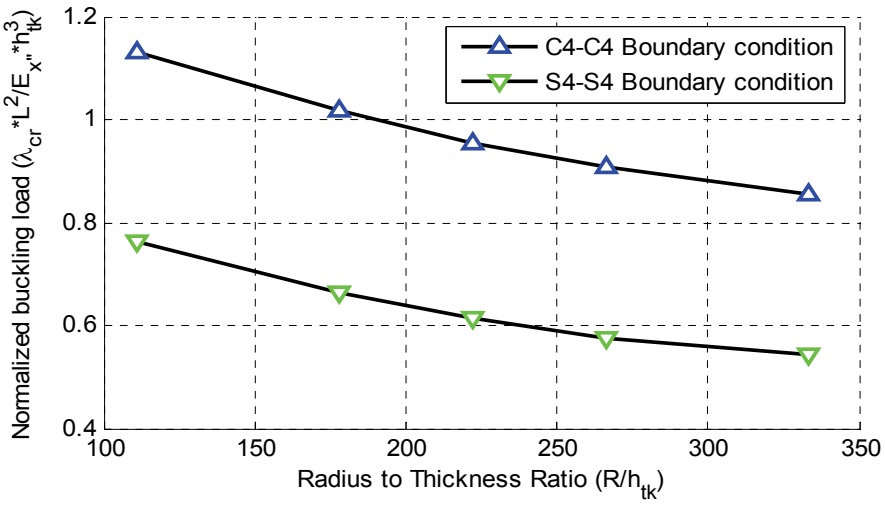

Figure 2.10: Comparison of buckling load of the hybrid plate with LC_2 lay-up configuration for different boundary conditions.

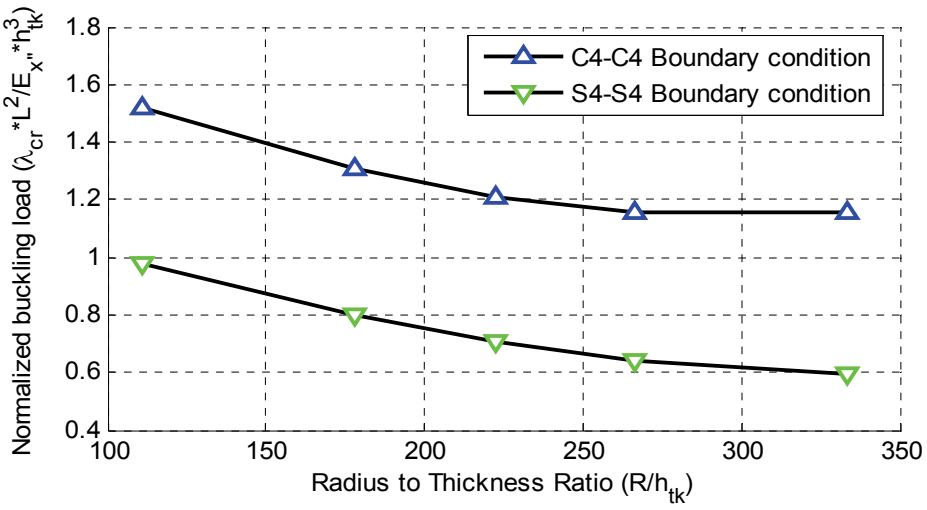

Figure 2.11: Comparison of buckling load of the hybrid plate with LC_3 lay-up configuration for different boundary conditions.

2.6 CONCLUSIONS

In the present chapter, buckling analysis has been carried out using Ritz method based on eight well known classical shallow shell theories, namely Donnell's, Love's, Mushtari's, Timoshenko's, Vlasov's, Sander's, Koiter's and Novozhilov's thoeries. Two types of taper configurations (A and B) and three types of lay-up configurations (LC_1, LC_2 and LC_3) are considered under uniaxial compressive load. A detailed parametric study of curved (tapered and hybrid) plates has been conducted that includes the effects of boundary conditions, stacking sequence, taper configurations, radius, and geometric parameters of the plates. Among the important conclusions and observations one may list the following:

a) The buckling results based on different shell theories are close to each other but the Novozhilov's theory provides the most conservative result.

b) The moderately thick and tapered curved composite plates may fail by first-ply failure before global buckling. Therefore the tapered curved plate should be larger than the corresponding critical size. The critical size depends on both radius and staking sequence of the curved plates.

c) The tapered flat plate is more flexible than uniform flat plate, but the tapered curved plate provides a better design option in terms of saving the material without any compromise of the strength.

d) The normalized buckling load is more dependent on length-to-radius ratio (L_{tap}/R) than the taper configuration.

e) The buckling loads of all the lay-up configurations are both radius-to-thickness ratio (R/h_{tk}) and boundary condition dependent.

Chapter 3

Ply Failure vs. Global Buckling of Tapered Curved Composite Plates

3.1 INTRODUCTION

In this chapter, approximate analytical solutions are developed using Ritz method for the global buckling response of tapered curved plates considering uniaxial compression. Buckling analysis of tapered curved plates is carried out based on six well-established First-order shear deformation Shell Theories (FST). Various boundary conditions, and different lay-up and taper configurations are considered. The critical buckling loads calculated using the Ritz method are compared with that of the existing experimental and analytical results. The failure strength characteristics and load carrying capability of the tapered curved plates are studied considering two predominant types of local failures, which are the first-ply failure and the delamination failure. Based on the failure and buckling analyses, the critical values of size and shape parameters of the plates such that they will fail only in global buckling mode are determined. A comprehensive parametric study is carried out and design guidelines for the tapered curved plates are established based on this study.

3.2 FORMULATION

To determine the stiffness matrix of a ply in a tapered laminate, three coordinate systems have been defined: principal material coordinate system (x'', y'', z''), local coordinate system (x', y', z') and global coordinate system (x, y, z). These systems are shown in Fig. 2.1.

After two successive stress and strain transformations, with the first to transform from (x'', y'', z'') to (x', y', z') system and the second to transform from (x', y', z') to (x, y, z) system, the stress-strain relationship in the global coordinate system (x, y, z) for a ply in a tapered laminate is determined as:

$$\begin{Bmatrix} \sigma_{xx} \\ \sigma_{yy} \\ \sigma_{zz} \\ \tau_{yz} \\ \tau_{xz} \\ \tau_{xy} \end{Bmatrix} = \begin{bmatrix} \overline{C}_{11} & \overline{C}_{12} & \overline{C}_{13} & \overline{C}_{14} & \overline{C}_{15} & \overline{C}_{16} \\ & \overline{C}_{22} & \overline{C}_{23} & \overline{C}_{24} & \overline{C}_{25} & \overline{C}_{26} \\ & & \overline{C}_{33} & \overline{C}_{34} & \overline{C}_{35} & \overline{C}_{36} \\ & & & \overline{C}_{44} & \overline{C}_{45} & \overline{C}_{46} \\ & & & & \overline{C}_{55} & \overline{C}_{56} \\ sym & & & & & \overline{C}_{66} \end{bmatrix} \begin{Bmatrix} \varepsilon_{xx} \\ \varepsilon_{yy} \\ \varepsilon_{zz} \\ \gamma_{yz} \\ \gamma_{xz} \\ \gamma_{xy} \end{Bmatrix} \tag{3.1}$$

where σ_{ij} and τ_{ij} are the normal stresses and shear stresses respectively, and ε_{ij} and γ_{ij} are the normal strains and engineering shear strains respectively with i, j = x, y, z in the global coordinate system (x, y, z).

Eq. (3.1) can be written in short form as

$$\{\sigma\}_{xyz} = [\overline{C}]_{xyz} \{\varepsilon\}_{xyz} \tag{3.2}$$

Thus, the material stiffness matrix $[\overline{C}]_{xyz}$ in the global coordinate system (x, y, z) can be expressed by the material stiffness matrix $[C'']_{x''y''z''}$ in the principal material coordinate system (x'', y'', z'') and the transformation matrices as:

$$[\overline{C}]_{xyz} = [T_{\sigma\psi}][T_{\sigma\theta}][C'']_{x''y''z''}[T_{\sigma\theta}]^T[T_{\sigma\psi}]^T \tag{3.3}$$

where $[T_{\sigma\theta}]$ and $[T_{\sigma\psi}]$ are the stress transformation matrices due to fiber orientation angle θ and taper angle ψ respectively. The superscript T stands for transpose.

In the case of small taper angle and moderately-thick plates, the normal stress σ_{zz} in the z-direction is very small compared to other stresses. Therefore, applying the condition

that $\sigma_{zz}=0$ in the Eq. (3.1), the corresponding reduced stiffness matrix is calculated and expressed after rearrangement as:

$$\begin{Bmatrix}\sigma_{xx}\\ \sigma_{yy}\\ \tau_{xy}\\ \tau_{yz}\\ \tau_{xz}\end{Bmatrix}=\begin{bmatrix}Q_{11} & Q_{12} & Q_{16} & Q_{14} & Q_{15}\\ Q_{12} & Q_{22} & Q_{26} & Q_{24} & Q_{25}\\ Q_{16} & Q_{26} & Q_{66} & Q_{46} & Q_{46}\\ Q_{14} & Q_{24} & Q_{46} & Q_{44} & Q_{45}\\ Q_{15} & Q_{25} & Q_{56} & Q_{45} & Q_{55}\end{bmatrix}\begin{Bmatrix}\varepsilon_{xx}\\ \varepsilon_{yy}\\ \gamma_{xy}\\ \gamma_{yz}\\ \gamma_{xz}\end{Bmatrix} \tag{3.4}$$

where $Q_{ij}=\overline{C}_{ij}-\overline{C}_{i3}\overline{C}_{j3}/\overline{C}_{33}$; i, j = 1, 2, 4, 5, 6. (3.5)

and $\overline{C}_{ij}$ is the material stiffness coefficient in the global coordinate system given by the Eq. (3.3).

The equations for coefficients of matrices [A], [B] and [D] for tapered laminate can be written as

$$(A_{ij}, B_{ij}, D_{ij})=\int_{-h/2}^{h/2} Q_{ij}(1, z, z^2)dz \qquad \text{i , j = 1,2,4,5,6} \tag{3.6}$$

The strain-displacement relations corresponding to different shell theories are considered for the case of small deformations of a curved plate with radius R and written in terms of the mid-plane displacement field (u_o, v_o, w_o) that refers to the global coordinate system (x, y, z) as shown in Fig. 2.1. Further, φ_x and φ_y denote the rotations due to shear deformation. The tracer coefficients c_1 and c_2 are introduced to express the strain-displacement relations corresponding to the six different shell theories for shallow $(h_{tk}/R<<1)$ curved plate. The strain field can be expressed as:

$$[\varepsilon_{xx}\ \ \varepsilon_{yy}\ \ \gamma_{xy}\ \ \gamma_{yz}\ \ \gamma_{xz}]^T=[\varepsilon^o_{xx}\ \ \varepsilon^o_{yy}\ \ \gamma^o_{xy}\ \ \gamma^o_{yz}\ \ \gamma^o_{xz}]^T+z[\kappa^o_{xx}\ \ \kappa^o_{yy}\ \ \kappa^o_{xy}\ \ 0\ \ 0]^T \tag{3.7}$$

with (3.8)

$$\begin{Bmatrix} \varepsilon_{xx}^{o} \\ \varepsilon_{yy}^{o} \\ \gamma_{xy}^{o} \\ \gamma_{yz}^{o} \\ \gamma_{xz}^{o} \end{Bmatrix} = \begin{Bmatrix} \dfrac{\partial u_o}{\partial x} \\ \dfrac{\partial v_o}{\partial y} + \dfrac{w_o}{R} \\ \dfrac{\partial u_o}{\partial y} + \dfrac{\partial v_o}{\partial x} \\ \varphi_y + \dfrac{\partial w_o}{\partial y} - c_2 \dfrac{v_o}{R} \\ \varphi_x + \dfrac{\partial w_o}{\partial x} \end{Bmatrix}$$

and

$$\begin{Bmatrix} \kappa_{xx}^{o} \\ \kappa_{yy}^{o} \\ \kappa_{xy}^{o} \\ 0 \\ 0 \end{Bmatrix} = \begin{Bmatrix} \dfrac{\partial \varphi_x}{\partial x} \\ \dfrac{\partial \varphi_y}{\partial y} \\ \dfrac{\partial \varphi_x}{\partial y} + \dfrac{\partial \varphi_y}{\partial x} + \dfrac{c_1}{2R}\left(\dfrac{\partial v_o}{\partial x} - \dfrac{\partial u_o}{\partial y} \right) \\ 0 \\ 0 \end{Bmatrix} \tag{3.9}$$

where the column matrices $[\varepsilon_{xx}^{0} \;\; \varepsilon_{yy}^{0} \;\; \gamma_{xy}^{0} \;\; \gamma_{yz}^{0} \;\; \gamma_{xz}^{0}]^T$ and $[\kappa_{xx}^{o} \;\; \kappa_{yy}^{o} \;\; \kappa_{xy}^{o} \;\; 0 \;\; 0]^T$ are, respectively, the matrix of mid-plane strains and the matrix of curvatures.

By setting,

i) $c_1 = c_2 = 0$, equations that correspond to Donnell's [108] and Morley's [109] shell theories are obtained.

ii) $c_1 = 0$ and $c_2 = 1$, equations that correspond to Love's [98] and Loo's [110] shell theories are obtained.

iii) $c_1 = 1$ and $c_2 = 1$, equations that correspond to Sanders's [100] and Koiter's [101] shell theories are obtained.

In the case of shallow shells, the Koiter's and the Sanders's shell theories lead to the same expressions for strains and curvatures. In the present work, shallow tapered laminated shells are considered. Therefore, these two shell theories are referred to together as 'Koiter-Sanders shell theory'.

The force and moment resultants are written using the above mentioned strain field and the laminate stiffness matrices given in the Eq. (3.6), in the form:

$$\left\{\begin{array}{c} N_{xx} \\ N_{yy} \\ \hline N_{xy} \\ M_{xx} \\ M_{yy} \\ \hline M_{xy} \\ Q_{yz} \\ Q_{xz} \end{array}\right\} = \left[\begin{array}{ccc|ccc|c} A_{11} & A_{12} & A_{16} & B_{11} & B_{12} & B_{16} & S_1\begin{pmatrix} A_{14} & A_{15} \\ A_{24} & A_{25} \\ A_{46} & A_{56} \end{pmatrix} \\ A_{12} & A_{22} & A_{26} & B_{12} & B_{22} & B_{26} & \\ A_{16} & A_{26} & A_{66} & B_{16} & B_{26} & B_{66} & \\ \hline B_{11} & B_{12} & B_{16} & D_{11} & D_{12} & D_{16} & S_1\begin{pmatrix} B_{14} & B_{15} \\ B_{24} & B_{25} \\ B_{46} & B_{56} \end{pmatrix} \\ B_{12} & B_{22} & B_{26} & D_{12} & D_{22} & D_{26} & \\ B_{16} & B_{26} & B_{66} & D_{16} & D_{26} & D_{66} & \\ \hline S_2\begin{pmatrix} A_{14} & A_{24} & A_{46} \\ A_{15} & A_{25} & A_{56} \end{pmatrix} & & & S_2\begin{pmatrix} B_{14} & B_{24} & B_{46} \\ B_{15} & B_{25} & B_{56} \end{pmatrix} & & & S_3\begin{pmatrix} A_{44} & A_{45} \\ A_{45} & A_{55} \end{pmatrix} \end{array}\right] \left\{\begin{array}{c} \varepsilon^o_{xx} \\ \varepsilon^o_{yy} \\ \gamma^o_{xy} \\ \hline \kappa^o_{xx} \\ \kappa^o_{yy} \\ \kappa^o_{xy} \\ \hline \gamma^o_{yz} \\ \gamma^o_{xz} \end{array}\right\} \tag{3.10a}$$

The Eq. (3.10a) can be written in a short form as:

$$\left\{\begin{array}{c} N \\ \hline M \\ \hline Q \end{array}\right\} = [E^{'}]\{\varepsilon\} \tag{3.10b}$$

In the Eq. (3.10a) S_1, S_2 and S_3 are the Shear Correction (SC) factors. For uniform plate the coefficients S_1 and S_2 are set to be equal to zero but the coefficient S_3 is non-zero. Moreover, the value of S_3 is considered to be 5/6 for uniform plate. For a tapered plate the coefficients S_1, S_2 and S_3 will have non-zero values. There is no experimental or analytical work that is currently available as to what values of S1, S2 and S3 are appropriate for tapered laminated plates. Considering this, in the present work, all possible combinations of these SC factors (S_1, S_2 and S_3) are considered and corresponding analyses are conducted. The number of permutations of three SC factors

by taking the two numerical values (1 and 5/6) at a time is to be 6. Accordingly, the following six sets of SC factors are considered in the buckling analysis and corresponding critical buckling loads are calculated.

$S_1=1, \quad S_2=1, \quad S_3=1$ (3.11a)

$S_1=1, \quad S_2=1, \quad S_3=5/6$ (3.11b)

$S_1=1, \quad S_2=5/6, \quad S_3=5/6$ (3.11c)

$S_1=5/6, \quad S_2=5/6, \quad S_3=5/6$ (3.11d)

$S_1=5/6, \quad S_2=5/6, \quad S_3=1$ (3.11e)

$S_1=5/6, \quad S_2=1, \quad S_3=1$ (3.11f)

The set of SC factors that corresponds to the most conservative value of critical buckling loads is determined using the results of the analyses. This particular set of values is used futher onwards throughout the present work. For this purpose, a tapered plate with configuration B and having 36 layers at the thick end with $[0/90]_{9s}$ lay-up and 12 layers at the thin end with $[0/90]_{3s}$ lay-up, that is subjected to uni-axial end compressive loading has been analyzed using Ritz method. The plate is clamped at four edges (C4-C4) and the boundary conditions represented as C4 are given in the Appendix B. The dimensions of the square plate are (see Fig. 1.4): various values of the side length of the plate in the range of from 85.94 mm to 171.90 mm are considered, plate thickness at thick end h_{tk} = 4.5 mm and radius R = 500 mm. The material properties of the composite ply and epoxy are the same as given in Tables 2.5 and 2.6 respectively. The critical buckling load using six shear correction factors is shown in the Fig. 3.1 at the end of this section.

The strain energy of a tapered plate is written in Cartesian co-ordinates as follows:

$$\Pi = \frac{1}{2}\int_0^b \int_0^{L_{tap}} \left(\{\varepsilon\}^T \left[E'\right] \{\varepsilon\} \right) dxdy \tag{3.12}$$

where $$\{\varepsilon\} = [\varepsilon_{xx}^0 \quad \varepsilon_{yy}^0 \quad \gamma_{xy}^0 \quad \kappa_{xx}^0 \quad \kappa_{yy}^0 \quad \kappa_{xy}^0 \quad \gamma_{yz}^0 \quad \gamma_{xz}^0]^T \tag{3.13}$$

and $[E']$ is the stiffness matrix given in Eq. (3.10b).

The potential energy corresponding to the uni-axial end compression λ is

$$W = -\lambda \int_0^b \int_0^{L_{tap}} \left\{ \frac{\partial u_o}{\partial x} + \frac{1}{2}\left[\left(\frac{\partial v_o}{\partial x} \right)^2 + \left(\frac{\partial w_o}{\partial x} \right)^2 \right] \right\} dxdy \tag{3.14}$$

The approximate solutions for the displacement fields and rotations are expressed as a double series:

$$u_o(x,y) = \sum_{m=1}^{M}\sum_{n=1}^{N} U_{mn} U_m(x) U_n(y) \tag{3.15}$$

$$v_o(x,y) = \sum_{m=1}^{M}\sum_{n=1}^{N} V_{mn} V_m(x) V_n(y) \tag{3.16}$$

$$w_o(x,y) = \sum_{m=1}^{M}\sum_{n=1}^{N} W_{mn} W_m(x) W_n(y) \tag{3.17}$$

$$\varphi_x(x,y) = \sum_{m=1}^{M}\sum_{n=1}^{N} X_{mn} X_m(x) X_n(y) \tag{3.18}$$

$$\varphi_y(x,y) = \sum_{m=1}^{M}\sum_{n=1}^{N} Y_{mn} Y_m(x) Y_n(y) \tag{3.19}$$

The functions $U_m(x)$, $U_n(y)$, $V_m(x)$, $V_n(y)$, $W_m(x)$, $W_n(y)$, $X_m(x)$, $X_n(y)$, $Y_m(x)$ and $Y_n(y)$ are so chosen as to satisfy the boundary conditions which are given in the Appendix B and the coefficients U_{mn}, V_{mn}, W_{mn} , X_{mn} and Y_{mn} are determined by the following stationary conditions:

$$\frac{\partial \prod}{\partial U_{mn}} = \frac{\partial W}{\partial U_{mn}} \tag{3.20}$$

$$\frac{\partial \prod}{\partial V_{mn}} = \frac{\partial W}{\partial V_{mn}} \tag{3.21}$$

$$\frac{\partial \prod}{\partial W_{mn}} = \frac{\partial W}{\partial W_{mn}} \tag{3.22}$$

$$\frac{\partial \prod}{\partial X_{mn}} = \frac{\partial W}{\partial X_{mn}} \tag{3.23}$$

$$\frac{\partial \prod}{\partial Y_{mn}} = \frac{\partial W}{\partial Y_{mn}} \tag{3.24}$$

where, $\prod$ and W are given by the Eqs. (3.12) and (3.14) respectively.

Using the Eqs. (3.20) through (3.24) the following matrix equation is obtained:

$$\begin{bmatrix} [L_{IJ}^{11}] & [L_{IJ}^{12}] & [L_{IJ}^{13}] & [L_{IJ}^{14}] & [L_{IJ}^{15}] \\ [L_{IJ}^{12}] & [L_{IJ}^{22}] & [L_{IJ}^{23}] & [L_{IJ}^{24}] & [L_{IJ}^{25}] \\ [L_{IJ}^{13}] & [L_{IJ}^{23}] & [L_{IJ}^{33}] & [L_{IJ}^{34}] & [L_{IJ}^{35}] \\ [L_{IJ}^{14}] & [L_{IJ}^{24}] & [L_{IJ}^{34}] & [L_{IJ}^{44}] & [L_{IJ}^{45}] \\ [L_{IJ}^{15}] & [L_{IJ}^{25}] & [L_{IJ}^{35}] & [L_{IJ}^{45}] & [L_{IJ}^{55}] \end{bmatrix} \begin{Bmatrix} U_{IJ} \\ V_{IJ} \\ W_{IJ} \\ X_{IJ} \\ Y_{IJ} \end{Bmatrix} = -\bar{\lambda} \begin{bmatrix} [0] & [0] & [0] & [0] & [0] \\ [0] & [G_{IJ}^{22}] & [0] & [0] & [0] \\ [0] & [0] & [G_{IJ}^{33}] & [0] & [0] \\ [0] & [0] & [0] & [0] & [0] \\ [0] & [0] & [0] & [0] & [0] \end{bmatrix} \begin{Bmatrix} U_{IJ} \\ V_{IJ} \\ W_{IJ} \\ X_{IJ} \\ Y_{IJ} \end{Bmatrix} \tag{3.25}$$

Further details about the matrices $[L_{IJ}^{11}]$, $[L_{IJ}^{12}]$, $[G_{IJ}^{22}]$, $[G_{IJ}^{33}]$, and so on are given in the Appendix B. The eigenvalues $\bar{\lambda}$ are the values of buckling loads. The following indicial expressions were introduced [105] and used in the Eq. (3.25):

$$I = (m-1)M + n \quad \text{and} \quad J = (i-1)N + j \tag{3.26}$$

where $i, m = 1,2.....M$ and $j, n = 1,2.....N$.

Eq. (3.25) can be written in a short form:

$$\left|[K^{'}] + \bar{\lambda}[Z^{'}]\right| = 0 \tag{3.27}$$

where [K'] and [Z'] are the stiffness matrix and geometric stiffness matrix respectively of the tapered plate. Eq. (3.27) is solved using MATLAB® as an eigenvalue problem. The smallest value of $\bar{\lambda}$ is the critical buckling load, λ_{cr}.

The critical buckling loads of taper configuration B corresponding to various taper angles are plotted in the Fig. 3.1. It can be seen from Fig. 3.1 that the set (S_1=1, S_2=5/6, S_3=5/6) given in the Eq. (3.11c) is the most conservative one in terms of critical buckling load. This set of shear correction factors will be used further onwards in the present work.

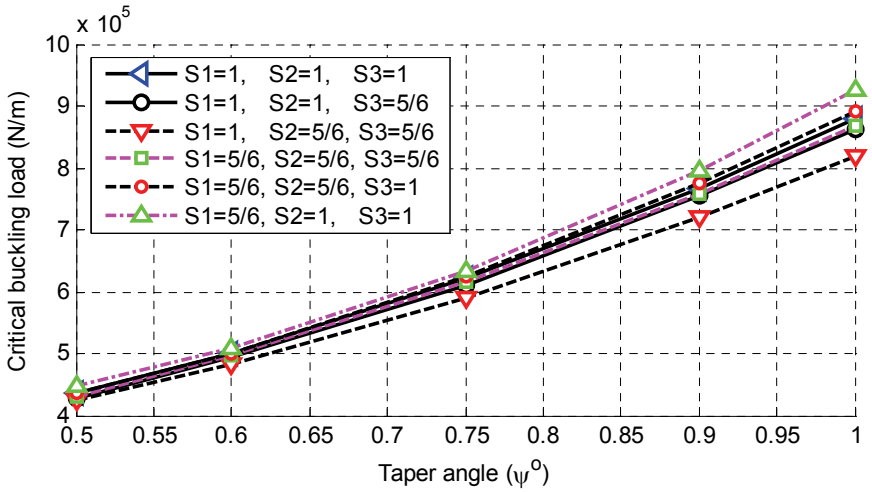

Figure 3.1: Comparison of critical buckling load obtained using six sets of SC factors for the laminate with the taper configuration B based on Koiter-Sanders shell theory.

3.3 VALIDATION

The commercial software ANSYS® has been chosen to model the curved composite plates to compare the buckling loads obtained using Ritz method based on FST. Element SHELL99 is used for the analyses using ANSYS®. SHELL99 is an 8-node, 3-D shell element with six degrees of freedom (three translations and three rotations) at each node. It is designed based on the degenerated solid approach with shear deformation effect and

to model thin to moderately-thick plate and shell structures with a side-to-thickness ratio of roughly 10 or greater. The tapered curved plates are meshed by using eighty-one elements which are shown by numbering in the Fig. 2.2.

To the authors' knowledge, no results are available yet in the literature on the buckling loads of the tapered curved composite plates under the action of uni-axial compression. Therefore the comparison with the existing works could not be made. However, in order to validate the formulation and analysis, first, the taper angle is set to be zero, and the resulting uniform-thickness laminates have been analyzed and the results have been compared with that available in the literature for the uniform-thickness laminates [107]. For this reason, a uniform-thickness cylindrical panel made of T300/5208 graphite/epoxy material having the mechanical properties of $E_{x"} = 141.34$ GPa (20.5×10^6 psi), $E_{y"} = 8.96$ GPa (1.3×10^6 psi), $G_{x"y"} = 5.17$ GPa (0.75×10^6 psi) and $\upsilon = 0.335$ are considered. The plate is clamped (C3) in transverse direction and simply-supported (S3) in longitudinal direction. The boundary conditions C3 and S3 are given in the Appendix B. The dimensions of the plate are taken to be: length L = 0.3048 m (12 inches), cord $b^{'}$ = 0.3048 m, radius R = 0.3048 m, thickness h = 1.016×10^{-03} m (0.04 inches). Becker [107] has conducted the bifurcation (obtained from eigenvalue solution) buckling analysis of this curved plate using STAGS computer code. In the present study, the buckling analysis is carried out using Ritz method based on various shell theories and the results are compared with that given in the work of Becker [107]. The buckling load is also obtained using ANSYS®. The normalized buckling load is given in the Table 3.1 wherein λ_{cr} denotes the critical buckling load.

As can be observed from the Table 3.1, the results obtained in the present work are in good agreement with the theoretical buckling load given in the reference work. The present results as well as the theoretical results given in Becker [107] are higher than the experimental result. According to Ref. [107], the bifurcation buckling load may be 23 to 45 percent higher than the experimental result for the critical buckling load. The results obtained based on different shell theories are somewhat close to each other but the Koiter-Sanders shell theory provides the most conservative result. The result obtained using ANSYS® overestimates the critical buckling load. Therefore in the present study, the Koiter-Sanders shell theory is used to calculate the buckling load using Ritz method.

Table 3.1: Comparison of critical buckling loads for the uniform-thickness cylindrical plate

Laminate Configuration	Becker [107] $(\lambda_{cr} L^2)/(E_{x''} h^3)$		Present $(\lambda_{cr} L^2)/(E_{x''} h^3)$			
	Exp.	Theory (Bifurcation)	Donnell, Morley	Koiter- Sanders	Love, Loo	ANSYS®
$[90/0]_{2s}$	24.50	33.30	34.84	34.70	34.75	37.34

Next, a tapered plate with only two (one above and corresponding one below the mid plane) internally-dropped plies has been analyzed using Ritz method based on Koiter-Sanders theory. The plate has configuration $[90/0]_{2s}$ at thick end and $[90/0/90]_s$ at thin end. The material properties of the ply and the dimensions of the plate are the same as that mentioned before for the uniform-thickness cylindrical plate (Ref. [107]). The clamped-simply supported (C3-S3) boundary conditions are considered as in the previous case. The results obtained for critical buckling load are compared with that of two

uniform-thickness composite plates with lay-up configurations $[90/0]_{2s}$ and $[90/0/90]_s$, respectively. The critical buckling loads for these three laminates under uni-axial end compressive load are given in Table 3.2. As can be observed, the result for the tapered laminate is between that of the 8-layers uniform-thickness laminate and that of the 6-layers uniform-thickness laminate.

Table 3.2: Critical buckling loads for tapered and uniform-thickness composite plates

Plate	Critical Buckling Load (x 10^4 N/m)
8-Layers Uniform Plate $[90/0]_{2s}$	5.5366
Tapered Plate $[90/0]_{2s}$ - $[90/0/90]_s$	4.0094
6-Layers Uniform Plate $[90/0/90]_s$	2.9074

3.4 FIRST-PLY FAILURE ANALYSIS

The strength in compression of the tapered curved plate is investigated considering first-ply failure. This type of failure analysis is considered in the present work to determine whether any layer has failed (locally) due to compressive loading before the laminate as a whole fails on global buckling. First-ply failure analysis is carried out using ANSYS® based on the 3-D version of Tsai-Wu failure criterion given in the ANSYS® reference manual. The first-ply failure refers to the first instant at which any layer or more than one layer fails at the same load. The same criterion is applied for both the composite ply and the resin pocket. For this purpose, the resin pocket is considered (imagined) to be made up of layers of isotropic resin material. Material properties of composite ply and epoxy resin are given in the Tables 2.5 and 2.6 respectively.

Four square-shaped tapered composite plates of different sizes with taper configuration B (Fig. 1.4) and made of NCT/301 graphite-epoxy composite material are considered. The lay-up configuration for all the plates is $[0/90]_{9s}$ at the thick end and $[0/90]_{3s}$ at the thin end. This laminate is referred to as the laminate with lay-up configuration LC_1 in the Table 2.7 and further onwards. The side length of each of the square plates is as given in the Table 3.3, plate thickness at the thick end (h_{tk}) is 4.5 mm and the radius (R) of the plates is 500 mm. The clamped-clamped (C4-C4) boundary conditions as described in the Appendix B are considered. The results of first-ply failure analysis are summarized in the Table 3.3 along with the results of buckling analysis.

In the Table 3.3, the first-ply failure loads are compared with the buckling loads. As can be seen from this table, the tapered curved plates corresponding to taper angles of 0.75 and 1.0 degrees will fail by first-ply failure before the global buckling. On the other hand, the plates corresponding to taper angles of 0.1 and 0.50 degrees will not fail by first-ply failure even at the state of global buckling. Therefore, the maximum plate size should be corresponding to a taper angle of 0.53 degree and the critical length-to-height ratio (L_{tap} / h_{tk}) is to be 36. The failed layers numbered 2 and 3 respectively are the second layer and the third layer from the bottom surface of the laminate at the thick end of the plate. All the tapered curved plates failed at the thick end where the numbers of plies above or below the resin pockets are at minimum.

Table 3.3: Critical buckling loads and first-ply failure loads of tapered curved laminates with lay-up configuration LC_1 and taper configuration B

Taper Angle in Degrees	Side Length of the Square Plate (m)	Buckling Load Using Ritz Method (x 10^4 N/m)	First-ply Failure Load Using ANSYS® (x 10^4 N/m)	Failure Location (FEN, FLN)*
0.10	0.8594	14.08	48.05	1, 2
0.50	0.1719	40.05	42.00	1, 2
0.75	0.1146	59.37	43.50	9, 3
1.00	0.0859	79.48	45.60	9, 3

* FEN and FLN denote, respectively, the failed element number and failed layer number at first-ply failure.

Next, the tapered plates that correspond to the Table 3.3 are analyzed considering different radii values using the same boundary conditions (C4-C4), lay-up configuration (LC_1) and material properties (see Tables 2.5 and 2.6). The critical sizes of the tapered curved plates are determined corresponding to various radii values. For the calculation of the critical length-to-height ratio, the same procedure is applied as mentioned in the previous failure analysis for the plate with radius of 500 mm. In the Fig. 3.2, the values of the critical length-to-height ratio of tapered curved plates with various radii are plotted. In this figure, L_{tap} denotes the taper length and h_{tk} denotes the laminate thickness at the thick end. It is observed that the stiffness of the tapered curved plate increases with the decrease of radius. Therefore, critical length-to-height ratio is to be increased with the decrease of radius to avoid the material failure. It can also be seen in the Fig. 3.2 that the critical length-to-height ratio increases with the decrease of radius. The critical length-to-height ratio varies non-linearly with the change of radius. The design limit of the tapered curved composite plates with the lay-up configuration LC_1 and the taper configuration B is determined and represented as the hatched area in the Fig. 3.2. Beyond this limit, tapered curved plate with lay-up configuration LC_1 and taper configuration B will not fail

by first-ply failure before global buckling. Similar type of effect is also considered in the Fig. 2.3, where the critical length-to-height ratio (L_{tap} / h_{tk}) is to be 38.9 corresponds to taper angle of 0.49 degree.

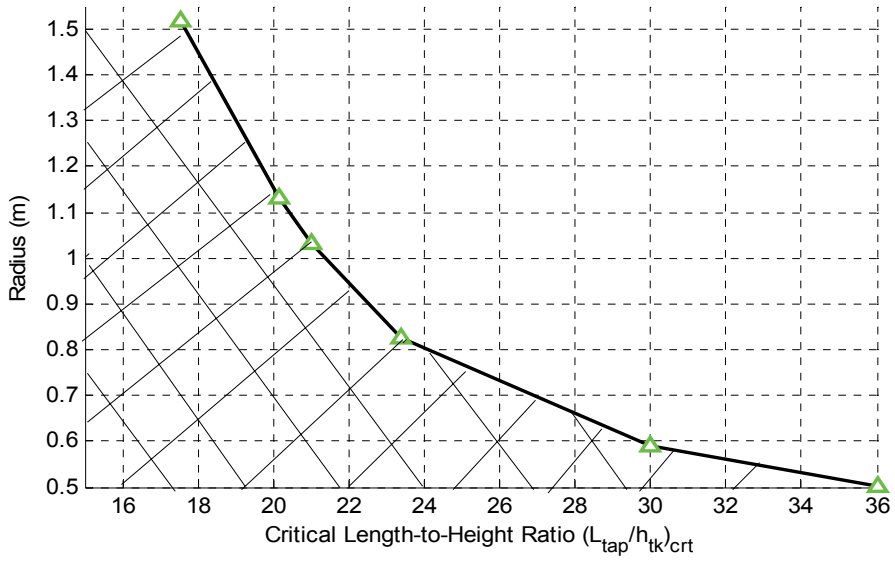

Figure 3.2: The relation between the critical length-to-height ratio and the radius of the tapered curved composite plate with the lay-up configuration LC_1 and the taper configuration B.

3.5 DELAMINATION FAILURE ANALYSIS

The initiation of delamination, if any, is dictated by the transverse interlaminar stresses developed under compressive load. In ANSYS®, interlaminar transverse shear stresses in shell element are calculated based on the assumption that no shear is carried at the top and bottom surfaces of the element. These interlaminar shear stresses are only computed in the interior of the element and are computed using equilibrium requirements. Delamination at any interface between any two adjacent layers is said to have occurred

when any of the transverse stress components in any of the two layers adjacent to the interface becomes equal to or greater than its corresponding allowable strength. Four square tapered composite plates of different sizes with taper configuration B and made of NCT/301 graphite-epoxy composite material are considered. The lay-up is $[0/90]_{9s}$ at the thick end and $[0/90]_{3s}$ at the thin end which together is defined as lay-up configuration LC_1 in the Table 2.7. The material properties of the composite ply and epoxy material are given in the Tables 2.5 and 2.6 respectively. The side length of the square plate varies from 85.9 to 859.4 mm, plate thickness at the thick end (h_{tk}) is 4.5 mm and radius (R) of the plates is 500 mm. The clamped-clamped (C4-C4) boundary conditions described in the Appendix B is considered. The averaged maximum interlaminer shear stresses are calculated in the present work at the state of first-ply failure load or critical buckling load (considering the larger one) and the corresponding locations are tabulated in the Table 3.4. The failed layers numbered 5 and 13 are, respectively, below and above the large resin pocket at the thin end.

Table 3.4: Averaged maximum interlaminar shear stress of clamped-clamped (C4-C4) tapered curved laminate with lay-up configuration LC_1 and taper configuration B

Taper Angle in Degrees	Side Length of Square Plate (m)	Compressive End Load (x 10^4 N/m)	Maximum Interlaminar Shear Stress, (MPa)	Location (EN, LLN)**	Remark
0.10	0.8594	48.05	1.01	63, 5	No Initiation of Delamination
0.50	0.1719	42.00	0.57	63, 5	
0.75	0.1146	59.37	0.99	55, 13	
1.00	0.0859	79.48	1.25	63, 5	

** EN and LLN denote, respectively, the element number and lower layer number adjacent to the interface where the interlaminer shear stress is maximum.

It is observed from the Table 3.4 that no initiation of delamination takes place for the taper configuration B and lay-up configuration LC_1 at the states of first-ply failure or global buckling. This is so because the maximum interlaminer shear stress in both the cases is less than the corresponding allowable shear strength of the composite material.

As an alternative approach, thin resin layers of thickness 0.0125 mm each are considered above the top resin pockets and below the bottom resin pockets as shown by the thick lines (thick lines are used to show these layers more clearly) in the Fig. 3.3; these thin resin plies are defined as 'resin-rich layers'. The longitudinal cross-section across the middle of curved laminate is considered. The thin resin-rich layers having thickness of one-tenth of a composite ply are taken into account in the analysis and transverse interlaminar normal and shear stresses developed at the locations of the ply drop-off are calculated to determine the stress states at these locations. The plate with a taper angle of 1 degree corresponding to the data given in the Table 3.4 is investigated using the same boundary conditions (C4-C4), ply-configuration (LC_1) and material properties (see Tables 2.5 and 2.6). The stresses are calculated under the compressive load of 79.48×10^4 N/m which is the critical buckling load corresponding to taper angle of 1 degree. The stresses at the top thin 'resin-rich layers' in the global coordinate directions (x,y,z) are plotted in the Fig. 3.4.

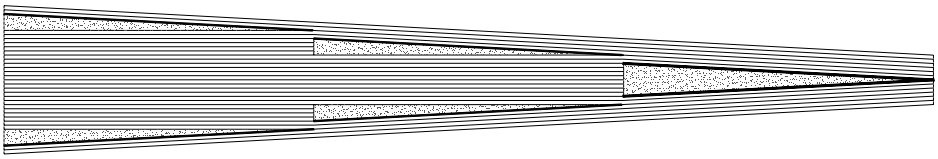

Figure 3.3: Longitudinal cross-section of taper configuration B with thin resin-rich layers.

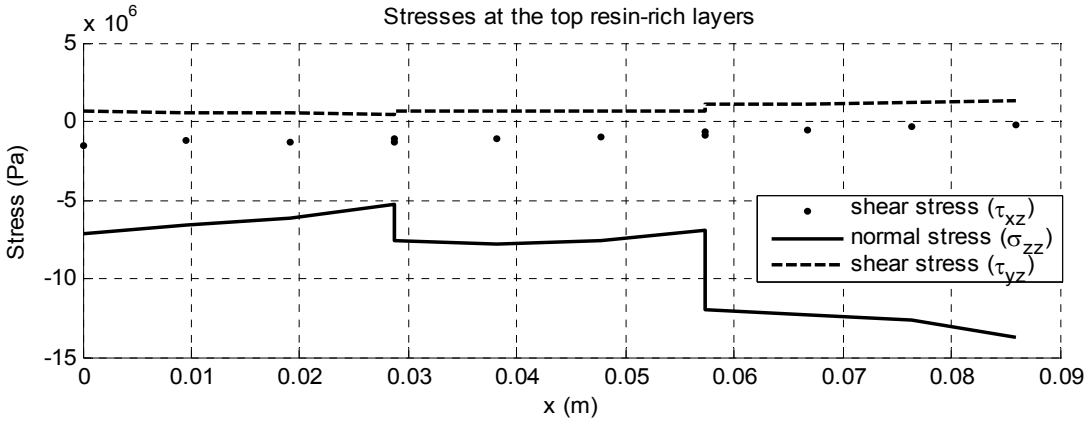

Figure 3.4: The stresses at the top 'resin-rich layers' with lay-up configuration LC_1 and taper configuration B for the taper angle of 1 degree.

From the stress distributions in 'resin-rich layers' shown in the Fig. 3.4, it is observed that significant normal and transverse stresses are present at these locations. These stresses are localized close to the region near the ply drops which are the probable locations for the initiation of delamination. In the Table 3.4, only the locations of maximum interlaminer stresses are identified but the present alternate approach is required to observe the distribution of these stresses along longitudinal direction. The drop in the normal stress σ_{zz} at each ply drop-off location is relatively higher than that in the interlaminar shear stresses. In addition, the drop in σ_{zz} at the ply drop-off that is close to the thin end is relatively the largest. It is to mention that the plate analyzed in

Fig. 3.4 will fail by first-ply failure load before global buckling as shown in Table 3.3. This may be the cause of the trace of normal stress σ_{zz}. A similar stress distribution has been observed at the bottom thin resin-rich layers.

3.6 PARAMETRIC STUDY

In the parametric study three types of longitudinal cross-sections of the curved plates are considered, that are, taper configurations A and B, and a hybrid configuration as shown in the Fig. 1.4. The Ritz solution is obtained based on Koiter-Sanders shell theory. The same material properties of composite ply and epoxy that are given in the Tables 2.5 and 2.6 respectively are used. The sizes of the plates are so chosen that the plates will not fail by first-ply failure before global buckling.

3.6.1 Buckling Analysis of Tapered Curved Plates

Tapered models shown in the Fig. 1.4 are considered with 36 and 12 plies at thick and thin ends respectively, which results in 24 drop-off plies. The configuration at the thick end is $[0/90]_{9s}$, and that of the thin end is $[0/90]_{3s}$ (this lay-up configuration is defined before as LC_1). In the analyses of taper configurations, the thickness at the thick end h_{tk} is set to be 4.5 mm and the radius of curved plate R is set to be 500 mm. For all taper configurations only LC_1 lay-up configuration with the boundary conditions of clamped at all four edges (C4-C4) are considered. The effects of various parameters, namely the ply drop-off parameters, taper angle and length-to-radius ratio on the critical buckling load of the tapered curved plates are investigated. The results are shown in the following Figs. 3.5 through 3.7.

3.6.1.1 Influence of Ply Drop-Off

The effect of ply drop-off on critical buckling load is shown in the Fig. 3.5. To investigate this effect, the side length of square tapered plate is considered as 859.4 mm corresponding to a taper angle of 0.1 degree. The thickness at the thick end is not changed and the taper angle is varied with the corresponding increase in the number of drop-off plies. The plate can be considered as a uniform-thickness plate when the number of ply drop-off is set to zero and the taper configuration A is obtained by dropping off twenty-four plies. The plates are clamped (C4-C4) at the four edges and the lay-up configuration is LC_1. In the Fig. 3.5, λ_{cr} denotes the critical buckling load.

From the Fig. 3.5, it is observed that the uniform-thickness curved plate is many times stiffer than the uniform-thickness flat plate in terms of buckling behavior. It is also observed that the tapered flat plate is less stiff than uniform flat plate. However, this strength reduction can be compensated for if the tapered plate is made into a curved one. Buckling loads of flat and curved plates vary linearly with the number of ply drop-offs. It can be concluded from the Fig. 3.5 that the tapered curved plate provides a better design option in terms of saving the material without any compromise of the strength.

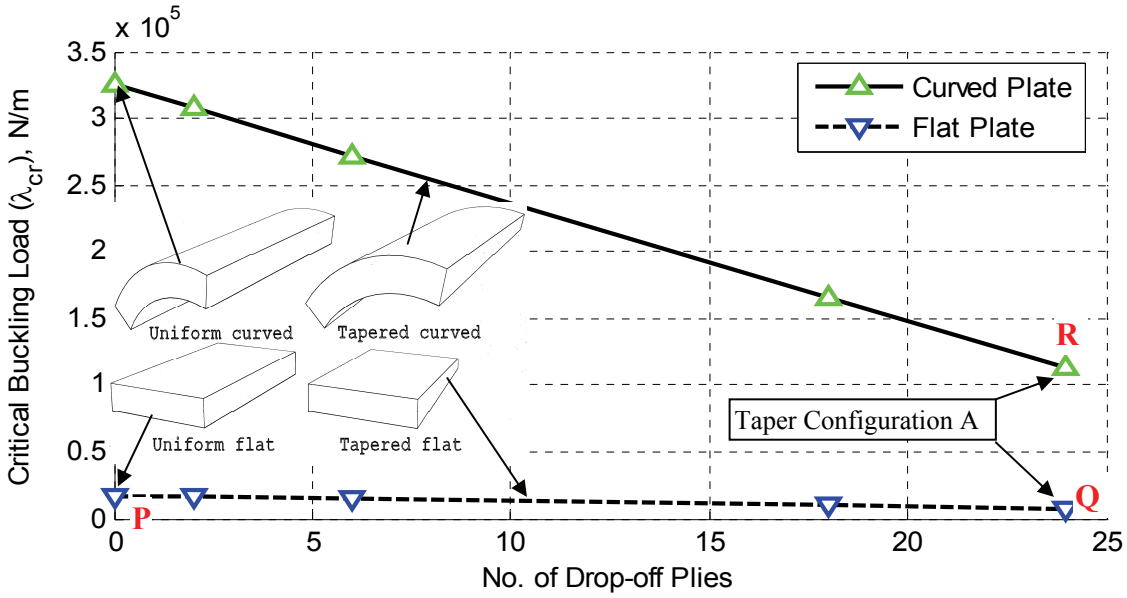

Figure 3.5: The effect of ply drop-off on critical buckling load for clamped-clamped (C4-C4) plates.

The weight savings provided by the tapered plate with respect to the uniform plate is expressed as:

$$W_s = (W^P - W^Q)/W^Q \times 100\% \tag{3.28}$$

where W^P and W^Q are the weights of the flat plate corresponding to the points marked as 'P' and 'Q' respectively in the Fig. 3.5.

Based on the Eq. (3.28), it is calculated that 29.40% weight of the flat plate can be saved by dropping-off 24 plies (at the location 'Q' in the Fig. 3.5). The strength of tapered curved plate with the taper configuration A (at the location 'R' in the Fig. 3.5) is 12.50 times higher than that of the flat tapered plate (at the location of 'Q'). Similar conclusions have also been arrived at for other taper configurations. Similar type of effect is presented in previous chapter in Fig. 2.4, where the buckling loads are calculated based

on classical shell theory. In Fig. 2.4, the buckling loads for both of the uniform and curved plates are 1.24 % higher than that of the present FST-based solution.

3.6.1.2 Influence of Taper Angle

The effect of the taper angle of the plate on the critical buckling load is determined using Ritz method based on First-order shear deformation Shell Theory (FST). The results are also compared with that obtained using Ritz method based on Classical Shell Theory (CST) given in the Refs. [111-112] and using Finite Element Method (FEM) given in the Ref. [113]. The size of the plate is decreased with the increase of taper angle while keeping the thickness of the thick section unchanged. The maximum and minimum edge lengths of the tapered curved square plates are, respectively, 859.4 mm corresponding to a taper angle of 0.1 degree and 171.9 mm corresponding to a taper angle of 0.5 degree. The comparison of critical buckling loads is shown in the Fig. 3.6 wherein λ_{cr} denotes the critical buckling load.

As can be observed, in all the three cases the critical buckling load increases as the taper angle is increased, because the plates become shorter (without any change in the thickness of the thick section) with the increase of taper angle. The buckling loads given in the Refs. [112] and [113] are, respectively, calculated using Ritz method based on Novozhilov's Classical Shell Theory (CST) and the nine-node Lagrange finite element based on First-order shear deformation Shell Theory (FST). In the case of buckling analysis based on the present FST based Ritz solution has more degrees of freedom compared to other two solutions (CST based Ritz solution and FST based FEM solution). For this reason, the buckling loads calculated using the present FST based Ritz solution

can be considered as the most conservative ones. At lower values of taper angle, the critical buckling loads calculated using the three different approaches do not vary significantly. On the other hand, at higher values of taper angle, the values of the critical buckling loads differ relatively much. Therefore it would be better to use the FST based Ritz solution for the thick and short plates. It can also be observed that in all the three cases, the critical buckling load varies nonlinearly with the variation of taper angle.

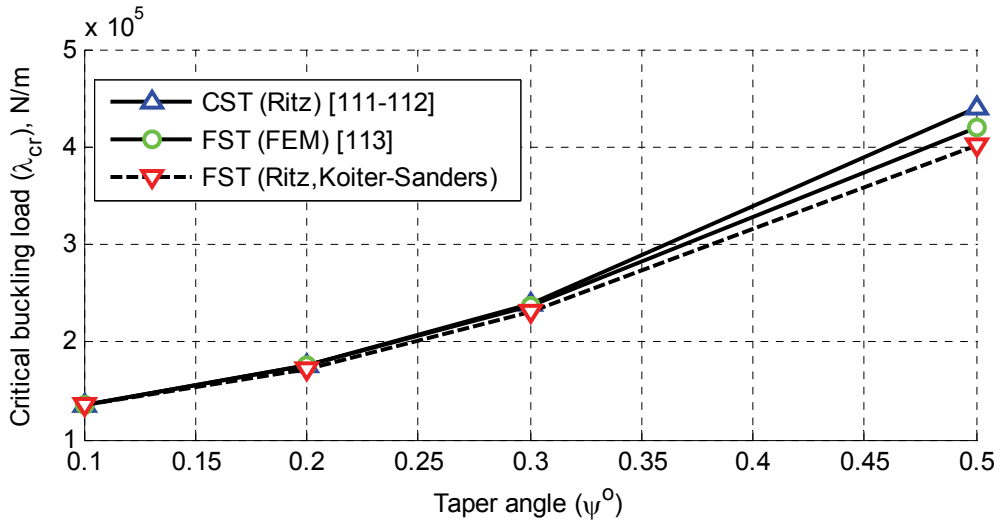

Figure 3.6: Effect of taper angle on the critical buckling load of clamped-clamped (C4-C4) tapered curved plate with lay-up configuration LC_1 and taper configuration B.

3.6.1.3 Influence of Length-to-Radius Ratio

The buckling loads of plates of different sizes are calculated using the present FST based Ritz solution and are compared with the buckling loads obtained using ANSYS®. The lay-up configuration is LC_1 and the clamped-clamped (C4-C4) boundary conditions are considered. The material properties used for composite ply and epoxy are the same as

given in the Tables 2.5 and 2.6 respectively. The results are presented in the Table 3.5, wherein R denotes the radius of the plate and L_{tap} denotes the length of the taper section.

Table 3.5: Critical buckling load of clamped-clamped (C4-C4) tapered curved laminate with lay-up configuration LC_1 and the taper configuration B

Taper Angle in Degrees	Side Length of Square Plate (m)	L_{tap}/R	Critical buckling load (x 10^4 N/m)	
			Ritz Solution	ANSYS®
0.10	0.8594	1.719	14.08	14.25
0.20	0.4297	0.859	15.86	16.21
0.30	0.2865	0.573	24.23	25.22
0.50	0.1719	0.345	40.05	42.00

As can be observed from Table 3.5, the critical buckling loads increase with the decrease of length-to-radius ratio. The plates become shorter with the decrease of this ratio which is the cause of increase of the critical buckling load. The critical buckling loads calculated using ANSYS® are higher than that obtained using Ritz method. In ANSYS® solution, an 8-node shell element (SHELL99) is considered based on the degenerated solid approach but the Ritz solution is developed based on the shear deformation shell theory which has more degrees of freedom than that of the element used in ANSYS®. This may be the main cause of dispersion between buckling load values. The difference between the boundary conditions imposed in the analytical solution using Ritz method and numerical solution using ANSYS® may also be a reason for the disagreement between the results obtained using Ritz method and ANSYS®.

The results obtained using FST based Ritz solution given in the Table 3.5 are normalized and compared with that of the CST based Ritz solution (Refs. [111-112]) in the Fig. 3.7.

In this figure, R denotes the radius, h_{tk} denotes the thickness at the thick end, λ_{cr} denotes the critical buckling load, L_{tap} denotes the length of taper section and $E_{x"}$ denotes the elastic modulus of composite ply material in the longitudinal direction.

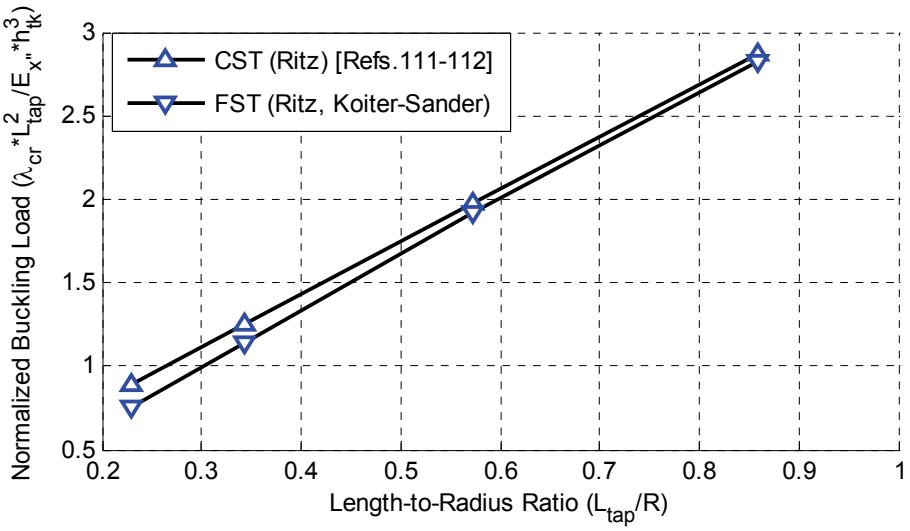

Figure 3.7: Effect of length-to-radius ratio on buckling coefficient of the clamped-clamped tapered curved plates with the lay-up configuration LC_1 and the taper configuration B.

The normalized buckling load called herein as the buckling coefficient decreases with the decrease of length-to-radius ratio of the tapered curved plate. The buckling coefficient calculated based on FST deviates away from that of CST with the increase of thickness of the plate as the rotations (φ_x and φ_y) due to shear deformation play an important role. The difference between the critical buckling loads calculated using FST and CST is close to 10% corresponding to the moderately-long plate (L_{tap}/R = 0.35). This difference increases with the decrease of length-to-radius ratio (L_{tap}/R) as the plate becomes shorter.

3.6.2 Buckling Analysis of Hybrid Curved plates

Laminates with only taper configuration have been studied in the previous sections of the present chapter. The hybrid configuration (consisting of both tapered and uniform-thickness sections) is taken into account in the present sub-section. The tapered section of hybrid plate is considered to have the taper configuration B. For the analysis of hybrid configuration three types of lay-up configurations, namely LC_1, LC_2 and LC_3 given in the Table 2.7 are considered. For the buckling analysis, the total plate length L = 229.2 mm, width b = 114.6 mm and the material properties given in the Tables 2.5 and 2.6 are considered. According to the first-ply failure analysis, the hybrid plates with the above mentioned lay-up configurations will not fail by first-ply failure before global buckling. Various parameters, namely the stiffness ratio, radius-to-thickness ratio and boundary conditions are investigated as to their influences on the critical buckling load of hybrid curved plate. With the increase of radius-to-thickness ratio, the plate becomes more flat as the radius is increased without changing the thickness at the thick end. The results are shown in the following Figs. 3.8 through 3.17.

3.6.2.1 The effect of the stiffness ratio

The variations of critical buckling load of hybrid type plate (Fig. 1.4) are shown in the Fig. 3.8 as a function of stiffness ratio $E_{x"}/E_{y"}$ for each lay-up configuration. The results were obtained by changing the value of $E_{x"}$. In the Fig. 3.8, $E_{x"}$ and $E_{y"}$ denote, respectively, the elastic moduli of composite ply material in the fiber direction and in the transverse to the fiber direction. As was expected, the critical buckling loads in all the three cases increase linearly with increasing stiffness ratio values. For the lower values of stiffness ratio, the values of the critical buckling loads of all the three lay-up

configurations are very close to each other. But for higher values of stiffness ratio the critical buckling loads of the three lay-up configurations differ much between themselves. The influence of shear deformation is characterized in the Fig. 3.8. This effect is more pronounced in the case of LC_1.

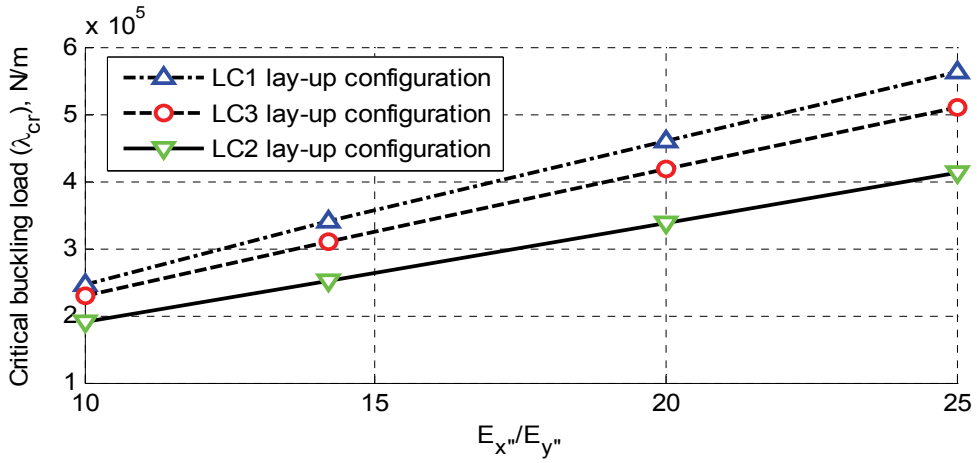

Figure 3.8: Effect of stiffness ratio on the critical buckling load of the clamped-clamped (C4-C4) hybrid curved plates.

3.6.2.2 Influence of Lay-Up Configuration

The normalized critical buckling loads (called as buckling coefficient) of three lay-up configurations LC_1, LC_2 and LC_3 are calculated using the present FST based Ritz solution and ANSYS®, and the buckling coefficients are compared in the Figs. 3.9 - 3.11. The buckling loads are calculated for clamped-clamped (C4-C4) boundary conditions. The taper configuration B is considered for the taper section. The effect of radius-to-thickness ratio on the buckling coefficient is evaluated in the Figs. 3.9 - 3.11. In these figures, R denotes the radius, h_{tk} denotes the thickness at thick end, λ_{cr} denotes the critical buckling

load, L denotes the total length of hybrid plates and $E_{x"}$ denotes the elastic modulus of composite ply material in the fiber direction. From Figs. 3.9 - 3.11, the following observations are made:

a) The lay-up configuration LC_2 is the weakest one among all lay-up configurations.

b) The rate of change of buckling coefficient of lay-up configuration LC_3 is lesser than that of lay-up configuration LC_1. The buckling coefficient of LC_1 is higher than that of LC_3 for smaller values of radius-to-thickness ratio ($R/h_{tk} < 230$ for clamped-clamped plate and $R/h_{tk} < 250$ for simply-supported plate). In the case of larger values of radius-to-thickness ratio ($R/h_{tk} > 230$ for clamped-clamped plate and $R/h_{tk} > 250$ for simply-supported plate), LC_3 is stronger than LC_1.

c) In all the cases, the value of the buckling coefficient decreases nonlinearly with the increase of radius-to-thickness ratio. The values of buckling coefficient become close to each other at larger values of R/h_{tk} ratio as the plate becomes flatter. In the case of plate with larger radius, the effect of radius has less influence on the buckling coefficient and the buckling behavior of the plate largely depends on the orientation of fiber angle. For uniaxial compressive load, the fibers parallel to the direction of the applied load are the strongest ones and the fibers perpendicular to the direction of the applied load are the weakest ones. A quantitative comparison of relative stiffness of three lay-up configurations is given in the Table 3.6. Lay-up configuration LC_3 is the strongest as it is made of two types of plies: moderately stiff plies and stiffest plies. Lay-up configuration LC_2 is the weakest one as it is constructed of the moderately stiff plies only. On the other hand, lay-up configuration LC_1 is the moderately stiff as two extreme types of plies namely, the weakest plies and strongest plies, are used to construct it.

d) The buckling behavior of all the lay-up configurations is strongly influenced by R/h_{tk}.

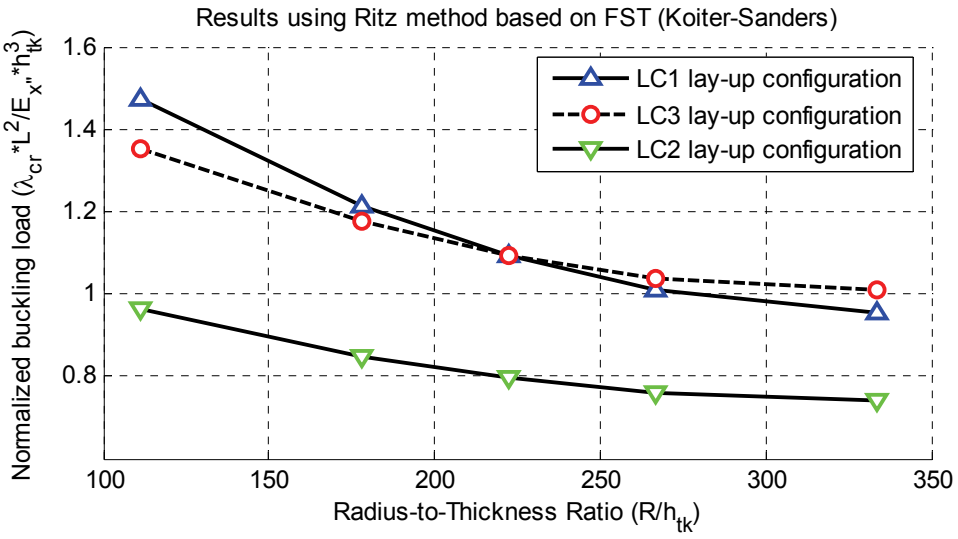

Figure 3.9: Variations of critical buckling load with the radius-to-thickness ratio for the clamped-clamped (C4-C4) hybrid laminates with different lay-up configurations.

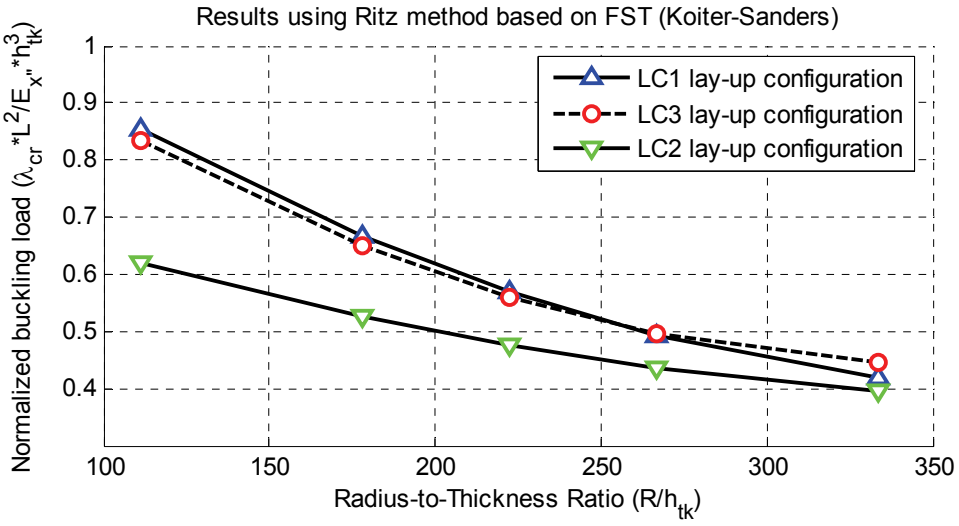

Figure 3.10: Variations of critical buckling load with the radius-to-thickness ratio for simply-supported (S4-S4) hybrid laminates with different lay-up configurations.

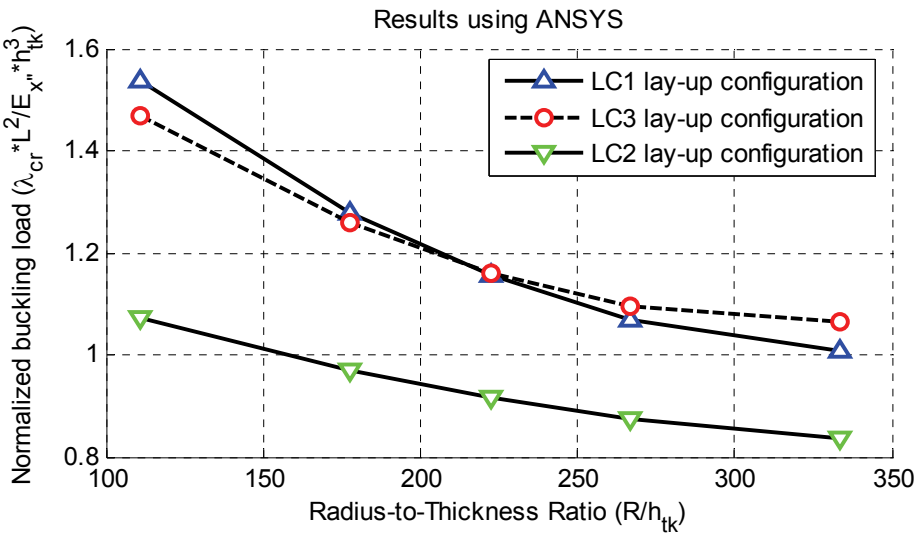

Figure 3.11: Variations of critical buckling load with the radius-to-thickness ratio for the clamped-clamped (C4-C4) hybrid laminates with different lay-up configurations.

Table 3.6: Qualitative comparison of stiffness properties of lay-up configurations for higher values of radius-to-thickness ratio

	Fiber Orientation			Remark
	90^0	$\pm45^0$	0^0	
Stiffness for Uniaxial End Compression	Weakest	Moderate	Strongest	
No. of plies in LC_1	6	0	6	Moderate Configuration
No. of plies in LC_2	0	6+6	0	Weakest Configuration
No. of plies in LC_3	0	4+4	4	Strongest Configuration

Figs. 3.12 – 3.14 show the effect of the radius-to-thickness ratio on normalized critical buckling loads. The normalized critical buckling loads corresponding to different values of radius-to-thickness ratio of hybrid curved plates are calculated using FST based Ritz solution and the buckling loads thus obtained are compared with that obtained using CST

based Ritz solution and using ANSYS®. From Figs. 3.12 – 3.14, the following observations are made:

a) The normalized critical buckling loads of all lay-up configurations decrease with the increase of radius-to-thickness ratio of the plate.

b) The lowest and highest values of buckling coefficients are obtained based on FST and CST respectively. The buckling coefficients calculated using ANSYS® are close to that of CST solution. In ANSYS® an 8-node shell element (SHELL99) is considered based on the degenerated solid approach but the Ritz solution is developed based on FST which has more degrees of freedom than the element used in ANSYS®. This is the reason for higher values of buckling coefficient obtained using ANSYS®. In the case of classical shell theory (CST), shear strains are omitted which is the cause for the corresponding higher value of buckling coefficient compared to that of the other two solutions.

c) On an average, buckling coefficient of all lay-up configurations (Figs. 3.12–3.14) obtained based on CST is 5.8% higher than that obtained using ANSYS®. On the other hand, buckling coefficients of LC_1, LC_2 and LC_3 obtained based on FST are, respectively, 5.22%, 13.51% and 9.38% lower than that obtained using ANSYS®.

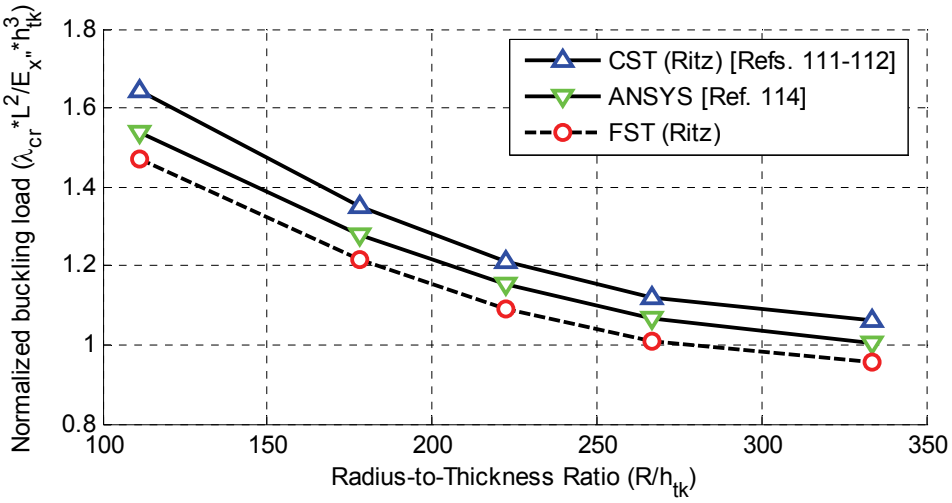

Figure 3.12: Variations of buckling coefficient with the radius-to-thickness ratio for the clamped-clamped (C4-C4) hybrid laminates with LC_1 lay-up configuration.

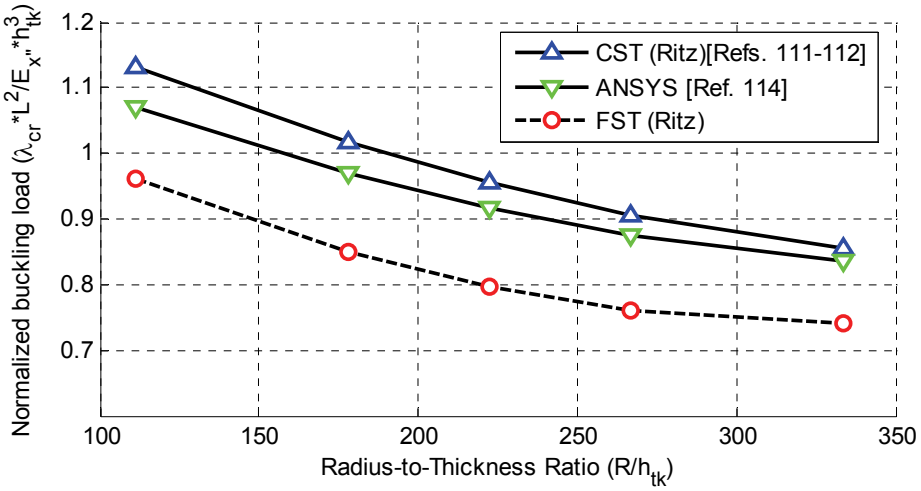

Figure 3.13: Variations of buckling coefficient with the radius-to-thickness ratio for the clamped-clamped (C4-C4) hybrid laminates with LC_2 lay-up configuration.

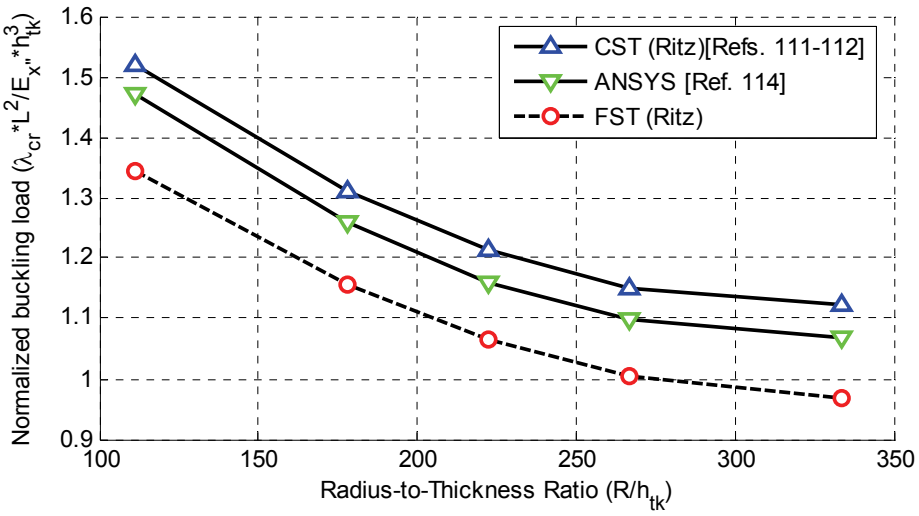

Figure 3.14: Variations of buckling coefficient with the radius-to-thickness ratio for the clamped-clamped (C4-C4) hybrid laminates with LC_3 lay-up configuration.

3.6.2.3 Influence of Boundary Conditions

Normalized critical buckling loads are calculated for the rectangular hybrid laminated curved plates (with a length/width ratio of 2.0) under uniaxial compression. The buckling analyses are performed using Ritz method based on Koiter-Sanders shell theory. Two boundary conditions are considered, that are, clamped at four edges (C4-C4) and simply-supported at four edges (S4-S4). These boundary conditions are given in the Appendix B. The effect of boundary condition on the buckling coefficient for the above mentioned plates is shown in the Figs. 3.15 – 3.17.

As observed from Figs. 3.15 – 3.17 and as can be expected, the boundary condition has significant influence on the buckling coefficient. In terms of critical buckling load, the fully clamped plate has a higher buckling load than the simply-supported plate. Simply-

supported plates allow rotations at the boundaries which is the reason for less strength. For lay-up configuration LC_1 as can be seen in the Fig. 3.15, the buckling coefficient difference between the values of that correspond to the clamped-clamped plate and the simply-supported plate is in the range of about 42.66% - 53.14% and the average difference is 45.17%. In the case of lay-up configuration LC_2 as can be seen in the Fig. 3.16, the buckling coefficient difference between the values of that correspond to the clamped-clamped plate and the simply-supported plate is in the range of about 35.02% - 46.83% and the average difference is 39.94%. On the other hand for the lay-up configuration LC_3 as can be seen in the Fig. 3.17, the buckling coefficient difference between the values of that correspond to the clamped-clamped plate and the simply-supported plate is in the range of about 36.22% - 54.58% and the average difference is 44.84%. Buckling coefficients of all the lay-up configurations are strongly influenced by both R/h_{tk} ratio and boundary condition.

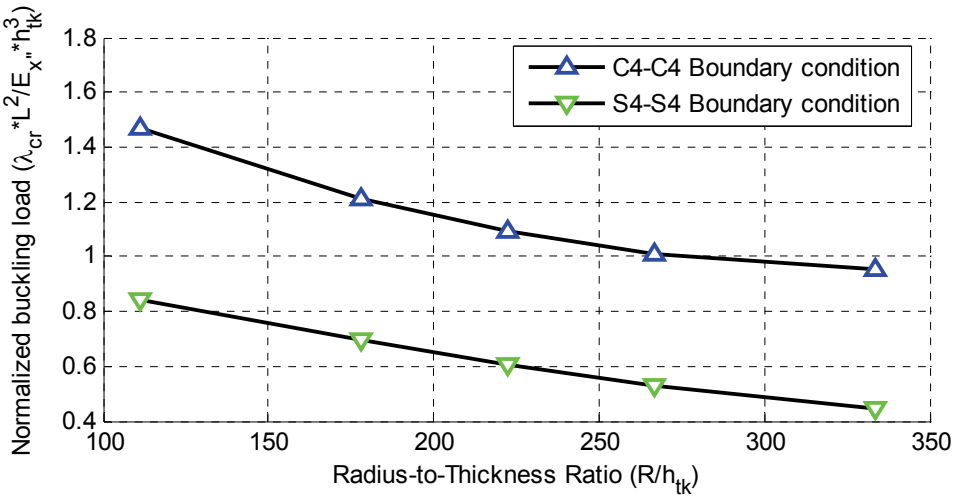

Figure 3.15: Comparison of buckling coefficient of the hybrid laminate with LC_1 lay-up configuration for different boundary conditions.

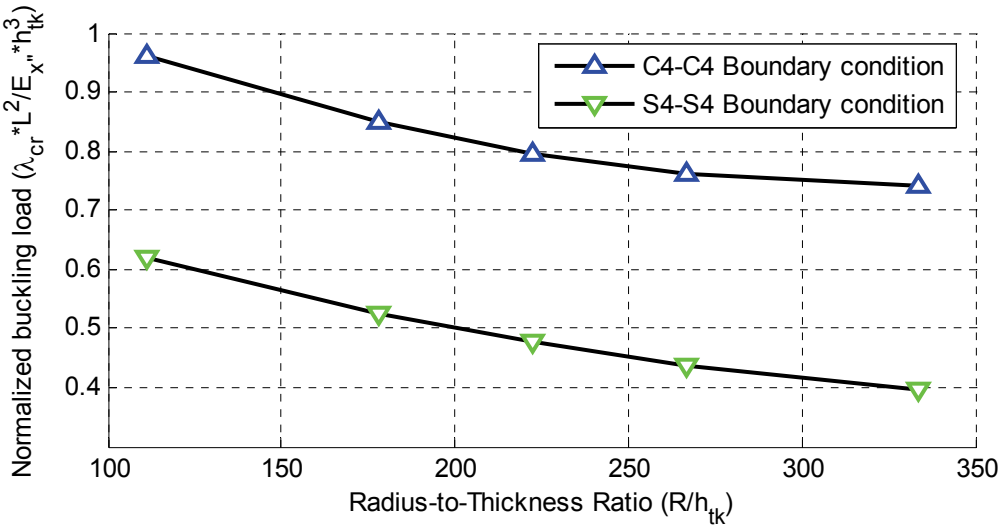

Figure 3.16: Comparison of buckling coefficient of the hybrid laminate with LC_2 lay-up configuration for different boundary conditions.

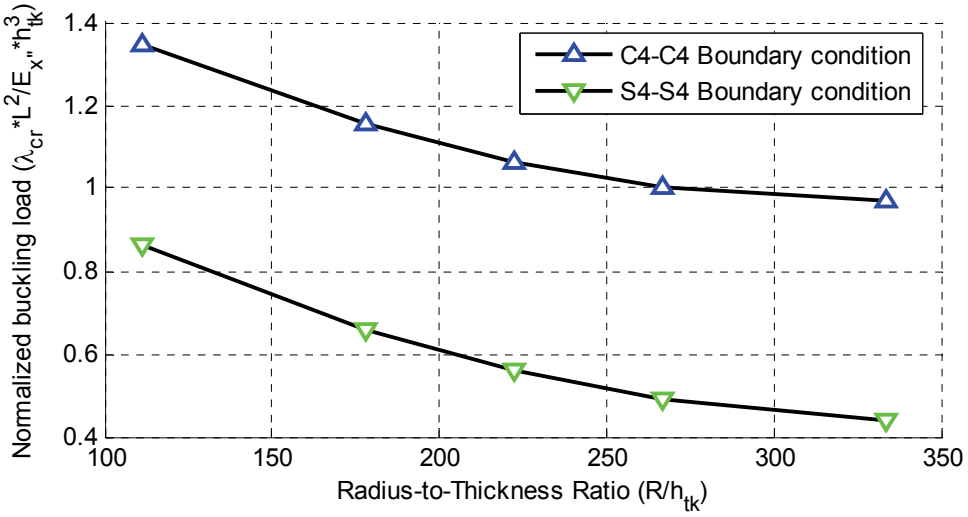

Figure 3.17: Comparison of buckling coefficient of the hybrid laminate with LC_3 lay-up configuration for different boundary conditions.

3.7 CONCLUSIONS

In the present chapter, the global buckling analysis of tapered curved laminated plates has been carried out using Ritz method based on six well-established first-order shallow shell theories, namely, Donnell's, Moreley's, Love's, Loo's, Koiter's and Sander's theories. Three types of tapered plates (two taper configurations A and B, and a hybrid configuration), three types of lay-up configurations (LC_1, LC_2 and LC_3), and uniaxial end compressive load are considered. A detailed parametric study of the plates has been conducted that includes the effects of boundary conditions, stacking sequence, taper configurations, radius, and geometric parameters of the plates. The conclusions listed in the following are based on the results presented in this chapter:

a) The moderately-thick and tapered curved composite plates fail by first-ply failure before global buckling. Therefore the dimensions of tapered curved plate should be larger than the corresponding critical size. The critical sizes depend on both radius and staking sequence of the plates. Such critical sizes have been determined in the present work.

b) The tapered flat plate is more flexible than uniform flat plate, but the tapered curved plate provides a better design option in terms of saving the material without any compromise of the strength.

c) The critical buckling loads of all lay-up configurations are considerably influenced by the stiffness ratio ($E_{x''}/E_{y''}$) of the ply material.

d) Classical shell theory can be used to calculate with reasonable accuracy the critical buckling load of moderately-long plates for which $L_{tap}/R > 0.35$. The first-order shear deformation shell theory should be used for the calculation of critical buckling load of shorter plates for which $L_{tap}/R < 0.35$.

Chapter 4

Compressive Response of Tapered Curved Composite Plates Based on a Nine-Node Composite Shell Element

4.1 INTRODUCTION

The prime objective of the present chapter is to conduct the linear global buckling analysis of the tapered curved plates (see Fig. 1.4) using finite element method based on first-order shear deformation shell theories. Six shell theories are used in the analysis, that are, Donnel's, Moreley's, Love's, Loo's, Koiter's and Sander's theories. The corresponding critical buckling loads are calculated and the most conservative value is obtained. The appropriate set of shear correction factors are determined as like chapter three and used in the buckling analyses. Buckling loads calculated using the finite element method are compared with that of the existing experimental results and analytical results for tapered curved composite plates based on Ritz solutions (which have been calculated in the chapters two and three). A parametric study that encompasses the influences of taper angle, length-to-radius ratio, stiffness ratio, stacking sequence, boundary conditions, radius and geometric parameters of the plates on the critical buckling load is conducted.

4.2 FORMULATION

The basic formulation based on first order shear deformation has been described in the chapter three using the Eqs. (3.1) through (3.10). In the Eq. (3.10a), three Shear

Correction (SC) factors S_1, S_2 and S_3 are given. The set of SC factors in Eq. (3.11) that corresponds to the most conservative value of critical buckling loads is reevaluated using the present FEM. This particular set of values is used further onwards throughout the present work. For this purpose, a tapered plate with configuration B and having 36 layers at the thick end with $[0/90]_{9s}$ lay-up and 12 layers at the thin end with $[0/90]_{3s}$ lay-up, that is subjected to uni-axial end compressive loading has been analyzed using FEM method. The plate is clamped at four edges (C4-C4) and the boundary conditions represented as C4 are given in the Appendix C. The dimensions of the square plate are (see Fig. 1.4): various values of the side length of the plate in the range of from 85.94 mm to 171.90 mm are considered, plate thickness at the thick end h_{tk} = 4.5 mm and the radius R = 500 mm. The material properties of the composite ply and epoxy are the same as given in Tables 2.5 and 2.6 respectively. The critical buckling loads using these properties are calculated and presented at the end of this section.

The total potential energy is expressed as the sum of strain energy U and the potential energy of external load W. For a plate of dimension $L_{tap} \times b$ subjected to uni-axial compression λ,

$$U = \frac{1}{2}\int_0^b \int_0^{L_{tap}} \left(\{\varepsilon\}^T \left[E'\right] \{\varepsilon\} \right) dxdy \tag{4.1}$$

where

$$\{\varepsilon\} = [\varepsilon_{xx}^0 \quad \varepsilon_{yy}^0 \quad \gamma_{xy}^0 \quad \kappa_{xx}^0 \quad \kappa_{yy}^0 \quad \kappa_{xy}^0 \quad \gamma_{yz}^0 \quad \gamma_{xz}^0]^T \tag{4.2}$$

and $[E']$ is the stiffness matrix given in Eq. (3.10b).

$$W = -\lambda \int_0^b \int_0^{L_{tap}} \frac{1}{2}\left(\frac{\partial w_o}{\partial x}\right)^2 dxdy \tag{4.3}$$

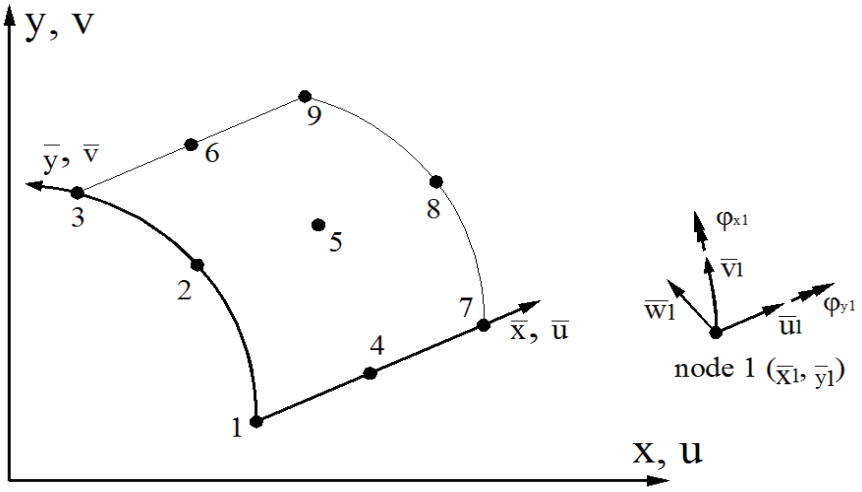

Figure 4.1: The nine-node shell element

The nine-node Lagrange shell element with five degrees of freedom per node shown in Fig. 4.1 is used in the present analysis. The five degrees of freedom are: the translation displacements in x, y and z directions that are *u*, *v* and *w* respectively, and rotations about y and x axes that are φ_x and φ_y respectively which are due to shear deformation. The displacement fields and rotations are defined as:

$$u = \sum_{i=1}^{9} \overline{N}_i u_i ; \quad v = \sum_{i=1}^{9} \overline{N}_i v_i ; \quad w = \sum_{i=1}^{9} \overline{N}_i w_i ; \quad \varphi_x = \sum_{i=1}^{9} \overline{N}_i \varphi_{xi} ; \quad \varphi_y = \sum_{i=1}^{9} \overline{N}_i \varphi_{y_i} \qquad (4.4)$$

where $\overline{N}_i(x, y)$ are the Lagrange shape functions. The shape functions are given in the Appendix C.

The matrix of strains and curvatures, $\{\varepsilon\}$, is expressed as:

$$\{\varepsilon\} = \left[\bar{B}_L^i\right]\{\bar{u}_e\} \qquad (4.5a)$$

where

$$\left[\bar{B}_L^i\right] = \left[[\bar{B}_L^1][\bar{B}_L^2] \ldots\ldots\ldots\ldots [\bar{B}_L^9]\right] \qquad (4.5b)$$

$$\{\bar{u}_e\} = [u_1, v_1, w_1, \varphi_{x1}, \varphi_{y1} \ldots\ldots\ldots\ldots\ldots\ldots\ldots\ldots\ldots u_9, v_9, w_9, \varphi_{x9}, \varphi_{y9}]^t \qquad (4.5c)$$

The matrix $\left[\bar{B}_L^i\right]$ is given in the Appendix C where i = 1, 2, 3 … 9.

The first variations of strain energy *U* and potential energy *W* that are given, respectively, by the Eqs. (4.1) and (4.3) are considered. For an element they are expressed as

$$\partial \mathrm{U_e} = \partial\{\bar{u}_e\}^t[K_e]\{\bar{u}_e\} \tag{4.6}$$

$$\partial \mathrm{W_e} = \partial\{\bar{u}_e\}^t[G_e]\{\bar{u}_e\} \tag{4.7}$$

where $\{\bar{u}_e\}$ is the element nodal displacement matrix. The element stiffness matrix $[K_e]$ and the element geometric stiffness matrix $[G_\mathrm{e}]$ are given by

$$[K_e] = [\int_\Omega \left[\bar{B}_L^i\right]^t [E'] \left[\bar{B}_L^i\right] d\Omega]_{45\times 45} \tag{4.8}$$

$$[G_e] = [\int_\Omega \left[\bar{g}_L^i\right]^t \left[\bar{g}_L^i\right] d\Omega]_{45\times 45} \tag{4.9}$$

The matrix $\left[\bar{g}_L^i\right]\{\bar{u}_e\}$ is given in the Appendix C. The equilibrium equation of an element is expressed as:

$$\frac{\partial U_e}{\partial \bar{u}_e} = \frac{\partial W_e}{\partial \bar{u}_e} \tag{4.10}$$

The Eq. (4.10) is simplified using the Eqs. (4.6) through (4.9):

$$\left| \sum [K_e] + \bar{\lambda} \sum [G_e] \right| = 0 \tag{4.11}$$

where the eigenvalues $\bar{\lambda}$ are the values of buckling loads. The element stiffness matrix $[K_e]$ and the element geometric stiffness matrix $[G_\mathrm{e}]$ are augmented considering all of the elements in the plate. Eq. (4.11) is solved using MATLAB® as an eigenvalue problem. The smallest value of $\bar{\lambda}$ is the critical buckling load, λ_{cr}.

The critical buckling loads corresponding to different values of shear correction factors are plotted in the Figs. 4.2 and 4.3. It can be seen from these figures that the critical buckling loads corresponding to all the six sets of shear correction factors are close to each other for lower values of taper angle. On the other hand, at higher values of taper angle, the values of the critical buckling loads differ relatively much. Among all the cases, the set (S_1=1, S_2=5/6, S_3=5/6) in the Eq. (3.11c) is the most conservative one in terms of critical buckling load. Similar conclusion has also been made using Ritz solution in the chapter three and this set of shear correction factors will be used further onwards in the present work.

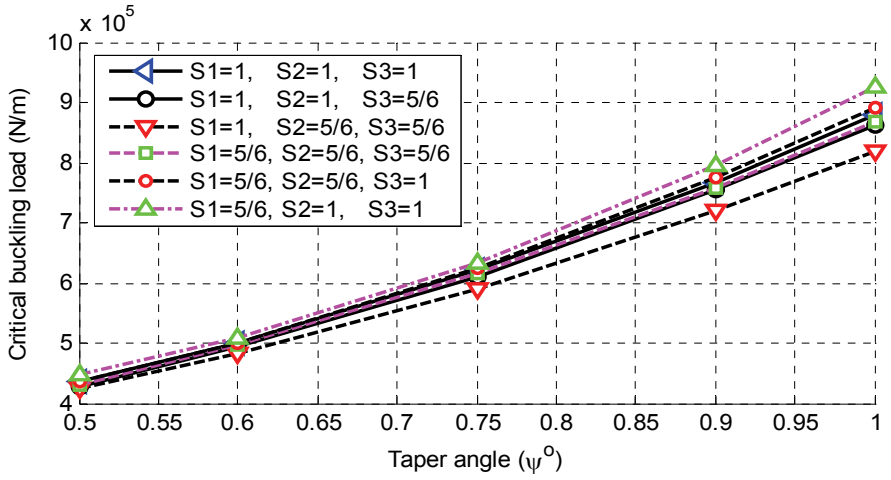

Figure 4.2: Comparison of critical buckling load obtained using six sets of SC factors for the clamped-clamped laminate with the configuration B based on Koiter-Sanders shell theory.

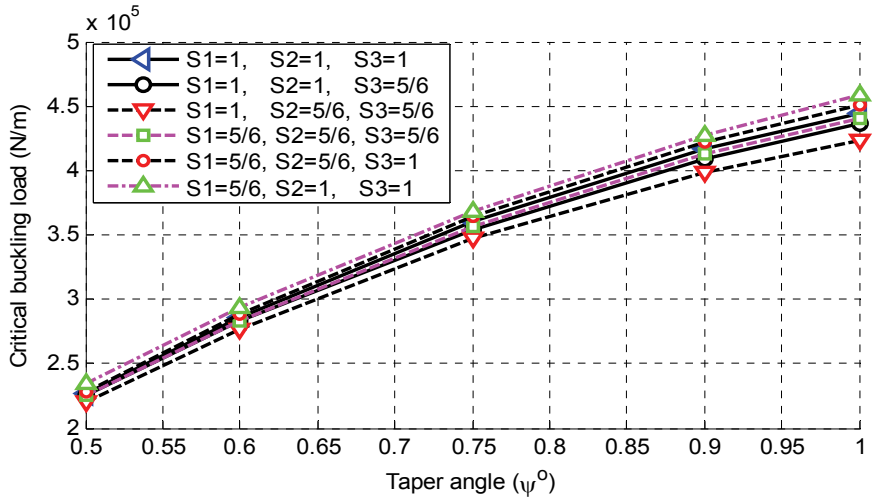

Figure 4.3: Comparison of critical buckling load obtained using six sets of SC factors for the simply-supported laminate with the configuration B based on Koiter-Sanders shell theory.

4.3 VALIDATION

To the authors' knowledge, no results are available yet in the literature on the buckling loads of the tapered curved composite plates under the action of uni-axial compression except the other contemporary works of the present author. Therefore the comparison with the existing works of other researchers could not be made. However, in order to validate the formulation and analysis, first, the taper angle is set to be zero, and the resulting uniform-thickness curved plates have been analyzed and the results have been compared with that available in the literature for the uniform-thickness plates. For this reason, an isotropic cylindrical panel [115] is investigated which is subjected to uniformly distributed transverse (normal to the surface) load q, and the geometric and materials properties are: width $b = 2\times R\times\alpha$ (α = 0.1 rad.), radius R = 2.54 m (100 in.), length L = 0.508 m (20 in.), thickness $h = 3.175\text{x}10^{-03}$ m (0.125 in.), elastic modulus E = 3.10 GPa (0.45×10^{6} psi), Poisson ratio υ = 0.3, and transverse load q = 275.79 Pa (0.04

psi). In the Ref. [115] two sets of uniform meshes, one with 81 nodes (405 degrees of freedom) and the other with 289 nodes (1,445 degrees of freedom), have been used with different p (degree of polynomial) levels considering symmetric boundary conditions.

Table 4.1: Vertical displacement at the center ($-w\times10^2$ m) of the clamped-clamped (C4-C4) cylindrical panel under transverse load

Type of element	Present	Reddy [115]					
		Mesh of 81 nodes			Mesh of 289 nodes		
		Full Integration	Selective Integration	Reduced Integration	Full Integration	Selective Integration	Reduced Integration
4-node	...	0.00858	0.02937	0.02941	0.01894	0.02896	0.02897
9-node	*0.02902*	0.02977	0.02883	0.02883	*0.02902*	0.02883	0.02883
25-node	…	0.02882	0.02883	0.02883	0.02883	0.02883	0.02883
81-node	…	0.02883	0.02882	0.02882	0.02882	0.02883	0.02883

The vertical displacement at the center of the shell is calculated considering symmetric boundary conditions and is compared in the Table 4.1. From the Table 4.1, it has been observed that the present result exactly matches with that of the reference. As can be seen from the Table 4.2 that the results based on different shell theories are close to each other but the Koiter-Sanders shell theory provides the lowest result for deflection. It is also shown in Table 3.1 that Koiter-Sanders shell theory provides the most conservative result for critical buckling load.

Table 4.2: The comparison of vertical displacement at the center ($-w\times10^2$ m) for uniform-thickness clamped-clamped (C4-C4) cylindrical plate

Reddy [115] (m)	Present (m)		
	Donnell, Morley	Sander, Koiter	Love, Loo
0.0290	0.0292	0.0290	0.0291

Next, a tapered plate with only two (one above and corresponding one below the mid plane) internally-dropped plies has been analyzed using finite element method based on Koiter-Sanders shell theory. A uniform-thickness cylindrical panel [107] made of T300/5208 graphite/epoxy having the mechanical properties of $E_{x"}$ = 141.34 GPa (20.5 x10^6 psi), $E_{y"}$ = 8.96 GPa (1.3 x10^6 psi), $G_{x"y"}$ = 5.17 GPa (0.75 x10^6 psi), $\upsilon_{x"y"}$ = 0.335; clamped (C3) in transverse direction (at x = 0, L) and simply supported (S3) in longitudinal direction (at y = 0, b) are considered. The boundary conditions C3 and S3 are given in the Appendix C. The dimensions of the plate are taken to be: the length L = 0.3048 m (12 inches), the cord length b' = 0.3048 m, the radius R = 0.3048 m, the thickness h = 1.016x10^{-03} m (0.04 inches). Becker [107] has conducted the bifurcation (obtained from eigenvalue solution) buckling analysis of this curved plate using STAGS computer code. Akhlaque and Ganesan [116] have conducted the linear global buckling analysis of this plate using Ritz method based on Koiter-Sanders shell theory. The results are also compared with that of the two uniform-thickness composite plates with lay-up configurations $[90/0]_{2s}$ and $[90/0/90]_s$, respectively. The buckling loads for these three laminates under uni-axial end compressive load are given in Table 4.3. As can be observed from this table, the result for tapered laminate is between that of the 8-layers uniform-thickness laminate and that of the 6-layers uniform-thickness laminate. The present result has also good agreement with that of the references.

Table 4.3: Critical buckling loads for tapered and uniform-thickness composite plates

Plate Type	Buckling Load $(\lambda_{cr} L^2)/(E_{x"} h^3)$		
	Present	Becker [107]	Akhlaque and Ganesan [116]
8-Layers Uniform Plate, $[90/0]_{2s}$	34.90	33.30	34.70
Tapered Plate, $[90/0]_{2s}$ - $[90/0/90]_s$	25.30	-	-
6-Layers Uniform Plate, $[90/0/90]_s$	18.32	-	-

4.4 PARAMETRIC STUDY

In the parametric study three types of longitudinal cross-sections of the curved plates are considered, that are, taper configurations A and B, and a hybrid configuration as shown in the Fig. 1.4. The finite element method is used based on Koiter-Sanders shell theory. The material properties of composite ply and epoxy used are the same as given in the Tables 2.5 and 2.6 respectively. Based on the convergence test, the mesh size used for the finite element analyses of taper configuration and hybrid configuration are 9×9 and 15×15 respectively. The 9×9 finite element mesh is shown in the Fig. 4.4.

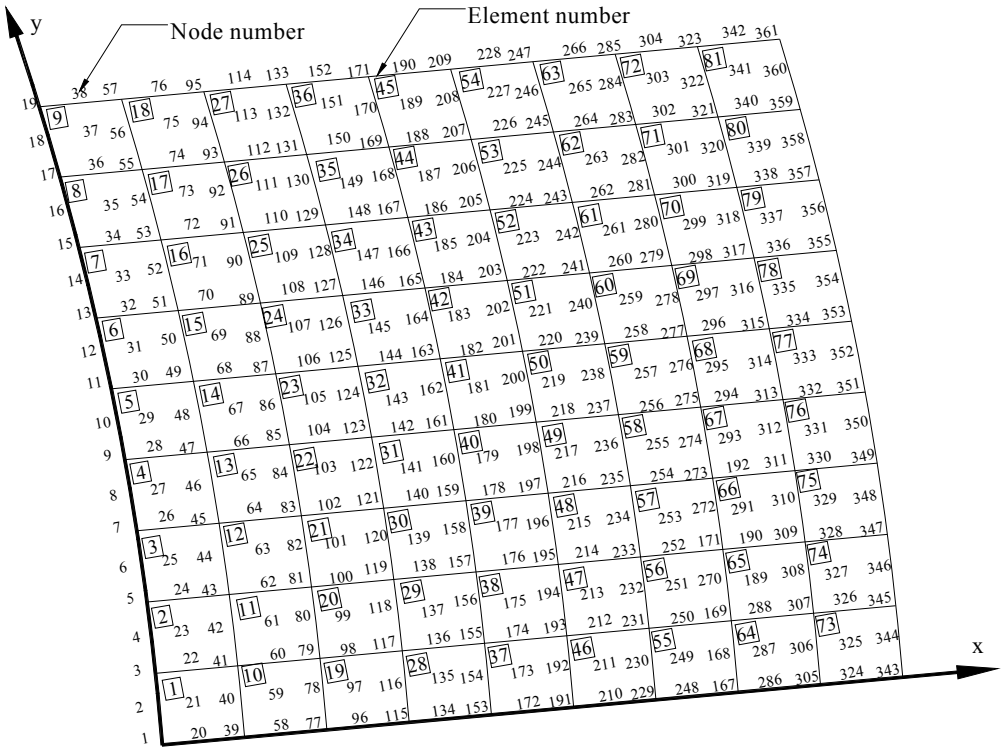

Figure 4.4: The 9×9 finite element mesh for the tapered curved plate

4.4.1 Buckling Analysis of Tapered Curved Plates

Tapered models shown in the Fig. 1.4 are considered with 36 and 12 plies at the thick end and the thin end respectively, which results in 24 drop-off plies. The configuration at the thick end is $(0/90)_{9s}$, and that of the thin end is $(0/90)_{3s}$ (this lay-up configuration is referred to as LC_1 in the Table 2.7). In the analyses of taper configurations, the thickness of the thick end h_{tk} is set to be 4.5 mm and the radius of the curved plate R is set to be 500 mm. For all the taper configurations only LC_1 lay-up configuration with clamped-clamped (C4-C4) boundary conditions is considered. In Table 4.4 the number of elements of taper configuration B was determined based on mesh convergence test. Various parameters, namely ply drop-off parameters, taper angle, stiffness ratio and length-to-radius ratio are investigated to see the influences of these parameters on the buckling loads of tapered curved plates. The results are shown in the following Figs. 4.5 through 4.10.

Table 4.4: Effect of mesh size on the critical buckling load of tapered curved plate with taper configuration B and LC_1 lay-up configuration (taper angle = 0.5 degree and radius = 500 mm)

Mesh	9 x 7	9 x 8	9 x 9
λ_{cr} ($\times 10^4$ N/m)	87.2299	87.1570	87.1162

4.4.1.1 Influence of Ply Drop-Off

The effect of ply drop-off on critical buckling load is shown in the Figs. 4.5 and 4.6. To investigate this effect, the side length of square tapered plate is considered as 859.4 mm corresponding to a taper angle of 0.1 degree. The thickness of the thick end is not

changed and the taper angle is varied with the corresponding increase in the number of drop-off plies. The plate can be considered as a uniform-thickness plate when the number of ply drop-off is set to zero and the taper configuration A is obtained by dropping off twenty four plies. The plates are clamped (C4-C4) at four edges and the lay-up configuration is LC_1. In the Figs. 4.5 and 4.6, λ_{cr} denotes the critical buckling load.

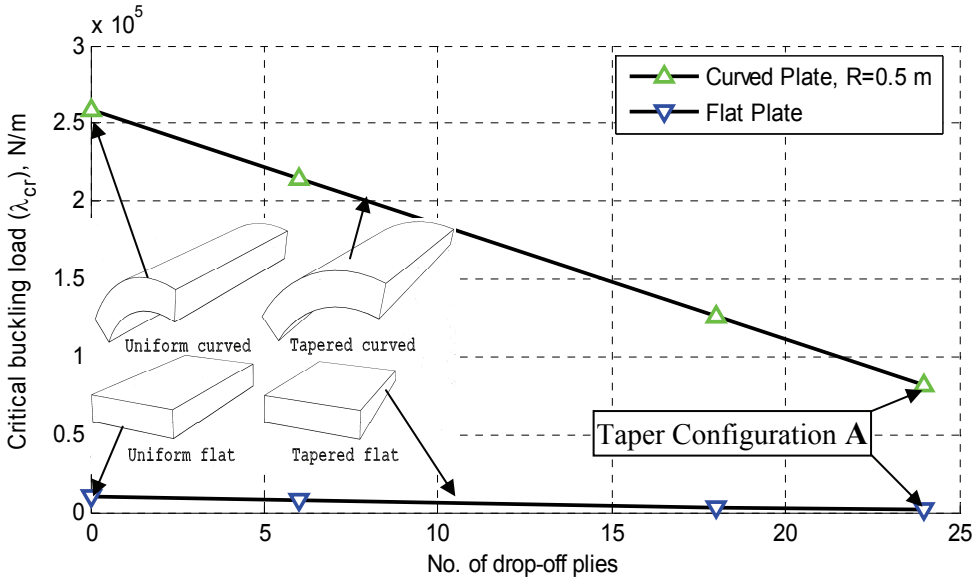

Figure 4.5: The effect of ply drop-off on critical buckling load for simply-supported plates.

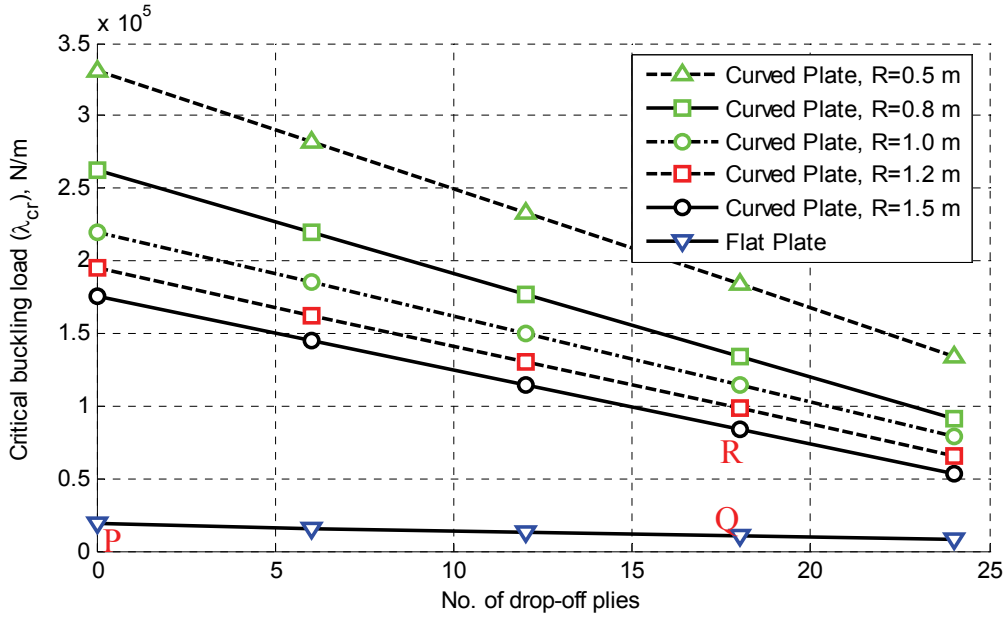

Figure 4.6: The effect of ply drop-off on critical buckling load for clamped-clamped plates.

From the Figs. 4.5 and 4.6, it is observed that the uniform-thickness curved plate is many times stiffer than the uniform-thickness flat plate in terms of buckling behavior. It is also observed that the tapered flat plate is less stiff than uniform flat plate. However, this strength reduction can be compensated for if the tapered plate is made into a curved one. It can be concluded from the Figs. 4.5 and 4.6 that the tapered curved plate provides a better design option in terms of saving the material without any compromise of the strength. Buckling loads of flat and curved plates vary linearly with the number of ply drop-off. The weight savings of the tapered plate with respect to the uniform plate is expressed as:

$$W_s = (W^P - W^Q)/W^P \times 100\% \tag{4.12}$$

where W^P and W^Q are the weights corresponding to the points marked as 'P' and 'Q' respectively in Fig. 4.6.

The gain of strength of the curved tapered plate with respect to the flat tapered plate can be expressed as:

$$G_s = (S^R - S^Q)/S^Q \times 100\% \tag{4.13}$$

where S^{Q} and S^{R} are the strengths corresponding to the points marked as 'Q' and 'R' respectively in Fig. 4.6.

Based on the Eq. (4.12), it is calculated that 21.96% weight can be saved by dropping-off 18 plies (corresponding to the location of 'Q' in the Fig. 4.6). The gain of strength of the curved tapered plate with respect to the flat tapered plate is calculated by the Eq. (4.13). Considering the strength property shown in Fig. 4.6, the gain of strength of the tapered curved plate (corresponding to the location of 'R') with respect to the flat tapered plate (corresponding to the point 'Q') is 82.47%. The details of the calculations are given in the Appendix C. Similar conclusions have also been arrived at for other taper configurations. Similar type of effect is presented in previous chapters in Figs. 2.4 and 3.5, where the buckling loads are calculated based on CST-based and FST-based Ritz solution respectively. In Fig. 2.4, the buckling loads for both of the uniform and curved plates are 0.80 % higher than that of the present FST-based FEM solution (Fig. 4.6). On the other hand, the buckling loads shown in Fig. 3.5 are 0.46 % lower than that of the present FST-based FEM solution (Fig. 4.6).

4.4.1.2 Influence of Taper Angle

The effect of taper angle of the curved plates on the critical buckling load is compared with that of obtained CST based Ritz solution and FST based Ritz solution. The comparison is shown in the Fig. 4.7 where the size of the plate is decreased with the

increase of taper angle while keeping the thickness of the thick section unchanged. The maximum and minimum edge lengths of the tapered curved square plate are 859.4 mm corresponding to a taper angle of 0.1 degree and 85.94 mm corresponding to a taper angle of 1.0 degree respectively. In the Fig. 4.7, λ_{cr} denotes the critical buckling load.

As can be observed from Fig. 4.7, the critical buckling load using three different methods increases as the taper angle is increased, because the plate becomes shorter (without changing the thickness) with the increase of taper angle. The buckling loads in the Refs. [112] and [116] are, respectively, calculated using Ritz method based on CST and FST. The buckling results FST based FEM solution are close to FST based Ritz solution as the both of these methods are based on first-order shear deformation theory. At lower values of taper angle, buckling loads obtained using different methods do not vary significantly. On the other hand, at the higher values of taper angle the critical buckling loads obtained using three different methods differ relatively much. It can also be observed that in all the three cases, the critical buckling load varies nonlinearly with the variation of taper angle.

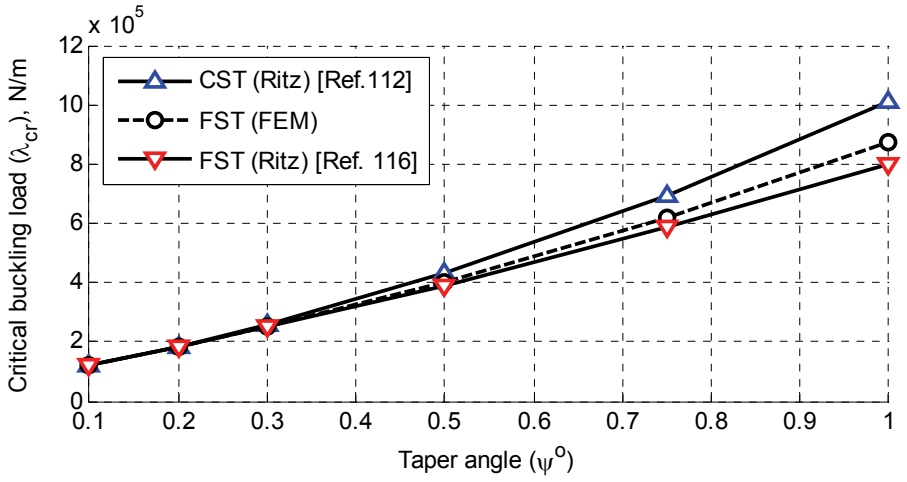

Figure 4.7: Effect of taper angle on the critical buckling load for clamped-clamped tapered curved plate with the taper configuration B and the LC_1 lay-up configuration.

4.4.1.3 Influence of Length-to-Radius Ratio

The normalized buckling loads of the plates of different sizes are calculated and compared with that of CST (Ritz) [112] and FST (Ritz) [116]. The lay-up configuration is LC_1 and the clamped-clamped (C4-C4) boundary conditions are considered. The material properties of composite ply and epoxy are used same as given in the Tables 2.5 and 2.6 respectively. The results are presented in the Fig. 4.8, wherein R denotes the radius of the plate, h_{tk} denotes the thickness at the thick end, λ_{cr} denotes the critical buckling load, L_{tap} denotes the length of taper section and $E_{y"}$ denotes the elastic modulus of composite material in the fiber direction.

The normalized buckling load called herein as the buckling coefficient decreases with the decrease of length-to-radius ratio of the tapered curved plate. Buckling coefficient using FST based FEM solution is close to that of the FST based Ritz solution. But buckling coefficients using FEM solution and FST based Ritz solution depart away from that of CST based Ritz solution with the increase of thickness of the plate as the rotations (φ_x and φ_y) play an important role with the increase of plate thickness. The buckling load using FEM is compared with the one using CST and the error is close to 10% corresponding to the moderately-long plate ($L_{tap}/R = 0.25$). The error percentage increases with the decrease of length-to-radius ratio (L_{tap}/R) as the plate becomes shorter.

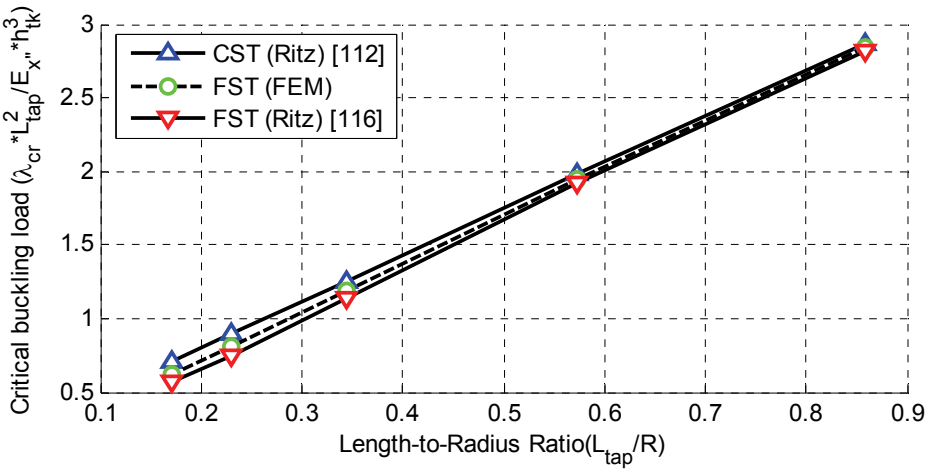

Figure 4.8: Effect of length-to-radius ratio on buckling coefficient of the clamped-clamped tapered curved laminate with the lay-up configuration LC_1 and the taper configuration B.

4.4.1.4 The effect of the stiffness ratio

The variation of critical buckling load is shown in the Figs. 4.9 and 4.10 as a function of stiffness ratio $E_{x"}/E_{y"}$ for each lay-up configuration. The results were obtained by changing the value of $E_{x"}$. In the Figs. 4.9 and 4.10, $E_{x"}$ and $E_{y"}$ denote, respectively, the elastic moduli of composite ply material in the fiber direction and in the direction transverse to the fiber direction. As was expected, the critical buckling load in all the three cases increases linearly with increasing stiffness ratio values. For the lower values of stiffness ratio, the values of the critical buckling loads of all the three lay-up configurations are very close to each other. But for higher values of stiffness ratio the critical buckling loads of the three lay-up configurations differ much between themselves. This effect is more pronounced in the case of LC_1.

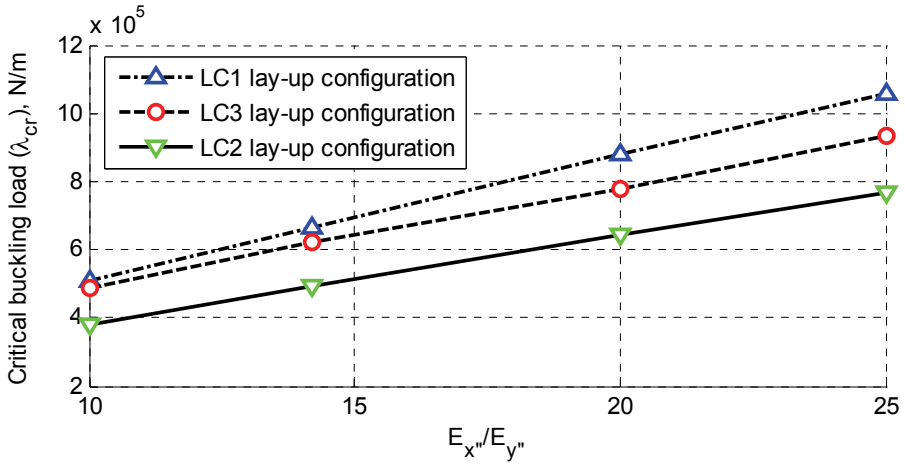

Figure 4.9: Effect of stiffness ratio on critical buckling load for clamped-clamped tapered curved laminate with the taper configuration B.

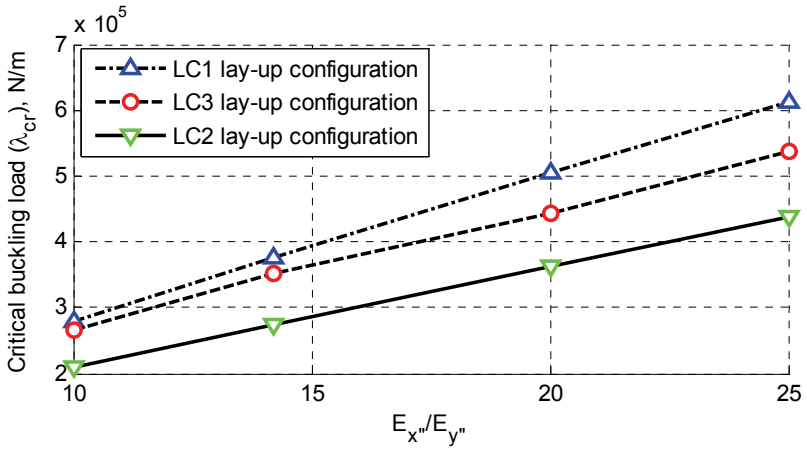

Figure 4.10: Effect of stiffness ratio on critical buckling load for simply-supported tapered curved laminate with the taper configuration B.

4.4.2 Buckling Analysis of Hybrid Curved plates

Laminates with only taper configuration have been studied in the previous sections of this chapter. The hybrid configuration (consisting of both tapered and uniform-thickness sections) is taken into account in the present sub-section. The tapered section of hybrid

plate is considered to have the taper configuration B. For the analyses of hybrid configuration three types of lay-up configurations, namely LC_1, LC_2 and LC_3 given in the Table 2.7 are considered. For the buckling analyses, the total plate length L = 229.2 mm, width b = 114.6 mm and the material properties given in Tables 2.5 and 2.6 are considered. According to the first-ply failure analysis, the hybrid plates with the above mentioned lay-up configurations will not fail by first-ply failure before global buckling. Two parameters radius-to-thickness ratio and boundary condition are investigated as to their effects on the critical buckling load of hybrid curved plate. With the increase of radius-to-thickness ratio, the plate becomes more flat as the radius is increased without changing the thickness at the thick end. The results are shown in the following Figs. 4.11 through 4.18.

4.4.2.1 Influence of Lay-Up Configurations

The normalized critical buckling loads of three lay-up configurations LC_1, LC_2 and LC_3 are calculated using finite element method and are compared in the Figs. 4.11 - 4.12. The buckling loads are calculated for clamped-clamped (C4-C4) boundary conditions. The effect of radius-to-thickness ratio on buckling load is also evaluated in the Figs. 4.11 - 4.12. In these figures, R denotes the radius, h_{tk} denotes the thickness at the thick end, λ_{cr} denotes the critical buckling load, L denotes the total length of hybrid plates and $E_{x"}$ denotes the elastic modulus of composite material in the fiber direction.

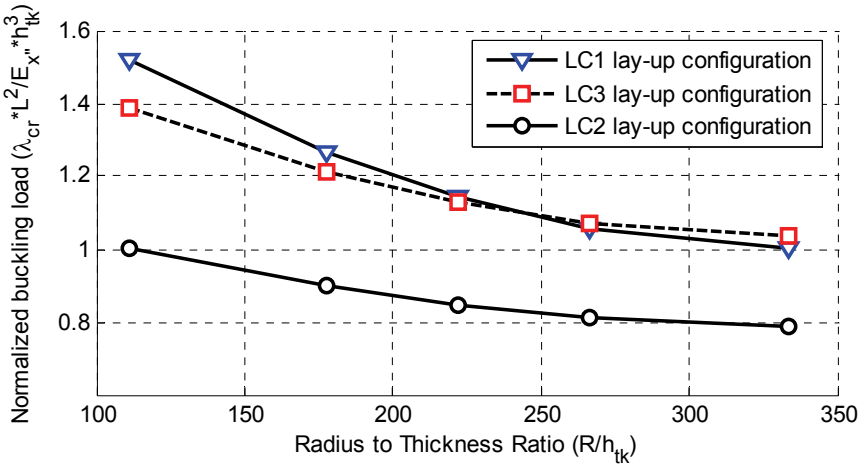

Figure 4.11: Variation of buckling coefficients with the radius-to-thickness ratio for the clamped-clamped (C4-C4) hybrid laminates with different lay-up configurations.

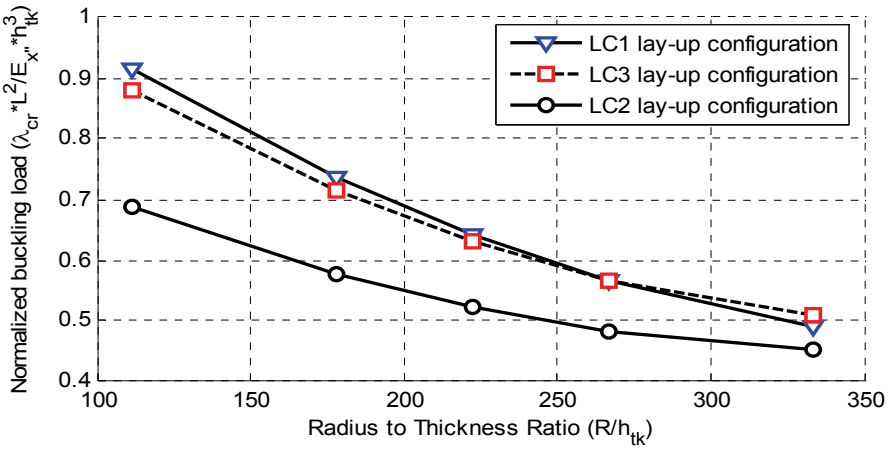

Figure 4.12: Variation of critical buckling load with the radius-to-thickness ratio for simply- supported (S4-S4) hybrid laminates with different lay-up configurations.

From Figs. 4.11 - 4.12, the following observations are made:

a) The lay-up configuration LC_2 is the weakest one among all lay-up configurations.

b) The rate of change of buckling load of lay-up configuration LC_3 is lesser than that of lay-up configuration LC_1. The buckling coefficient of LC_1 is higher than that of LC_3 for smaller values of radius-to-thickness ratio ($R/h_{tk} < 245$ for clamped-clamped plate and $R/h_{tk} < 260$ for simply-supported plate). In the case of larger values of radius-to-thickness ratio ($R/h_{tk} > 245$ for clamped-clamped plate and $R/h_{tk} > 260$ for simply-supported plate), LC_3 is stronger than LC_1.

c) In all the cases, the value of the buckling coefficient decreases nonlinearly with the increase of radius-to-thickness ratio. The values of buckling coefficient become close to each other at larger values of R/h_{tk} ratio as the plate becomes flatter. In the case of plate with larger radius, the effect of radius has less influence on the buckling coefficient and the buckling behavior of the plate largely depends on the orientation of fiber angle. For uniaxial compressive load, the fibers parallel to the direction of the applied load are the strongest ones and the fibers perpendicular to the direction of the applied load are the weakest ones. A quantitative comparison of relative stiffness of three lay-up configurations is given in the Table 3.6. Lay-up configuration LC_3 is the strongest as it is made of two types of plies: moderately stiff plies and stiffest plies. Lay-up configuration LC_2 is the weakest one as it is constructed of the moderately stiff plies only. On the other hand, lay-up configuration LC_1 is the moderately stiff as two extreme types of plies namely, the weakest plies and strongest plies, are used to construct it.

d) The buckling behavior of all the lay-up configurations is strongly influenced by R/h_{tk}.

Figs. 4.13 – 4.15 show the effect of the radius-to-thickness ratio on normalized critical buckling load. The normalized critical buckling loads corresponding to different values of radius-to-thickness ratio of hybrid curved plates are calculated using finite element method based on Koiter-Sanders shell theory. The buckling coefficients are compared with that obtained using Ritz method based on CST and using element SHELL99 of ANSYS®. From Figs. 4.13 – 4.15, the following observations are made.

a) The normalized critical buckling loads of all lay-up configurations decrease with the increase of radius-to-thickness ratio.
b) The lowest and highest values of buckling coefficients are obtained using the present FEM solution and CST based on Ritz solution respectively. In the case of classical shell theory (CST), shear strains are omitted which is the cause for the corresponding higher values of buckling loads compared to that of the other two (present FEM and ANSYS) solutions. The buckling coefficient calculated using FEM is lower than that of the ANSYS®. Because FEM solution is based on a nine-node shell element which has more degrees of freedom than that of the SHELL99 of ANSYS®.
c) On an average, the buckling coefficients of LC_1 lay-up configuration (Fig. 4.13) obtained based on ANSYS® and the present FEM solution are, respectively, 5.5% and 6.47% lower than that obtained using CST based Ritz solution.
d) On an average, the buckling coefficients of LC_2 lay-up configuration (Fig. 4.14) obtained based on ANSYS® and the present FEM solution are, respectively, 4.2% and 10.67% lower than that obtained using CST based solution.

e) On an average, the buckling coefficients of LC_3 lay-up configuration (Fig. 4.15) obtained based on ANSYS® and the present FEM solution are, respectively, 4.07% and 7.70% lower than that obtained using CST based solution.

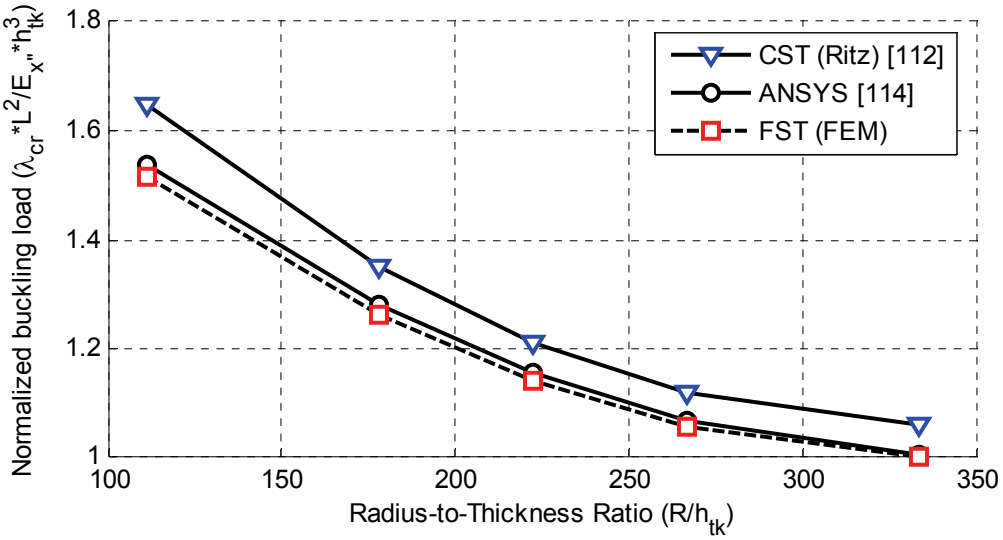

Figure 4.13: Variation of buckling coefficient with the radius-to-thickness ratio for the clamped-clamped (C4-C4) hybrid laminates with LC_1 lay-up configuration.

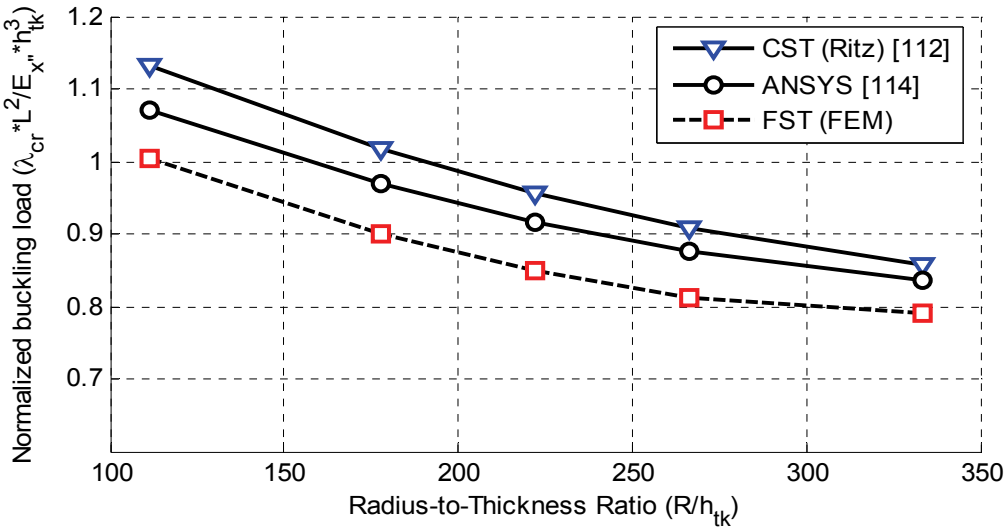

Figure 4.14: Variation of buckling coefficient with the radius-to-thickness ratio for the clamped-clamped (C4-C4) hybrid laminates with LC_2 lay-up configuration.

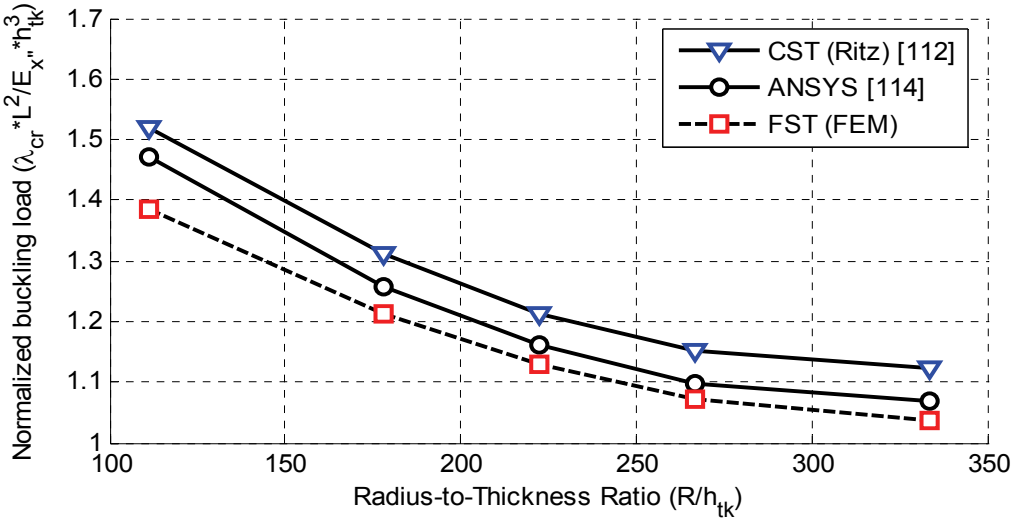

Figure 4.15: Variation of buckling coefficient with the radius-to-thickness ratio for the clamped-clamped (C4-C4) hybrid laminates with LC_3 lay-up configuration.

4.4.2.2 Influence of Boundary Conditions

Normalized critical buckling loads are calculated for the rectangular hybrid laminated curved plates (with a length/width ratio of 2.0) under uniaxial end compression. The buckling analyses are performed using finite element method based on Koiter-Sanders shell theory. Two types of boundary conditions are considered, that are, clamped at four edges (C4-C4) and simply supported at four edges (S4-S4). These boundary conditions are given in the Appendix C. The effect of radius-to-thickness ratio on the buckling coefficient for the above mentioned plates is shown in the Figs. 4.16- 4.18.

As observed from Figs. 4.16- 4.18 and as can be expected, the boundary condition has significant influence on the buckling coefficient. In terms of critical buckling load, the fully clamped plate has a higher buckling load than the simply-supported plate. Simply supported plates allow rotations at the boundaries which is the reason for less strength. For lay-up configuration LC_1 as can be seen in the Fig. 4.16, the difference between the buckling coefficient values that correspond to the clamped-clamped plate and the simply-supported plate is in the range of about 39.88% - 50.95% and the average difference is 43.50%. In the case of lay-up configuration LC_2 as can be seen in the Fig. 4.17, the difference between the buckling coefficient values that correspond to the clamped-clamped plate and the simply-supported plate is in the range of about 31.78% - 42.58% and the average difference is 37.10%. On the other hand for the lay-up configuration LC_3 as can be seen in the Fig. 4.18, the difference between the buckling coefficient values that correspond to the clamped-clamped plate and the simply-supported plate is in the range of about 36.30% - 51.56% and the average difference is 42.92%. Buckling coefficients of all the lay-up configurations are strongly influenced by both R/h_{tk} ratio and the boundary condition.

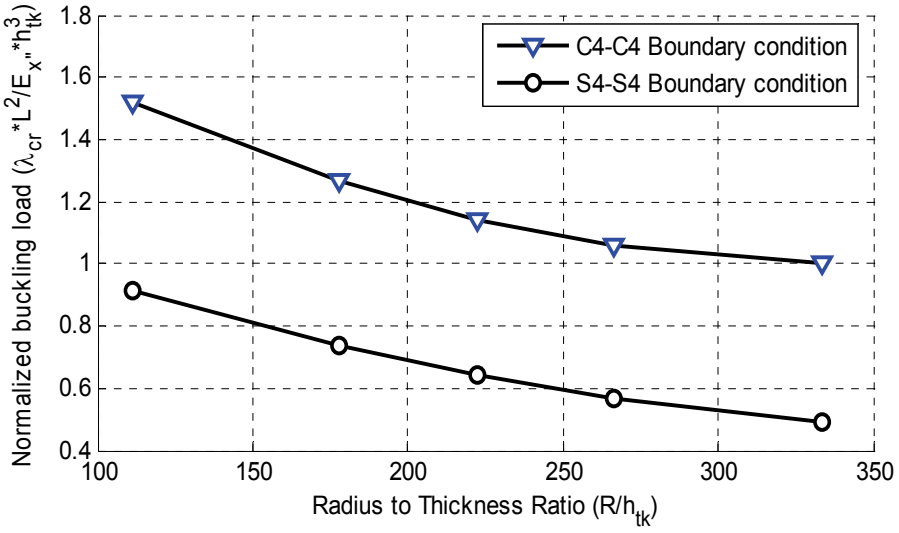

Figure 4.16: Comparison of buckling coefficient of the hybrid laminate with LC_1 lay-up configuration for different boundary conditions using FEM.

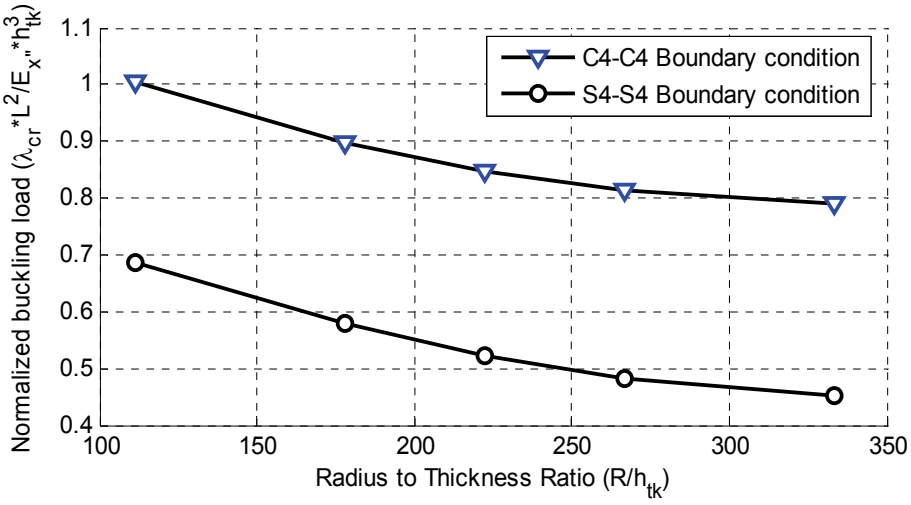

Figure 4.17: Comparison of buckling coefficient of the hybrid laminate with LC_2 lay-up configuration for different boundary conditions using FEM.

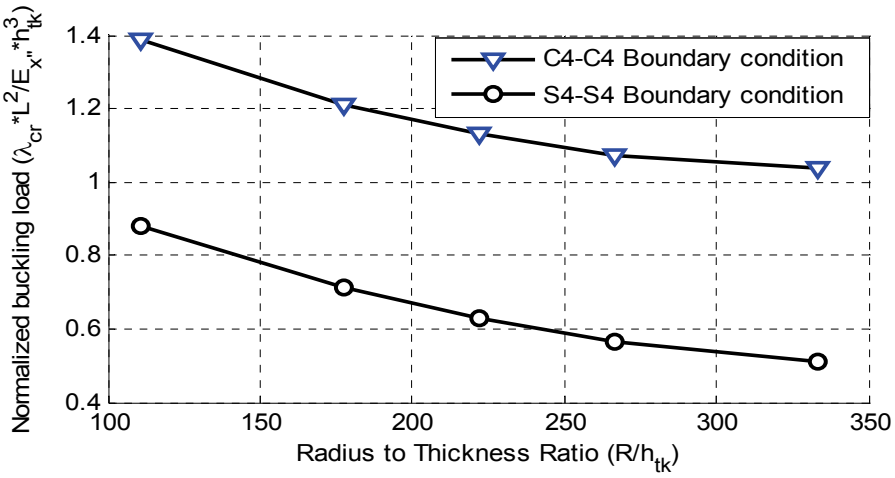

Figure 4.18: Comparison of buckling coefficient of the hybrid laminate with LC_3 lay-up configuration for different boundary conditions using FEM.

4.5 CONCLUSIONS

In the present chapter, the buckling analysis of tapered curved laminated plates has been carried out using finite element method based on six well-established first-order shallow shell theories, namely, Donnell's, Moreley's, Love's, Loo's, Koiter's and Sander's theories. Three types of tapered plates (taper configurations A and B, and a hybrid configuration), three types of lay-up configurations (LC_1, LC_2 and LC_3), and uniaxial end compressive load are considered. A detailed parametric study of the plates has been conducted that includes the influences of boundary condition, stacking sequence, taper configuration, radius, and geometric parameters of the tapered curved plates**.** The conclusions listed in the following are based on the results presented in this chapter:

a) Any of the previously mentioned shell theories can be used for the buckling analysis of uniform or tapered curved plates. But the Sander's and the Koiter's shell theories provide the most conservative result.

b) The uniaxial compressive strength can be increased significantly by making the tapered plate into a curved one and a considerable amount of material can also be saved.

c) The critical buckling loads of all lay-up configurations are considerably influenced by the stiffness ratio ($E_{x"}/E_{y"}$) of the ply material. In the present analysis, the value of $E_{x"}$ was varied without changing the value of $E_{y"}$. As a result, plate becomes stiffer in the longitudinal direction with the increase of the stiffness ratio ($E_{x"}/E_{y"}$) and this influenced significantly to increase the critical buckling load.

d) In the case of present FEM solution, classical shell theory can be used to calculate with reasonable accuracy the critical buckling loads of moderately-long plates for which $L_{tap}/R > 0.25$. The first-order shear deformation shell theory should be used for the calculation of critical buckling loads of shorter plates for which $L_{tap}/R < 0.25$. In the case of FST based Ritz solutions of chapter three, this ratio L_{tap}/R is to be 0.35. Because, the present FEM solution is closer to CST based Ritz solution compared to that of the FST based Ritz solution. For this reason, shorter plate can be used if the FEM based solution is being used in the calculation of critical buckling load.

e) At higher values of radius, lay-up configurations LC_3, LC_1 and LC_2 become the strongest, moderate and weakest laminates respectively.

Chapter 5

Non-Linear Buckling Analysis of Tapered Curved Composite Plates Based on a Simplified Methodology

5.1 INTRODUCTION

The first objective of this chapter is to conduct the fully non-linear analysis of the tapered curved plate without considering the effect of ply failure on the response of the tapered curved plate using the finite element method based on first-order shear deformation shell theories. Two non-linear shell theories are used in the analysis, that are, Donnel's and Sanders's theories. The corresponding stability limit loads are calculated and the most conservative value is obtained. The second objective is to calculate the linearized buckling loads considering the singularity of the tangent stiffness matrix. The third objective is to determine the stability limit load using a simplified methodology that involves only two load steps. A parametric study that encompasses the effects of taper angle, length-to-height ratio, radius, radius-to-thickness ratio, and geometric parameters of the plates is also conducted.

In the present work, the buckling response of curved composite plates with longitudinal internal ply-drop-off configurations as shown in Fig. 5.1 is investigated. Longitudinal-ply-drop-off tapers are those in which the internal discontinuities of the laminate are parallel to the direction of the applied load. In the Fig. 5.1, h_{tk} and h_{tn} denote the thicknesses at the thick end and thin end respectively; L_{tk}, L_{tap} and L_{tn} denote the lengths

of thick, taper and thin section respectively; R, b and b' denote the radius, the width and the cord length of curved plates respectively; and (u_o, v_o, w_o) denotes the mid-plane displacement field with reference to the global coordinate system (x, y, z). The taper configuration has five resin pockets: four small resin pockets are distributed symmetrically with respect to the mid-plane and the fifth one is designed combining the two small resin pockets. Every small resin pocket is formed by dropping-off three composite plies and there are continuous composite plies above and below each resin pocket. The hybrid configuration is obtained by combining the tapered and uniform-thickness sections as shown in the Fig. 5.1 wherein L denotes the total length.

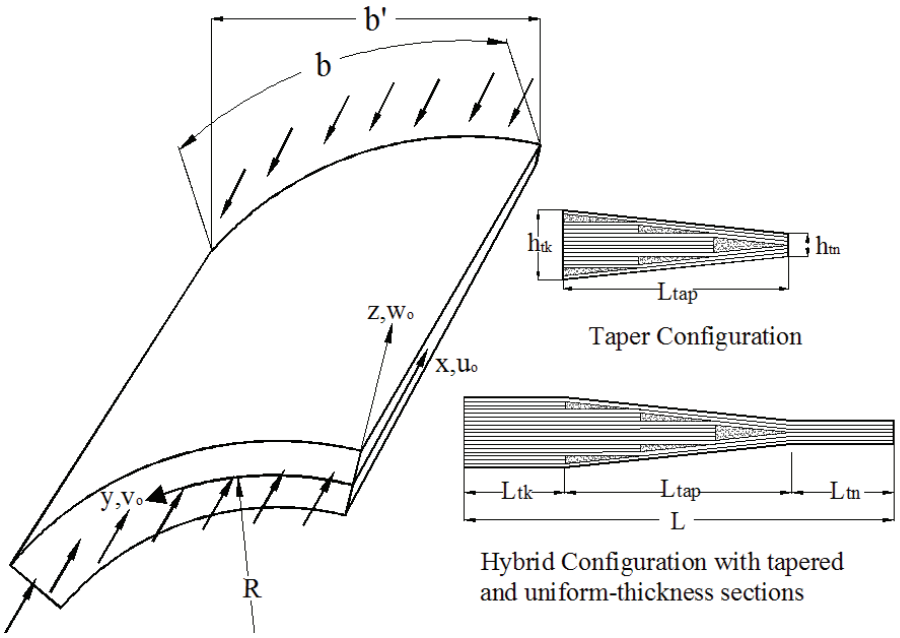

Figure 5.1: Different longitudinal cross-sections of curved plate.

5.2 FORMULATION

The basic formulation based on first order shear deformation has been described in the chapter three using the Eqs. (3.1) through (3.10). In the Eq. (3.10a), three Shear Correction (SC) factors S_1, S_2 and S_3 are given. It has been shown in the previous chapters three and four that the set (S_1=1, S_2= S_3=5/6) in the Eq. (3.11c) is the most conservative one in terms of critical buckling load. This set of shear correction factors will be used in the present non-linear analyses.

The total potential energy is expressed as the sum of strain energy U and the potential energy of external load W. For the tapered plate of dimension $L_{tap} \times b$ subjected to uni-axial compression P_x,

$$W = -P_x \int_0^b u_o \,|_{x=L_{tap}} \, dy \tag{5.1}$$

$$\begin{aligned} U &= \frac{1}{2}\int_0^b \int_0^{L_{tap}} \{[\varepsilon]^T [E'][\varepsilon]\} dxdy \\ &= \frac{1}{2}\int_0^b \int_0^{L_{tap}} \{[\varepsilon_L]^T [E'][\varepsilon_L]\} dxdy + \frac{1}{2}\int_0^b \int_0^{L_{tap}} \{[\varepsilon_L]^T [E'][\varepsilon_N]\} dxdy \\ &+ \frac{1}{2}\int_0^b \int_0^{L_{tap}} \{[\varepsilon_N]^T [E'][\varepsilon_L]\} dxdy + \frac{1}{2}\int_0^b \int_0^{L_{tap}} \{[\varepsilon_N]^T [E'][\varepsilon_N]\} dxdy \\ &= U_{LL} + U_{LN} + U_{NL} + U_{NN} \end{aligned} \tag{5.2}$$

where $\{\varepsilon\}$ and [E'] are given in the Eq. (3.10b).

The nine-node Lagrange element with five degrees of freedom per node shown in Fig. 4.1 is used in the analysis. The five degrees of freedom are: the translation displacements in x, y and z directions that are *u*, *v* and *w* respectively, and rotations about y and x axes that

are φ_x and φ_y which are due to shear deformation. The displacement fields and rotations are defined as:

$$u = \sum_{i=1}^{9} \overline{N}_i u_i ; v = \sum_{i=1}^{9} \overline{N}_i v_i ; w = \sum_{i=1}^{9} \overline{N}_i w_i ; \varphi_x = \sum_{i=1}^{9} \overline{N}_i \varphi_{x_i} ; \quad \varphi_y = \sum_{i=1}^{9} \overline{N}_i \varphi_{y_i} \tag{5.3}$$

where $\overline{N}_i(x, y)$ are the Lagrange shape functions. The shape functions are given in the Appendix C.

The linear part of the matrix of strains and curvatures, $\{\varepsilon_L\}$, is expressed as:

$$\begin{aligned} \{\varepsilon_L\} &= \left[\bar{B}_L^i\right]\{\bar{u}_e\} \\ &= \left[[\bar{B}_L^1][\bar{B}_L^2] \dots \dots \dots \dots [\bar{B}_L^9]\right] \times [u_1, v_1, w_1, \varphi_{x1}, \varphi_{y1} \dots \dots \dots u_9, v_9, w_9, \varphi_{x9}, \varphi_{y9}]^{\mathrm{T}} \end{aligned} \tag{5.4}$$

where the matrix $\left[\bar{B}_L^i\right]$ is given in the Appendix D with i = 1, 2, 3 … 9 and the non-liner part of the matrix of strains and curvatures, $\{\varepsilon_N\}$, is expressed as:

$$\{\varepsilon_N\} = 1/2[H][S]\{\bar{u}_e\} \tag{5.5}$$

The matrices [H] and [S] are given in the Appendix D. The first variation of potential energy W given by Eq. (5.1), and the first and second variations of strain energy U given by Eq. (5.2) are considered. They are expressed as:

$$\partial \mathrm{W_e} = -(\partial\{\bar{u}_e\}^t[F_e])|_{x=L_{tap}} \tag{5.6}$$

$$\partial U_e = \partial\{\bar{u}_e\}^t[K_e]\{\bar{u}_e\} \tag{5.7}$$

$$\partial^2 \mathrm{U_e} = \partial\{\bar{u}_e\}^t[K_{eT}]\partial\{\bar{u}_e\} \tag{5.8}$$

where $\{\bar{u}_e\}$ is the element nodal displacement matrix.

Further, element nodal load matrix $[F_e]$, element stiffness matrix $[K_e]$ and element tangent stiffness matrix $[K_{eT}]$ are written as:

$$[F_e] = \left([P_x N_1, 0, 0, 0, 0, P_x N_2, 0, 0, 0, 0, \ldots\ldots P_x N_9, 0, 0, 0, 0]^T \right)|_{x=L_{tap}} \tag{5.9}$$

$$\begin{aligned}[K_e] = \Bigg[& \left(\int_\Omega [\overline{B}_L]^T [E'][\overline{B}_L] d\Omega \right) + \frac{1}{2} \left(\int_\Omega [\overline{B}_L]^T [E'][H][S] d\Omega \right) \\ & + \left(\int_\Omega [S]^T [H]^T [E'][\overline{B}_L] d\Omega \right) + \left(\frac{1}{2} \int_\Omega [S]^T [H]^T [E'][H][S] d\Omega \right) \Bigg]\end{aligned} \tag{5.10}$$

$$\begin{aligned}[K_{eT}] = \Bigg[& \left(\int_\Omega [\overline{B}_L]^T [E'][\overline{B}_L] d\Omega \right) + \left(\int_\Omega [\overline{B}_L]^T [E'][H][S] d\Omega \right) \\ & + \left(\int_\Omega [S]^T [H]^T [E'][\overline{B}_L] d\Omega \right) + \left(\int_\Omega [S]^T [H]^T [E'][H][S] d\Omega \right) \\ & + \left(\int_\Omega [S]^T [N_L][S] d\Omega \right) + \left(\int_\Omega [S]^T [N_N][S] d\Omega \right) \Bigg]\end{aligned} \tag{5.11}$$

The matrices [H], [S], [N_L] and [N_N], and the matrix of shape functions [N_i] are given in the Appendix D.

The equilibrium equations for an element are expressed as:

$$\frac{\partial U}{\partial \overline{u}_e} = \frac{\partial W}{\partial \overline{u}_e} \tag{5.12}$$

The non-linear Eq. (5.12) is simplified using the Eqs. (5.6), (5.7), (5.9) and (5.10) in terms of element stiffness matrix [K_e], element nodal load matrix $\{F_e\}$ and the element nodal displacement matrix $\{\overline{u}_e\}$ as:

$$\sum \left[K_e \left(\{\overline{u}_e\} \right) \right] \{u\} = \sum \{F_e\} \tag{5.13}$$

The Newton-Raphson solution procedure for the r-th iteration can be expressed as:

$$[K_T(\{u\})]^{r-1} \{\partial u\}^r = \{F\} - [K(\{u\})]^{r-1} \{u\}^{r-1} \tag{5.14}$$

where [K_T] denotes the tangent stiffness matrix of the structure, {F} denotes the load matrix of the structure, [K] denotes the stiffness matrix of the structure, and {u} denotes the displacement matrix of the structure. The solution at the r-th iteration is then given by

$$\{u\}^r = \{u\}^{r-1} + \{\partial u\}^r \tag{5.15}$$

The linearized buckling loads are determined considering the singularity of the tangent stiffness matrix. The details of linearized buckling analysis has been explained in the Ref. [91] which is summarized in the following.

The stiffness matrices that correspond to two successive load steps represented by (t-Δt) and t are $[^{t-\Delta t}K]$ and $[^{t}K]$ respectively, and the corresponding vectors of externally applied loads are $\{^{t-\Delta t}P_x\}$ and $\{^{t}P_x\}$. In the linearized buckling analysis it is assumed that the stiffness varies linearly with the linear variation of the applied load and at any load step τ,

$$\frac{[^{\tau}K]-[^{t-\Delta t}K]}{[^{t}K]-[^{t-\Delta t}K]} = \gamma \tag{5.16}$$

and

$$\frac{\{^{\tau}P_x\}-\{^{t-\Delta t}P_x\}}{\{^{t}P_x\}-\{^{t-\Delta t}P_x\}} = \gamma \tag{5.17}$$

where γ is a scaling factor. At the state of buckling, the tangent stiffness matrix is singular and the condition for calculating γ is:

$$\det[^{\tau}K] = 0 \tag{5.18}$$

or, equivalently,

$$[^{\tau}K]\{u\} = 0 \tag{5.19}$$

Substituting from the Eq. (5.16) into the Eq. (5.19) , the eigenproblem is obtained as:

$$[^{t}K]\{u\} = \Lambda[^{t-\Delta t}K]\{u\} \tag{5.20}$$

and

$$\Lambda = \frac{\gamma - 1}{\gamma} \tag{5.21}$$

The eigenvalues Λ_i in the Eq. (5.21) are all positive and the smallest values Λ_1, Λ_2..... are of interest. The linearized buckling load is given by:

$$\{P_x\}_{Buckling} = \{^{t-\Delta t}P_x\} + \Lambda_1(\{^{t}P_x\} - \{^{t-\Delta t}P_x\}) \tag{5.22}$$

In the present work, the arc-length method of Ref. [77] is considered for the fully non-linear buckling analysis. In the case of arc-length method, both the displacement and load are iterative according to Crisfield's arc-length method [77] and the incremental displacement $\{\partial u\}^r$ is expressed in terms of displacement and load. Moreover, in the present work, post-buckling analysis is carried out without considering the effect of ply failure and the stability limit load (non-linear buckling load) is evaluated from the load-deflection curve. Numerical integration is considered to evaluate the stiffness matrix and the tangent stiffness matrix using the appropriate Gauss quadrature.

5.3 VALIDATION

To the author's knowledge, no results are available yet in the literature on the non-linear buckling analysis of the tapered curved composite plates under the action of uni-axial compression. Therefore the comparison with the existing works could not be made. In order to validate the formulation and analysis, first, the taper angle is set to be zero, and the resulting uniform-thickness plates have been analyzed and the results have been compared with that available in the literature for the uniform-thickness plates. For this purpose, the deflection of a shallow curved plate hinged on straight edges and free on the curved edges [62] is calculated using the Sanders's shell theory. The geometric and material parameters used are: width b = 2×R×α (α = 0.1 rad.), radius R = 0.0254 m (1in.), length L = 0.508 m (20 in.), thickness h = 3.175×10^{-03} m (0.125 in.), elastic modulus E =

3.10 GPa (0.45×10^6 psi) and Poisson ratio $\upsilon = 0.3$. Point load at the center of the plate is used with a load step of P = - 444.82 N and a total of 12 load steps are considered. For this non-linear analysis, full integration of stiffness coefficients and symmetric boundary conditions are considered. The deflection versus load curve is compared in the Fig. 5.2 for different mesh sizes (in the Fig. 5.2, for example, N9-6x6 represents the 6x6 mesh using nine-node element). As can be observed the results obtained using nine-node element are in close agreement with those given by Reddy [62].

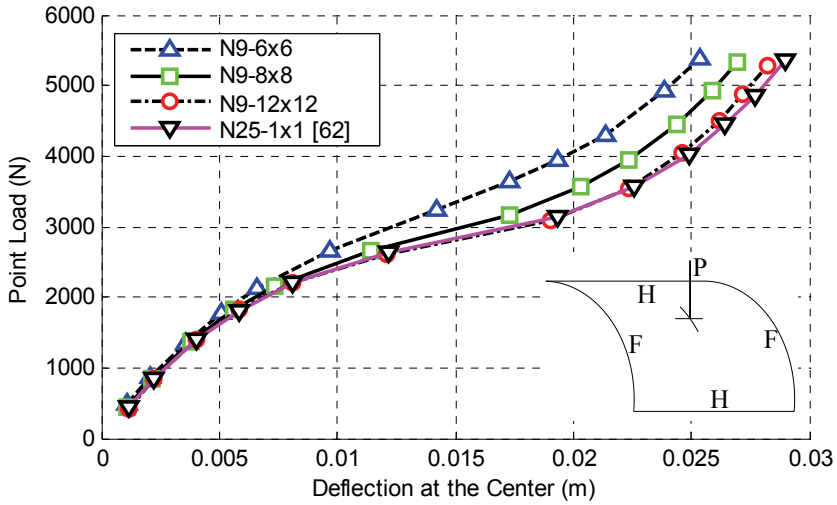

Figure 5.2: Deflection versus load curve for the hinged-free curved plate based on Sanders's shell theory.

A uniform-thickness cylindrical panel with ply configuration $[0_2/90_2]_s$ and made of T300/5208 graphite/epoxy material having the mechanical properties of $E_{x''} = 181$ GPa, $E_{y''} = E_{z''} = 10.3$ GPa, $G_{x''y''} = G_{x''z''} = G_{y''z''} = 7.10$ GPa, $\upsilon_{x''y''} = \upsilon_{x''z''} = \upsilon_{y''z''} = 0.28$ and the geometrical properties of length L = 150 mm, width b = 157.05 mm, radius R = 150 mm, thickness h = 1 mm and cross sectional area at the curved end A = 157.05 mm^2 has been

investigated by Kweon and Hong [118]. In this reference, continuum non-linear analysis has been carried out using 8-node degenerative shell element and updated Lagrangian formulation without considering the effect of ply failure. However, in the present study, fully non-linear analysis is carried out using nine-node Lagrange shell element and Sanders shell theory without considering the failure effect. The arc-length method is used to solve the non-linear equations. The load-deflection curve is plotted in the Fig. 5.3 from which the stability limit load is calculated as 129 MPa (the details of limit load calculation are given in the Appendix E) but in the Ref. [118] its value is given as 123.10 MPa. Deflections calculated based on two shell theories are close to each other but Sanders's theory provides a more conservative result. This shell theory will be used further onwards in the present work.

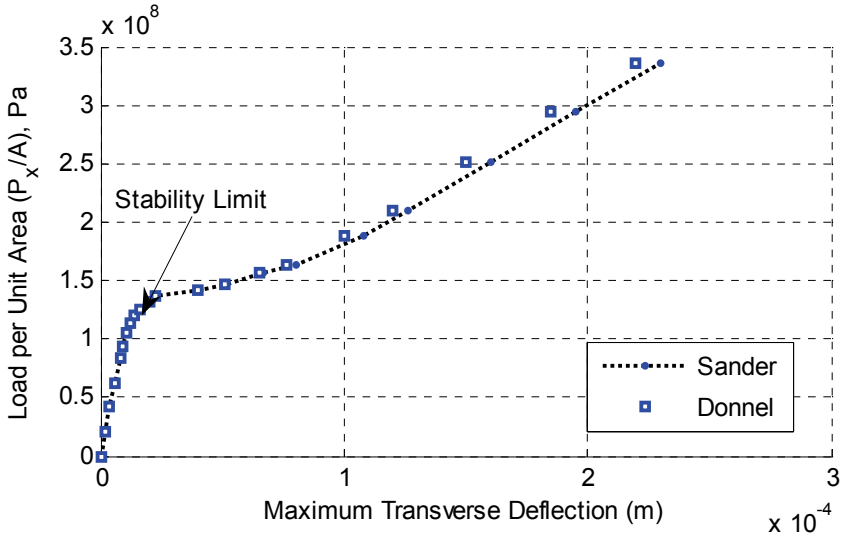

Figure 5.3: Load-deflection curve for uniform-thickness curved plate with ply configuration $[0_2/90_2]_s$.

Alternatively, the stability limit load of cylindrical panel with ply configuration $[0_2/90_2]_s$ is predicted from the linearized critical loads. The calculation of linealized critical load is performed based on a pre-stressed structure under a certain load vector $\{F_{base}\}$ and can be expressed as:

$$\{F_{base}\} = \lambda_{base}\{F_{ref}\} \tag{5.23}$$

where $\{F_{ref}\}$ denotes the reference pre-stress load vector and λ_{base} denotes the scalar base load.

To perform this type of linearized analysis, the selected load $\{F_{base}\}$ is first applied in a single load step and the modified Newton-Raphson equilibrium iteration is performed. The tangent stiffness matrix of the structure $[K_T]$ corresponding to the equilibrium state is obtained. At the succeeding step a trial load increment is applied and the stiffness matrix [K] due to stress and displacement increment of this trial load step is calculated. A basic assumption of the linearized analysis is that the structure behaves linearly before the critical load is reached. Based on this assumption, the pre-stressed load $\{F_{base}\}$ is applied to find out the corresponding critical load, so that the tangent stiffness matrix $[K_T]$ is completely degraded. To find out this additional load level, a generalized eigen-analysis procedure is applied. If the eigenvalue extraction based on this fundamental load level gives a critical scalar load $\Delta\lambda_{cr}$, then the predicted and linearized critical scalar load λ_{cr}, shown in the Fig. 5.4, is given by

$$\lambda_{cr} = \Delta\lambda_{cr} + \lambda_{base} \tag{5.24}$$

At various base load levels, different linearized critical loads may be predicted, and if the stability limit does exist for the structure, the curve formed by connecting these predicted critical loads should intersect the non-linear load-deflection curve at the point of

instability. The curve is called as the 'predicted-linearized-load curve' for easy reference (Fig. 5.4). The shape of the curve can be made unique (Ref. [89]) if the linearized critical load is plotted against the scalar base load upon which the eigenvalue extractions are performed, denoted as λ_{base} , as shown in Fig. 5.4 wherein the load per unit area are considered. In this figure, λ_{cr} denotes the critical linearized buckling load and A denotes the area at the curved end. A 45-degree base load line is plotted by considering the base load values along the y-axis correspondng to that of the x-axis. The predicted-linearized-load curve will intersect with this 45-degree line at the point of instability and this intersection point is the stability limit load of the cylindrical panel with ply configuration $[0_2/90_2]_s$.

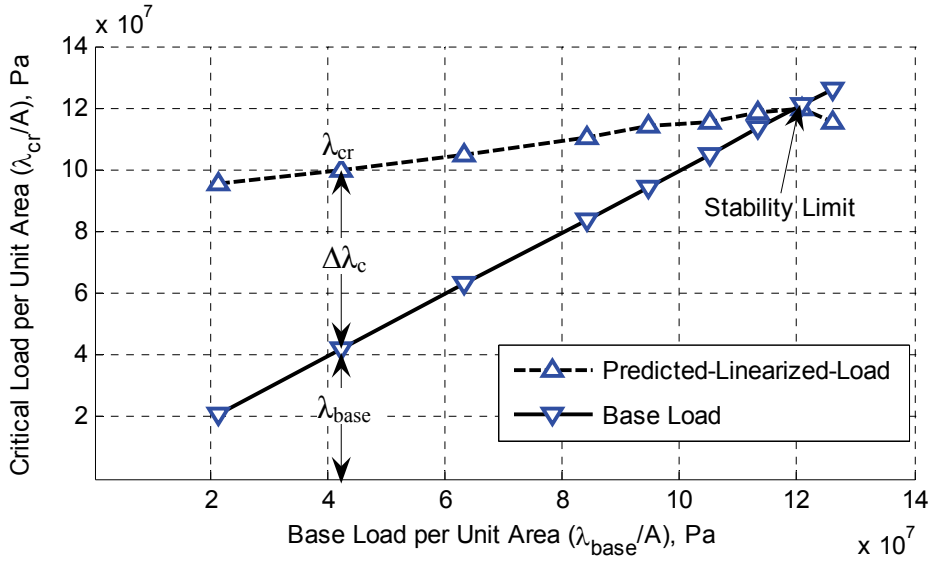

Figure 5.4: Predicted-linearized-load curve in base load system.

It is proposed in the present work that the stability limit load can also be calculated by linear interpolation considering only two load steps. It is assumed that the slope of the predicted-linearized-load curve is constant until the stability limit load. First, a linearized

buckling analysis based on the pre-stress load (b_1) is performed, and an approximated critical load (p_1) is obtained (see Fig. 5.5). Then a suitable second base load (b_2) is applied to the structure and iterations are carried out until equilibrium. This configuration of the structure is taken as the base state upon which another linearized buckling analysis is performed to obtain a new predicted critical load (p_2). Finally, on a λ_{cr}-λ_{base} graph, extrapolation from points (b_1, p_1) and (b_2, p_2) is made to find out the intersection point. The linear interpolation is expressed for the prediction of the stability limit load as:

$$Stability\ \ Limit\ \ Load = \frac{p_1 - m_2 b_1}{1 - m_2}; \tag{5.25}$$

$$m_2 = \frac{p_2 - p_1}{b_2 - b_1} \tag{5.26}$$

where m_2 is the slope of the predicted-linearized-load curve, b_1 and b_2 are the base loads, and p_1 and p_2 are the linearized critical loads corresponding to the base loads b_1 and b_2 respectively.

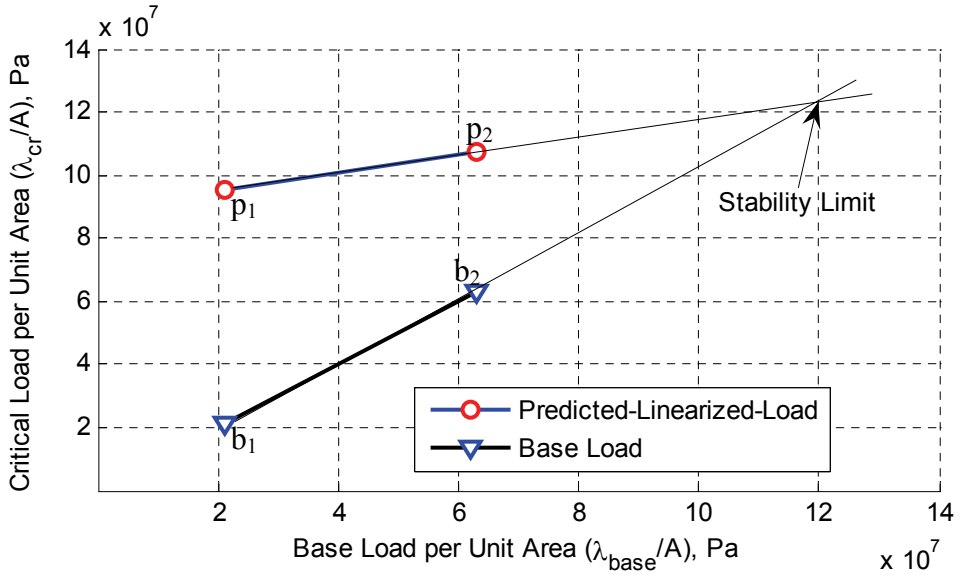

Figure 5.5: Prediction of stability limit load using the simplified methodology for uniform-thickness curved plate with ply configuration $[0_2/90_2]_s$.

In the Table 5.1, the stability limit load per unit area predicted based on the present simplified methodology is compared with that obtained using fully non-linear analysis. It is observed from the Table 5.1, the stability limit load per unit area predicted based on the simplified methodology is 6.76 % lower than that obtained from fully non-linear analysis (for corresponding load-deflection curve, see Fig. 5.3).

Table 5.1: Comparison of stability limit load per unit area for the cylindrical panel with ply configuration $[0_2/90_2]_s$

Plate Type	Stability Limit Load per Unit Area Based on Simplified Methodology (MPa)	Stability Limit Load per Unit Area Based on Fully Non-Linear Analysis (MPa)
Uniform Curved	120.27	129

5.4 PARAMETRIC STUDY

In the parametric study two types of longitudinal cross-sections of the curved plates are considered, that are, taper configuration and hybrid configuration as shown in the Fig. 5.1. The non-linear buckling analysis is carried out using nine-node Lagrange shell element based on Sander's theory. The material properties of composite material and epoxy used are the same as given in the Tables 2.5 and 2.6 respectively. Based on the convergence test, the number of elements used in the finite element analysis of taper configuration and hybrid configuration are 9×9 and 15×15 respectively. The 9×9 finite element mesh is shown in the Fig. 4.4.

5.4.1 Non-Linear Buckling Analyses of Tapered Curved Plates

For the analysis of tapered curved plates, three types of non-linear buckling analyses are considered, that are, fully non-linear buckling, linearized buckling and simplified non-linear buckling analysis. The fully non-linear buckling analysis employs a non-linear static analysis with gradually increasing load to seek the load level at which the structure becomes unstable and this load level is known as the stability limit load. The basic assumption of the linearized buckling analysis is that the structure behaves linearly before the critical load is reached. In case of simplified non-linear buckling analysis, the stability limit is calculated by linear interpolation considering only two load steps and it is assumed that the slope of the predicted-linearized-load curve is constant until the stability limit point.

Taper configuration shown in the Fig. 5.1 is considered with 36 and 12 plies at thick and thin ends respectively, which results in 24 drop-off plies. The configuration at the thick end is $[0/90]_{9s}$, and that of the thin end is $[0/90]_{3s}$. In the fully non-linear analysis of taper configuration, the height of the thick end h_{tk} is to be taken as 4.5 mm and the radius of curved plate R is set to be 500 mm. Various values for parameters, namely the critical length-to-height ratio, radius, and taper angle are investigated to see the influences of these parameters on the buckling loads of tapered curved plates. The results are shown in the following Figs. 5.6 through 5.8.

The fully non-linear analysis of clamped-clamped tapered curved square plate with the side length of 0.8594 m is carried out using the Crisfield's arc-length method [77]. The

load-deflection curve is determined and is shown in the Fig. 5.6. The stability limit load is calculated at the point where the transverse deflection increased significantly with the small increment of compressive load and this value is to be equal to 9.5×10^4 N/m which is marked in the figure.

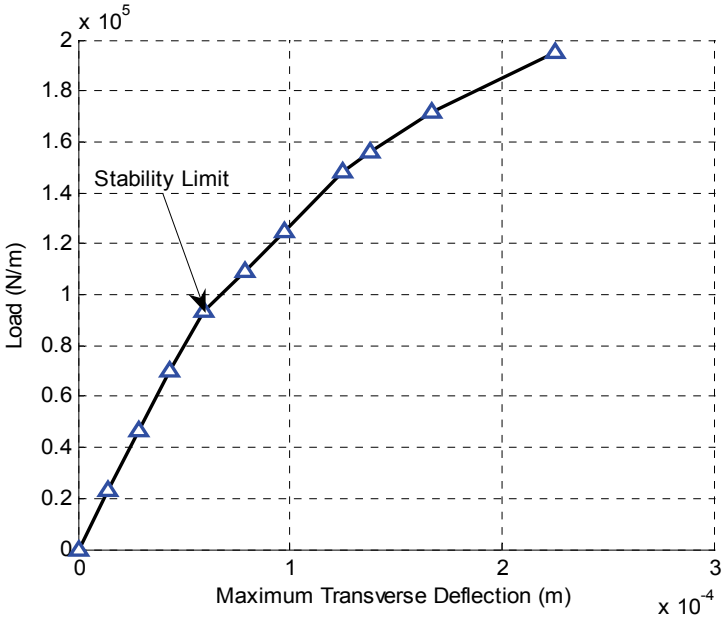

Figure 5.6: Load-deflection curve for clamped-clamped tapered curved plate

Alternatively, the stability limit load is calculated using linear interpolation considering the present simplified methodology. A linearized critical analysis based on the pre-stress load (b_1) is performed, and an approximated critical load (p_1) is obtained (see Fig. 5.7). Then a suitable second base load (b_2) is applied to the structure and another linearized critical analysis is performed to obtain a new predicted critical load (p_2). Finally, extrapolation from points (b_1, p_1) and (b_2, p_2) is made to find its intersection. The intersection point corresponds to the stability limit load of the tapered curved plate.

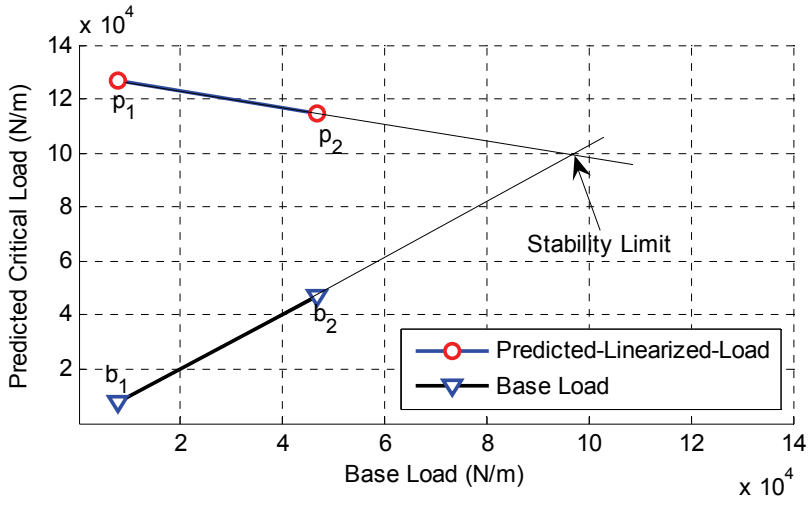

Figure 5.7: Prediction of the stability limit load of tapered curved plate using the simplified methodology.

The values of the base loads b_1 and b_2, and the corresponding linearized critical loads p_1 and p_2 are given in the Table 5.2. In this table, the stability limit loads predicted based on the present simplified methodology and using the Eq. (5.25) are compared with that obtained using the fully non-linear analysis. It is observed from the Table 5.2 that the stability limit load predicted based on the simplified methodology is 6.63 % lower than that obtained from the fully non-linear analysis (for load-deflection curve, see Fig. 5.6).

Table 5.2: Comparison of stability limit load for tapered curved plate

Plate Type	Prediction of Stability Limit Load (N/m)					Stability Limit Load Based on Fully Non-Linear Analysis (N/m)
	First load step		Second load step		Stability Limit Load (N/m)	
	Base Load b_1	Critical Load p_1	Base Load b_2	Critical Load p_2		
Tapered Curved	0.78×10^4	12.66×10^4	4.68×10^4	11.43×10^4	8.87×10^4	9.50×10^4

5.4.1.1 Influence of Taper Angle

The load carrying capability of the tapered curved plates is studied in the Ref. [116] considering first-ply failure load. This type of failure analysis is considered to determine whether a layer in the laminate has failed due to compressive loading before global buckling occurs. Element SHELL99 is used for the analyses using ANSYS®. First-ply failure analysis is carried out in the Ref. [116] using ANSYS® based on the 3-D version of Tsai-Wu failure criterion. Material properties of composite material and epoxy are given in the Tables 2.5 and 2.6 respectively.

Four different sizes of square tapered composite plates with the taper configuration of Fig. 5.1 and made of NCT/301 graphite-epoxy composite material are considered. The lay-up is $[0/90]_{9s}$ at the thick end and $[0/90]_{3s}$ at the thin end. The side length of the square plate varies from 85.9 mm to 859.4 mm, plate thickness at the thick end (h_{tk}) is 4.5 mm and radius (R) of the plate is 500 mm. The clamped-clamped (C4-C4) boundary conditions given in the Appendix D are considered. The side length of square plates corresponding to various values of taper angles are given in the Table 5.3. The first-ply failure loads are compared with the linear buckling and stability limit loads based on the present simplified methodology. From this table, the following observations are made:

a) The tapered curved plates corresponding to the taper angles of 0.75 and 1.0 degrees will fail by first-ply failure before the linear global buckling (see Table 3.3). In the case of stability limit load, tapered plate corresponding to the taper angle of 1.0 degree will fail by first-ply failure.

b) On the other hand, the plates corresponding to the taper angles of 0.1 and 0.50 degrees will not fail by first-ply failure if the linear buckling load is considered. The plates corresponding to the taper angles of 0.1, 0.50 and 0.75 degrees will not fail by first-ply failure if the stability limit load is considered. The maximum plate size should be corresponding to the taper angle of 0.53 and 0.79 degrees for linear buckling loads and stability limit loads respectively.

c) The critical length-to-height ratio (L_{tap} / h_{tk}) is to be 36 (see Fig. 3.2) and 24 (see Fig. 5.8) for the linear buckling load and stability limit load respectively.

d) In terms of numerical values, the difference between the two loads (linear buckling load and stability limit load) decreases with decrease of plate size. This is so because the plate becomes stiffer with the decrease of plate size and the stability limit load of stiff plate is closer to the bifurcation-buckling load (linear buckling load).

e) The failed layers with numbers 2 and 3, respectively, are the second layer and the third layer from the bottom at the thick end of the plates. All the tapered curved plates failed at the thick end where the number of plies above or below the resin pockets are at minimum.

Table 5.3: Comparison of linear buckling load, stability limit load and first-ply failure load of tapered curved composite plates

Taper Angle in Degree	Side Length of the Square Plate (m)	Linear Buckling Load [116] (N/m)	Stability Limit Load Based on the Simplified Methodology (N/m)	First-ply Failure Load [116] (N/m)	Failure Location (FEN, FLN)*
0.10	0.8594	14.08×10^4	8.87×10^4	48.05×10^4	1, 2
0.50	0.1719	40.05×10^4	25.68×10^4	42.00×10^4	1, 2
0.75	0.1146	59.37×10^4	42.55×10^4	43.50×10^4	9, 3
1.00	0.0859	79.48×10^4	59.61×10^4	45.60×10^4	9, 3

* FEN and FLN denote the failed element number and failed layer number at first-ply failure.

Next, the tapered plates of the Table 5.3 are analyzed corresponding to different radii using the same boundary condition (C4-C4), laminate configuration, and the material properties of Tables 2.5 and 2.6. The critical sizes of the tapered curved plates are determined corresponding to various radii. For the calculation of critical length-to-height ratio, the same procedure is applied as that used in the previous case of the plate with the radius of 500 mm. In the Fig. 5.8, the plot of radius versus critical length-to-height ratio of tapered curved plates is given. In this figure, L_{tap} denotes the taper length and h_{tk} denotes the thickness of the plate at the thick end. From Fig. 5.8, the following observations are made:

a) The critical length-to-height ratio of the plate increases with the decrease of radius. This is so because the stiffness of the tapered curved plate increases with the decrease of radius. The critical length-to-height ratio varies non-linearly with the radius. In the case of larger radius, shorter plate can be used under uni-axial compression, which will not fail before global buckling.

b) The design limit for the tapered curved composite plates mentioned in the Table 5.3 corresponds to the shaded area of the Fig. 5.8. Beyond this limit, tapered curved plate will not fail by ply failure before global buckling of the plate occurs. Dark shaded area represents the design limit predicted by the present simplified non-linear buckling (stability limit) analysis, and the dark and light shaded areas together represent the design limit corresponding to the linear buckling analysis.

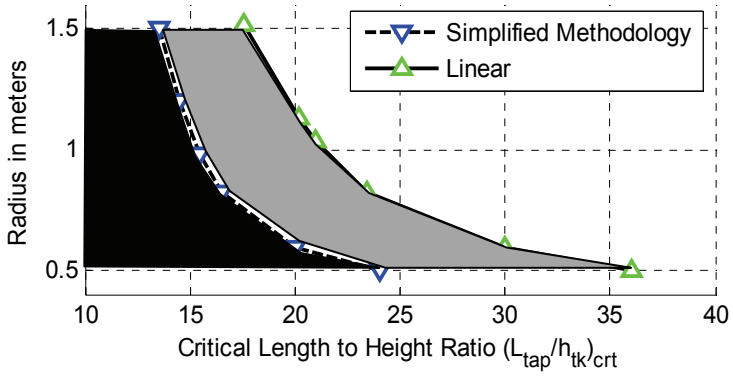

Figure 5.8: The effect of the radius of the tapered curved composite plate on the critical length-to-height ratio.

5.4.2 Non-Linear Buckling Analyses of Hybrid Curved Plates

Laminates with only taper configuration have been studied in the previous section of this chapter and the laminates with the hybrid (combined tapered and uniform-thickness) configuration are taken into account in the present sub-section. The tapered part of hybrid plates is modeled using the taper configuration shown in the Fig. 5.1. The lay-up configurations are given in the Table 2.7. For the buckling analyses, total plate length L = 229.2 mm, width b = 114.6 mm and the material properties of Tables 2.5 and 2.6 are considered. According to the first-ply failure analysis, the hybrid plates with lay-up configurations given in Table 2.7 will not fail by ply failure before global buckling. The results of the non-linear buckling analysis are shown in the following Figs. 5.9 through 5.13.

The fully non-linear analysis of clamped-clamped hybrid curved plate with lay-up configuration LC_1 and radius of 500 mm is carried out using the Crisfield's arc-length method [77]. The load-deflection curve is determined and plotted in the Fig. 5.9 from

which the stability limit load is calculated at the point where the transverse deflection increased significantly with the small increment of compressive load and this value is to be equal to 19.0×10^4 N/m.

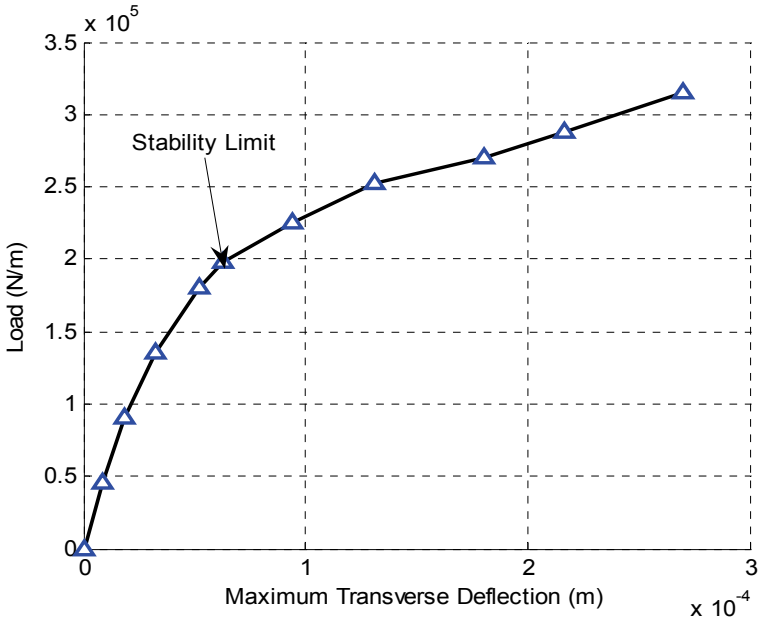

Figure 5.9: Load-deflection curve for clamped hybrid curved plate

Alternatively, the stability limit load is calculated by linear interpolation using the present simplified methodology. A linearized buckling analysis based on the pre-stress load (b_1) is performed, and an approximated critical load (p_1) is obtained (see Fig. 5.10). Then a suitable second base load (b_2) is applied to the structure and another linearized buckling analysis is performed to obtain a new predicted critical load (p_2). Finally, extrapolation from points (b_1, p_1) and (b_2, p_2) is made to find its intersection. The intersection point corresponds to the stability limit load of the tapered curved plate.

The values of the base loads b_1 and b_2, and the corresponding linearized critical loads p_1 and p_2 are given in the Table 5.4. In this table, the stability limit load predicted using the

present simplified methodology is compared with that obtained using fully non-linear analysis. It is observed from the Table 5.4, the stability limit load predicted based on simplified methodology is 8.94 % lower than that obtained from fully non-linear analysis (for the load-deflection curve, see Fig. 5.9).

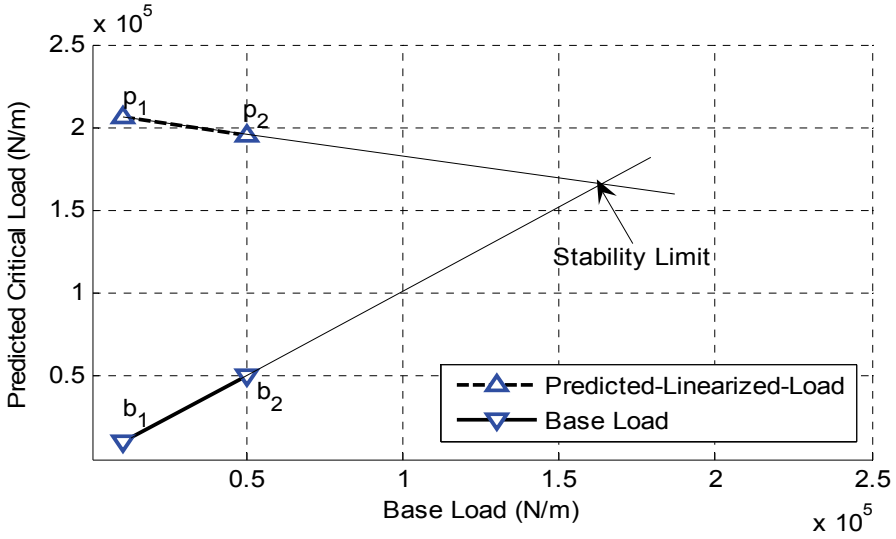

Figure 5.10: Prediction of the stability limit load of hybrid curved plate using simplified methodology.

Table 5.4: Comparison of the stability limit load for hybrid curved plate

Plate Type	Prediction of Stability Limit Load (N/m)					Stability Limit Load Based on Fully Non-Linear Analysis (N/m)
	First load step		Second load step		Stability Limit Load (N/m)	
	Base Load b_1	Critical Load p_1	Base Load b_2	Critical Load p_2		
Hybrid Curved	1.0×10^4	20.6×10^4	5.0×10^4	19.95×10^4	17.3×10^4	19.0×10^4

5.4.2.1 Influence of Radius-to-Thickness Ratio

Figs. 5.11 through 5.13 show the influence of the radius-to-thickness ratio on the normalized stability limit and the normalized linear buckling load. The normalized

stability limit loads corresponding to different radius-to-thickness ratio of hybrid curved plates are calculated using simplified methodology based on Sander's theory and these normalized loads are compared with the linear buckling loads obtained using Ritz method based on Classical Shell Theory (CST) and First-order shear deformation Shell Theory (FST). In the Figs. 5.11 – 5.13, R denotes the radius, h_{tk} denotes the thickness of the plate at thick end, λ_{cr} denotes the stability limit load or critical linear buckling load, L_{tap} denotes the length of taper section and $E_{x"}$ denotes the elastic modulus of the composite material in the fiber direction. From Figs. 5.11 – 5.13, the following observations are made:

a) All types of normalized loads decrease with the increase of radius-to-thickness ratio.
b) The lowest and highest normalized loads are obtained using the simplified methodology and CST-based Ritz solution respectively. In the case of CST-based Ritz solution, shear strains are omitted which is the cause for higher buckling loads compared to that obtained using the other two methods. The normalized load using the simplified methodology is lower than that of the FST-based Ritz solution. Because the equations for the strains of non-linear shell theory which is linearized to calculate the stability limit load have more non-linear terms compared to the linear shell theory.
c) Stability limit load of hybrid plates are strongly radius-to-thickness ratio dependent.

d) The stability limit load diverges away from the linear buckling load with the increase of radius-to-thickness ratio. This is so because the plate becomes more flexible with the increase of radius.

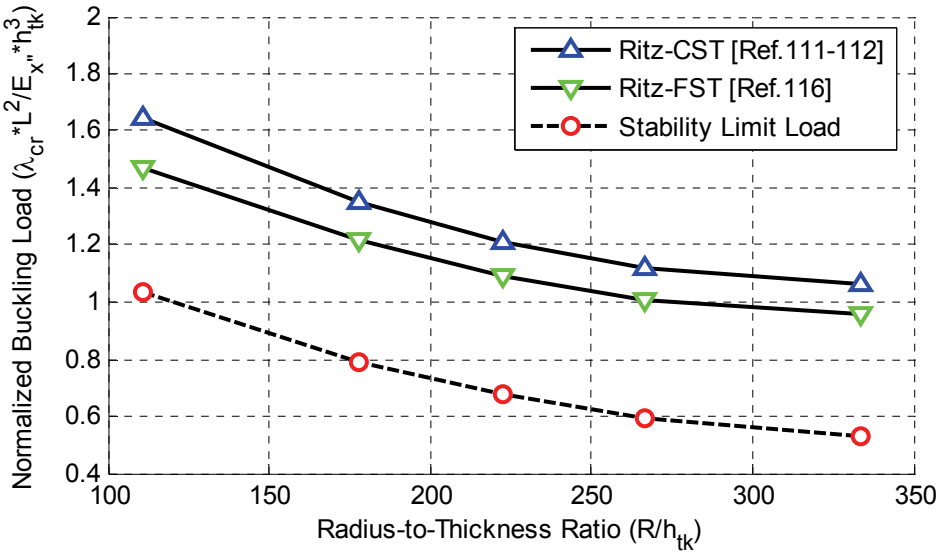

Figure 5.11: Variation of buckling loads with the radius-to-thickness ratio of the clamped-clamped hybrid plate with lay-up configuration LC_1.

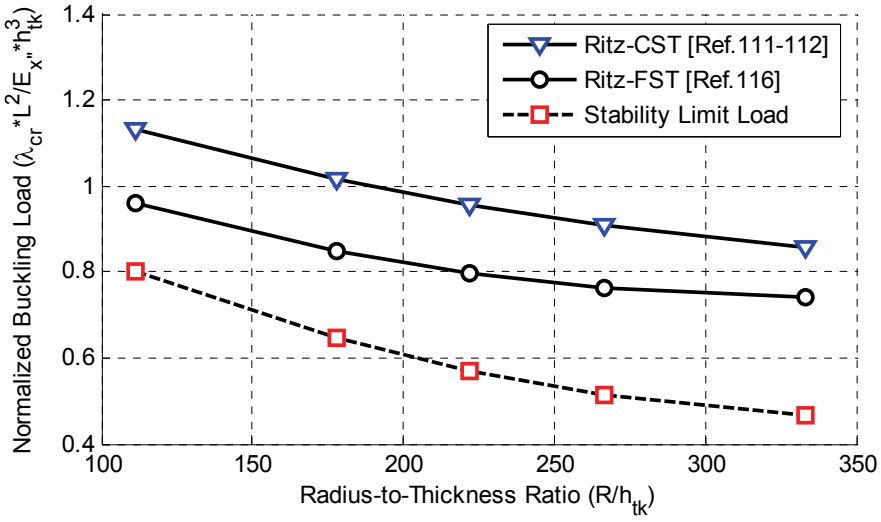

Figure 5.12: Variation of buckling loads with the radius-to-thickness ratio of the clamped-clamped hybrid plate with lay-up configuration LC_2.

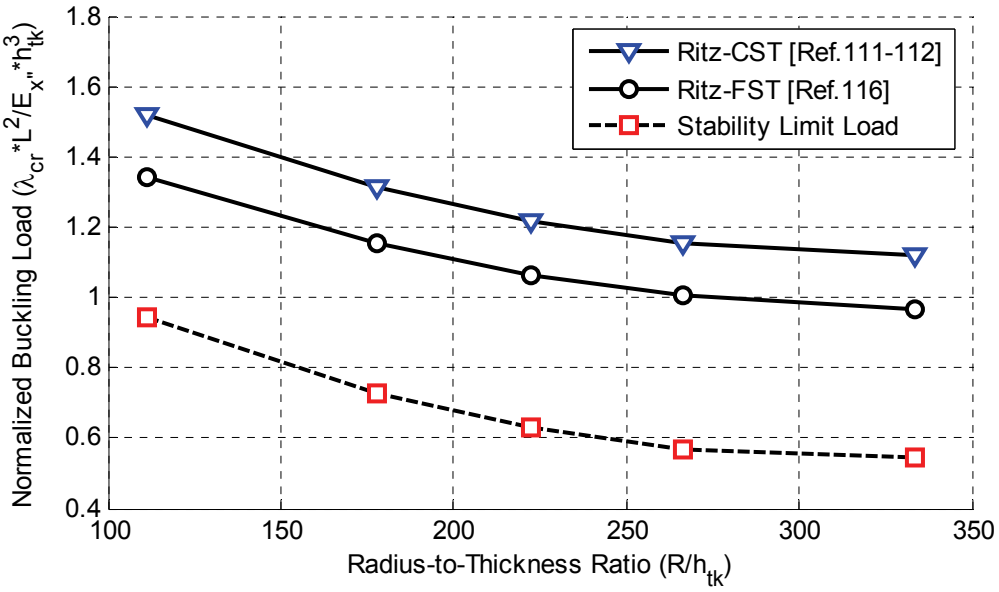

Figure 5.13: Variation of buckling loads with the radius-to-thickness ratio of the clamped-clamped hybrid plate with lay-up configuration LC_3.

5.5 CONCLUSIONS

In the present chapter, fully non-linear and linearized buckling analyses have been carried out using finite element method based on two well known first-order shallow shell theories, namely, Donnel's, and Sander's theories. Three types of composite plates, that are, uniform-thickness, tapered and hybrid plates are considered under uni-axial compressive load. A detailed parametric study of curved (tapered and hybrid) plates has been conducted that includes the influences of taper angle, critical length-to-height ratio, radius, radius-to-thickness ratio and geometric parameters of the plates on the buckling load. The conclusions listed herein, are based on all the numerical results presented.

a) Any of the above mentioned shell theories can be used for the buckling analysis of flat or tapered curved plates. However, the Sander's shell theory provides the most conservative results.

b) Stability limit load calculated based on the simplified methodology has agreement with that of the fully non-linear analysis. The present simplified methodology consumes reasonably shorter computational time compared to the standard fully non-linear analysis.

c) The moderately thick and tapered curved composite plates may fail by ply failure before global buckling. Therefore, the tapered curved plate should be larger than the corresponding critical size. The critical size depends on both the radius and taper angle of the plate.

d) Stability limit load of hybrid plate depends strongly on the radius-to-thickness ratio.

Chapter 6

Conclusions, Contributions, and Future Work

6.1 CONCLUDING REMARKS

The objective of the present thesis work is to investigate the compressive response of shallow curved composite plates with longitudinal internal ply-drop-off configurations. For this purpose, three types of analyses, namely, global buckling (linear and non-linear), first-ply failure, and delamination failure analyses are considered. Three types of tapered plates (taper configurations A and B, and a hybrid configuration) and three types of lay-up configurations (LC_1, LC_2 and LC_3) are investigated.

Linear global buckling is carried out using Classical Shell Theory (CST) based on Ritz method and using First-order shear deformation Shell Theory (FST) based on the Ritz method and Finite Element Method (FEM). The classical linear buckling analysis is carried out based on eight well-known classical shallow shell theories, namely Donnell's, Love's, Mushtari's, Timoshenko's, Vlasov's, Sander's, Koiter's and Novozhilov's theories. The linear buckling analysis is also carried out based on six well-established first-order shear deformation shell theories, that are, Donnell's, Moreley's, Love's, Loo's, Koiter's and Sander's theories. The Ritz method is used to solve both of the CST and FST based linear buckling problems. A nine-node tapered curved composite finite element is developed based on the above mentioned six first-order shear deformation shell theories. In the case of different shell theories, the corresponding critical buckling loads are calculated and the most conservative value is obtained.

Linear buckling analysis is insufficient to take into account the effect of large deflections on the buckling loads of structural components. This effect can only be considered in the non-linear buckling analysis. However, very large number of load steps is required to determine the buckling load based on the non-linear analysis in which the stability limit load is calculated from the non-linear load-deflection curve. In the present thesis work, a simplified methodology is developed to predict the stability limit load that requires the consideration of only two load steps. The stability limit loads of the tapered curved plates are calculated using this simplified methodology.

The strength characteristics and load carrying capability of the tapered curved plates are investigated considering the first-ply failure and delamination failure analyses using ANSYS®. First-ply failure analysis is carried out based on the 3-D version of Tsai-Wu failure criterion. The initiation of delamination, if any, is dictated by the transverse interlaminar stresses developed under compressive load. The interlaminar transverse shear stresses in shell element are calculated based on the assumption that no shear is carried at the top and bottom surfaces of the element. These interlaminar shear stresses are only computed in the interior of the element and are computed using equilibrium requirements.

Based on the failure and buckling analyses, the critical sizes and parameters of the tapered curved plates that will not fail before global buckling are determined. Parametric studies that encompass the effects of boundary conditions, stacking sequence, taper configurations, radius and other geometric parameters of the plates are conducted.

Based on the present study, the following main concluding remarks are made:

a) The buckling results based on different classical shell theories are close to each other but the Novozhilov's shell theory provides the most conservative result.

b) Any of the previously mentioned first-order shear deformation shell theories can be used for the buckling analysis of uniform or tapered curved plates. But the Sander's and the Koiter's shell theories provide the most conservative result.

c) The moderately-thick and tapered curved composite plates can also fail by first-ply failure before global buckling. Therefore the dimensions of tapered curved plate should be larger than the corresponding critical size. The critical sizes depend on both radius and stacking sequence of the plates. Such critical sizes have been determined in the present work.

d) The tapered flat plate is more flexible than uniform flat plate, but the tapered curved plate provides a better design option in terms of saving the material without any compromise of the strength.

e) Uniaxial compressive strength can be increased significantly by making the tapered plate into a curved one and a considerable amount of material can also be saved.

f) The critical buckling loads of all lay-up configurations are considerably influenced by the stiffness ratio ($E_{x"}/E_{y"}$) of the ply material.

g) Classical shell theory can be used to calculate with reasonable accuracy the critical buckling loads of moderately-long plates for which $L_{tap}/R > 0.35$. The first-order shear deformation shell theory should be used for the calculation of critical buckling loads of shorter plates for which $L_{tap}/R < 0.35$.

h) The normalized buckling load is more dependent on length-to-radius ratio (L_{tap}/R) than the taper configuration.

i) The buckling behavior of all the lay-up configurations are both radius-to-thickness ratio (R/h_{tk}) and boundary condition dependent. At higher values of radius, lay-up configurations LC_3, LC_1 and LC_2 become the strongest, moderate and weakest laminates respectively.

j) Stability limit load calculated based on the simplified methodology has agreement with that of the fully non-linear analysis. The present simplified methodology consumes reasonably shorter computational time compared to the standard fully non-linear analysis.

6.2 CONTRIBUTIONS

The remarkable contributions made in this thesis are summarized below:

1) One of the important contributions of the present thesis is a systematic and thorough study of the compressive response of the tapered curved composite plates. The tapered curved plate provides a better design option in terms of saving the material without any compromise of the strength. The cost of the engineering products can be minimized by reducing the weight of the products. According to Bombardier [119], the extra cost of $41,000 to 69,000 USD per year per aircraft is needed for the extra Operating Empty Weight (OWE) of 500 kg of a regional jet.

2) The second most important contribution is the present simplified methodology that consumes reasonably shorter computational time compared to the standard fully non-linear analysis.

3) The critical sizes and parameters of the tapered curved plates that will not fail by first-ply failure and delamination failure before global buckling are determined. This contribution is made for design purpose.

4) To apply the first-order shear deformation shell theories to analyze the tapered plates, an appropriate set of shear correction factors have been determined.

6.3 RECOMMENDATIONS

The following recommendations for further study can be considered:

1) A low velocity transverse impact on a composite plate may cause internal delaminations, which has not been considered in the present work. Therefore, Compression After Impact (CAI) of the tapered curved plates can be considered in the future work.

2) The post-buckling response of tapered curved composite plates including progressive failure of the laminate under compressive and shear loadings.

3) To quantify the effect of stochastic variability in the material properties on the progressive failure.

4) The dynamic buckling analysis of the tapered curved composite plates.

APPENDIX A

Boundary Conditions for Classical Shell Theory

S3:

at x=0, L	at y=0, b
u ≠ dw/dx ≠ 0; w = v = N_{xx} = M_{xx} = 0	v≠ dw/dy ≠ 0; w = u = M_{yy} = N_{yy} = 0
$W_m = \sin(m\pi \frac{x}{L})$	$W_n = \sin(n\pi \frac{y}{b})$
$V_m = \sin(m\pi \frac{x}{L})$	$V_n = \cos(n\pi \frac{y}{b})$
$U_m = \cos(m\pi \frac{x}{L})$	$U_n = \sin(n\pi \frac{y}{b})$

(*A1*)

S4:

at x=0, L	at y=0, b
dw/dx ≠ 0; w = v = u = M_{xx} = 0	dw/dy ≠ 0; w = u = v = M_{yy} = 0
$W_m = \sin(m\pi \frac{x}{L})$	$W_n = \sin(n\pi \frac{y}{b})$
$V_m = \sin(m\pi \frac{x}{L})$	$V_n = \sin(n\pi \frac{y}{b})$
$U_m = \sin(m\pi \frac{x}{L})$	$U_n = \sin(n\pi \frac{y}{b})$

(*A2*)

C3:

at x=0, L	at y=0, b
u ≠ M_{xx} ≠ 0; w = v = N_{xx} = dw/dx = 0	v ≠ M_{yy} ≠ 0; w = u = dw/dy = N_{yy} = 0
$W_m = \left(\cos\frac{\lambda_i x}{L} - \cosh\frac{\lambda_i x}{L}\right) - \gamma_i\left(\sin\frac{\lambda_i x}{L} - \sinh\frac{\lambda_i x}{L}\right)$	$W_n = \left(\cos\frac{\lambda_i y}{b} - \cosh\frac{\lambda_i y}{b}\right) - \gamma_i\left(\sin\frac{\lambda_i y}{b} - \sinh\frac{\lambda_i y}{b}\right)$
Vm =Wm;	$V_n = \cos(n\pi \frac{y}{b})$
$U_m = \cos(m\pi \frac{x}{L})$	Un=Wn

(*A3*)

C4:

at x=0, L	at y=0, b
M_{xx} ≠ 0; w = v = dw/dx = 0	M_{yy} ≠ 0; w = u = v = dw/dy = 0
$W_m = \left(\cos\frac{\lambda_i x}{L} - \cosh\frac{\lambda_i x}{L}\right) - \gamma_i\left(\sin\frac{\lambda_i x}{L} - \sinh\frac{\lambda_i x}{L}\right)$	$W_n = \left(\cos\frac{\lambda_i y}{b} - \cosh\frac{\lambda_i y}{b}\right) - \gamma_i\left(\sin\frac{\lambda_i y}{b} - \sinh\frac{\lambda_i y}{b}\right)$
Vm =Wm;	$V_n = \frac{dW_n}{dy}$
$U_m = \frac{dW_m}{dx}$; u = 0 at x = L	Un = Wn
$U_m = \cos(m\pi \frac{x}{L})$; u ≠ 0 at x = 0	

(*A4*)

In general, the displacement functions are expressed in the Equations (2.17) through (2.19) and Um, Un, Vm, Vn, Wm and Wn are selected from the above expressions for different boundary conditions. L and b are the length and width of the plate respectively; N_{ij} and M_{ij} are the resultant force and moment respectively, where i, j = x, y. The values

of Lamda, λ_i and Gama, γ_i can be found in Bertholate [103]. Si and Ci are the simply supported and clamped boundary conditions respectively with i= 3, 4.

System Equations of Classical Shallow Shell Theories

For balanced symmetric laminate, $B_{ij}=0$ and $A_{16}=A_{26}=0$; applying these conditions to the equations (2.26), the following expressions of L_{IJ}^{st} and G_{IJ}^{st} are obtained, where s, t = 1, 2, 3:

$$L_{IJ}^{11} = \sum_{m=1}^{M}\sum_{n=1}^{N} \left\{ \sum_{i=1}^{M}\sum_{j=1}^{N} \left\{ \int_0^L A_{66} U_m U_i dx \int_0^b \frac{dU_n}{dy}\frac{dU_j}{dy} dy + \int_0^L A_{11} \frac{dU_m}{dx}\frac{dU_i}{dx} dx \int_0^b U_n U_j dy + \int_0^L D_{66} \left(\frac{c_4}{R}\right)^2 U_m U_i dx \int_0^b \frac{dU_n}{dy}\frac{dU_j}{dy} dy \right\} \right\} \tag{A5}$$

$$L_{IJ}^{12} = \sum_{m=1}^{M}\sum_{n=1}^{N} \left\{ \sum_{i=1}^{M}\sum_{j=1}^{N} \left\{ -\int_0^L D_{26} \frac{c_2}{R^2} c_4 U_m V_i dx \int_0^b \frac{dU_n}{dy}\frac{dV_j}{dy} dy - \int_0^L \frac{D_{66}}{R^2} c_3 c_4 U_m \frac{dV_i}{dx} dx \int_0^b \frac{dU_n}{dy} V_j dy + \int_0^L A_{66} U_m \frac{dV_i}{dx} dx \int_0^b \frac{dU_n}{dy} V_j dy + \int_0^L A_{12} \frac{dU_m}{dx} V_i dx \int_0^b U_n \frac{dV_j}{dy} dy \right\} \right\} \tag{A6}$$

$$L_{IJ}^{13} = \sum_{m=1}^{M}\sum_{n=1}^{N} \left\{ \sum_{i=1}^{M}\sum_{j=1}^{N} \left\{ \int_0^L \frac{D_{26}}{R} c_4 U_m W_i dx \int_0^b \frac{dU_n}{dy}\frac{d^2W_j}{dy^2} dy + 2\int_0^L \frac{D_{66}}{R} c_4 U_m \frac{dW_i}{dx} dx \int_0^b \frac{dU_n}{dy}\frac{dW_j}{dy} dy + \int_0^L D_{26} \frac{c_1}{R^3} c_4 U_m W_i dx \int_0^b \frac{dU_n}{dy} W_j dy + \int_0^L \frac{A_{12}}{R} \frac{dU_m}{dx} W_i dx \int_0^b U_n W_j dy + \int_0^L \frac{D_{16}}{R} c_4 U_m \frac{d^2W_i}{dx^2} dx \int_0^b \frac{dU_n}{dy} W_j dy \right\} \right\} \tag{A7}$$

$$L_{IJ}^{22} = \sum_{m=1}^{M}\sum_{n=1}^{N} \left\{ \sum_{i=1}^{M}\sum_{j=1}^{N} \left\{ \int_0^L A_{22} V_m V_i dx \int_0^b \frac{dV_n}{dy}\frac{dV_j}{dy} dy + \int_0^L D_{66} \left(\frac{c_3}{R}\right)^2 \frac{dV_m}{dx}\frac{dV_i}{dx} dx \int_0^b V_n V_j dy + \int_0^L A_{66} \frac{dV_m}{dx}\frac{dV_i}{dx} dx \int_0^b V_n V_j dy + \int_0^L D_{26} \frac{c_2}{R^2} c_3 \frac{dV_m}{dx} V_i dx \int_0^b V_n \frac{dV_j}{dy} dy + \int_0^L D_{22} \left(\frac{c_2}{R}\right)^2 V_m V_i dx \int_0^b \frac{dV_n}{dy}\frac{dV_j}{dy} dy + \int_0^L D_{26} \frac{c_2}{R^2} c_3 V_m \frac{dV_i}{dx} dx \int_0^b \frac{dV_n}{dy} V_j dy \right\} \right\} \tag{A8}$$

$$
\begin{aligned}
L_{IJ}^{23} = \sum_{m=1}^{M}\sum_{n=1}^{N} \Bigg\{ \sum_{i=1}^{M}\sum_{j=1}^{N} \Bigg\{ & -2\int_0^L \frac{D_{66}}{R} c_3 \frac{dV_m}{dx}\frac{dW_i}{dx}dx \int_0^b V_n \frac{dW_j}{dy}dy - \int_0^L D_{26}\frac{c_1}{R^3}c_3\frac{dV_m}{dx}W_i dx \int_0^b V_n W_j d \\
& - \int_0^L D_{16}\frac{c_3}{R}\frac{dV_m}{dx}\frac{d^2W_i}{dx^2}dx\int_0^b V_n W_j dy + \int_0^L \frac{A_{22}}{R}V_m W_i dx \int_0^b \frac{dV_n}{dy}W_j dy \\
& - \int_0^L D_{26}\frac{c_3}{R}\frac{dV_m}{dx}W_i dx\int_0^b V_n \frac{d^2W_j}{dy^2}dy - 2\int_0^L D_{26}\frac{c_2}{R}V_m\frac{dW_i}{dx}dx\int_0^b \frac{dV_n}{dy}\frac{dW_j}{dy}dy \\
& - \int_0^L D_{22}\frac{c_1}{R^3}c_2 V_m W_i dx\int_0^b \frac{dV_n}{dy}W_j dy - \int_0^L D_{22}\frac{c_2}{R}V_m W_i dx\int_0^b \frac{dV_n}{dy}\frac{d^2W_j}{dy^2}dy \\
& - \int_0^L D_{12}\frac{c_2}{R}V_m\frac{d^2W_i}{dx^2}dx\int_0^b \frac{dV_n}{dy}W_j dy \Bigg\} \Bigg\}
\end{aligned}
\tag{A9}
$$

$$
G_{IJ}^{22} = \sum_{m=1}^{M}\sum_{n=1}^{N} \left\{ \sum_{i=1}^{M}\sum_{j=1}^{N} \left\{ \int_0^L \frac{dV_m}{dx}\frac{dV_i}{dx}dx \int_0^b V_n V_j dy \right\} \right\}
\tag{A10}
$$

$$
G_{IJ}^{23} = \sum_{m=1}^{M}\sum_{n=1}^{N} \left\{ \sum_{i=1}^{M}\sum_{j=1}^{N} \left\{ \int_0^L \frac{dW_m}{dx}\frac{dW_i}{dx}dx \int_0^b W_n W_j dy \right\} \right\}
\tag{A11}
$$

$$
\begin{aligned}
L_{IJ}^{33} = \sum_{m=1}^{M}\sum_{n=1}^{N} \Bigg\{ \sum_{i=1}^{M}\sum_{j=1}^{N} \Bigg\{ & 2\int_0^L D_{26}\frac{c_1}{R^2}W_m\frac{dW_i}{dx}dx\int_0^b W_n\frac{dW_j}{dy}dy + \int_0^L D_{12}\frac{c_1}{R^2}\frac{d^2W_m}{dx^2}W_i dx\int_0^b W_n W_j dy \\
& + \left[\int_0^L D_{22}\frac{c_1}{R^2}W_m W_i dx\int_0^b \frac{d^2W_n}{dy^2}W_j dy + 2\int_0^L D_{26}W_m\frac{dW_i}{dx}dx\int_0^b \frac{d^2W_n}{dy^2}\frac{dW_j}{dy}dy \right] \\
& + 2\int_0^L D_{16}\frac{dW_m}{dx}\frac{d^2W_i}{dx^2}dx\int_0^b \frac{dW_n}{dy}W_j dy + 2\int_0^L D_{26}\frac{c_1}{R^2}\frac{dW_m}{dx}W_i dx\int_0^b \frac{dW_n}{dy}W_j dy \\
& + \left[\int_0^L D_{22}\frac{c_1}{R^2}W_m W_i dx\int_0^b W_n\frac{d^2W_i}{dy^2}dy + 2\int_0^L D_{16}\frac{d^2W_m}{dx^2}\frac{dW_i}{dx}dx\int_0^b W_n\frac{dW_j}{dy}dy \right] \\
& + \int_0^L D_{22}\frac{c_1^2}{R^4}W_m W_i dx\int_0^b W_n W_j dy + \int_0^L D_{12}\frac{d^2W_m}{dx^2}W_i dx\int_0^b W_n\frac{d^2W_j}{dy^2}dy \\
& + 2\int_0^L D_{26}\frac{dW_m}{dx}W_i dx\int_0^b \frac{dW_n}{dx}\frac{d^2W_j}{dx^2}dy + 4\int_0^L D_{66}\frac{dW_m}{dx}\frac{dW_i}{dx}dx\int_0^b \frac{dW_n}{dy}\frac{dW_j}{dy}dy \\
& + \int_0^L D_{12}\frac{c_1}{R^2}W_m\frac{d^2W_i}{dx^2}dx\int_0^b W_n W_j dy + \int_0^L D_{11}\frac{d^2W_m}{dx^2}\frac{d^2W_i}{dx^2}dx\int_0^b W_n W_j dy \\
& + \int_0^L \frac{A_{22}}{R^2}W_m W_i dx\int_0^b W_n W_j dy + \int_0^L D_{12}W_m\frac{d^2W_i}{dx^2}dx\int_0^b \frac{d^2W_n}{dy^2}W_j dy \\
& + \int_0^L D_{22}W_m W_i dx\int_0^b \frac{d^2W_n}{dy^2}\frac{d^2W_j}{dy^2}dy \Bigg\} \Bigg\}
\end{aligned}
\tag{A12}
$$

The respective values of c_1, c_2, c_3 and c_4 are given in the section of formulation.

APPENDIX B

Boundary Conditions for First-order Shear Deformation Shell Theory

S3:

at x = 0, L

$w = M_{xx} = \varphi_y = N_{xx} = v = 0$

$$W_m = \sin(m\pi \frac{x}{L})$$
$$V_m = \sin(m\pi \frac{x}{L})$$
$$U_m = \cos(m\pi \frac{x}{L})$$
$$(\varphi_x)_m = \cos(m\pi \frac{x}{L})$$
$$(\varphi_y)_m = \sin(m\pi \frac{x}{L})$$

at y = 0, b

$w = M_{yy} = \varphi_x = N_{yy} = u = 0$

$$W_n = \sin(n\pi \frac{y}{b})$$
$$V_n = \cos(n\pi \frac{y}{b})$$
$$U_n = \sin(n\pi \frac{y}{b})$$
$$(\varphi_x)_n = \sin(n\pi \frac{x}{b})$$
$$(\varphi_y)_n = \cos(n\pi \frac{x}{b})$$

(B1)

S4:

at x = 0, L

$w = M_{xx} = \varphi_y = u = v = 0$

$$W_m = \sin(m\pi \frac{x}{L})$$
$$V_m = \sin(m\pi \frac{x}{L})$$
$$U_m = \sin(m\pi \frac{x}{L})$$
$$(\varphi_x)_m = \cos(m\pi \frac{x}{L})$$
$$(\varphi_y)_m = \sin(m\pi \frac{x}{L})$$

at y = 0, b

$w = M_{yy} = \varphi_x = u = v = 0$

$$W_n = \sin(n\pi \frac{y}{b})$$
$$V_n = \sin(n\pi \frac{y}{b})$$
$$U_n = \sin(n\pi \frac{y}{b})$$
$$(\varphi_x)_n = \sin(n\pi \frac{x}{b})$$
$$(\varphi_y)_n = \cos(n\pi \frac{x}{b})$$

(B2)

C3:

at x = 0, L

$w = \varphi_x = \varphi_y = N_{xx} = v = 0$

$$W_m = \left(\cos\frac{\lambda_i x}{L} - \cosh\frac{\lambda_i x}{L}\right) - \gamma_i\left(\sin\frac{\lambda_i x}{L} - \sinh\frac{\lambda_i x}{L}\right)$$
$$V_m = \sin(m\pi \frac{x}{L})$$
$$U_m = \cos(m\pi \frac{x}{L})$$
$$(\varphi_x)_m = \sin(m\pi \frac{x}{L})$$
$$(\varphi_y)_m = \sin(m\pi \frac{x}{L})$$

at y = 0, b

$w = \varphi_x = \varphi_y = N_{yy} = u = 0$

$$W_n = \left(\cos\frac{\lambda_i y}{b} - \cosh\frac{\lambda_i y}{b}\right) - \gamma_i\left(\sin\frac{\lambda_i y}{b} - \sinh\frac{\lambda_i y}{b}\right)$$
$$V_n = \cos(n\pi \frac{y}{b})$$
$$U_n = \sin(n\pi \frac{y}{b})$$
$$(\varphi_x)_n = \sin(n\pi \frac{x}{b})$$
$$(\varphi_y)_n = \sin(n\pi \frac{x}{b})$$

(B3)

C4:

at x = 0, L

w = φ_x = φ_y = v = 0

$$W_m = \left(\cos\frac{\lambda_i x}{L} - \cosh\frac{\lambda_i x}{L}\right) - \gamma_i\left(\sin\frac{\lambda_i x}{L} - \sinh\frac{\lambda_i x}{L}\right)$$

$$V_m = \sin(m\pi\frac{x}{L})$$

$U_m = \sin(m\pi\frac{x}{L})$; u = 0 at x = L

$U_m = \cos(m\pi\frac{x}{L})$; u ≠ 0 at x = 0

$(\varphi_x)_m = \sin(m\pi\frac{x}{L})$, $(\varphi_y)_m = \sin(m\pi\frac{x}{L})$

at y = 0, b

w = φ_x = φ_y = u = v = 0

$$W_n = \left(\cos\frac{\lambda_i y}{b} - \cosh\frac{\lambda_i y}{b}\right) - \gamma_i\left(\sin\frac{\lambda_i y}{b} - \sinh\frac{\lambda_i y}{b}\right)$$

$$V_n = \sin(n\pi\frac{y}{b})$$

$$U_n = \sin(n\pi\frac{y}{b})$$

$$(\varphi_x)_n = \sin(n\pi\frac{x}{b})$$

$$(\varphi_y)_n = \sin(n\pi\frac{x}{b})$$

(B4)

In general, the displacement functions are expressed as in the Equations (3.15) through (3.19) and functions U_m, U_n, V_m, V_n, W_m, W_n, φ_x and φ_y are selected from the above expressions for different boundary conditions. L and b are the length and width of the plate respectively; N_{ij} and M_{ij} are the resultant force and moment respectively, where i, j = x, y. The values of λ_i and γ_i can be found in Bertholet [103]. Si and Ci denote the simply-supported and clamped boundary conditions respectively, where i = 3, 4.

Different Edge Conditions of the Curved Plates

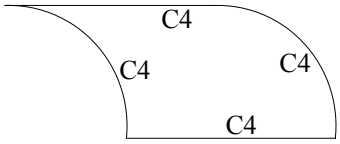

Clamped-Clamped (C4-C4)

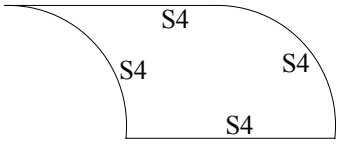

Simply-Supported (S4-S4)

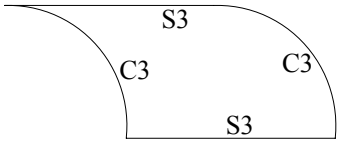

Clamped-Simply Supported (C3-S3)

The details about the boundary conditions where S3, S4, C3 and C4 are, respectively, given by the Eqs. (B1) through (B4).

System Equations of First-order Shear Deformation Shell Theory

For balanced symmetric laminate, B_{11}= B_{12}= B_{16}= B_{22}= B_{26}= B_{66}=0, and A_{16}=A_{26}=0; applying these conditions to the Eq. (3.25), the following expressions for L_{IJ}^{st} are obtained:

$$L_{IJ}^{11} = \sum_{m=1}^{M}\sum_{n=1}^{N} \left\{ \sum_{i=1}^{M}\sum_{j=1}^{N} \left\{ \int_0^L A_{66} U_m U_i dx \int_0^b \frac{dU_n}{dy}\frac{dU_j}{dy} dy \right.\right.$$
$$\left.\left. + \int_0^L A_{11} \frac{dU_m}{dx}\frac{dU_i}{dx} dx \int_0^b U_n U_j dy + 1/4 \int_0^L D_{66} \left(\frac{c_1}{R}\right)^2 U_m U_i dx \int_0^b \frac{dU_n}{dy}\frac{dU_j}{dy} dy \right\}\right\} \quad \text{(B5)}$$

$$L_{IJ}^{12} = \sum_{m=1}^{M}\sum_{n=1}^{N} \left\{ \sum_{i=1}^{M}\sum_{j=1}^{N} \left\{ -\frac{1}{4}\int_0^L \left(\frac{c_1}{R}\right)^2 D_{66} U_m \frac{dV_i}{dx} dx \int_0^b \frac{dU_n}{dy} V_j dy - \int_0^L \frac{c_2}{R} A_{14} \frac{dU_m}{dx} V_i dx \int_0^b U_n V_j dy \right.\right.$$
$$+ \int_0^L A_{66} U_m \frac{dV_i}{dx} dx \int_0^b \frac{dU_n}{dy} V_j dy + \int_0^L A_{12} \frac{dU_m}{dx} V_i dx \int_0^b U_n \frac{dV_j}{dy} dy$$
$$\left.\left. + \frac{1}{2}\int_0^L B_{46} \frac{c_1 c_2}{R^2} U_m V_i dx \int_0^b \frac{dU_n}{dy} V_j dy - \int_0^L A_{46} \frac{c_2}{R} U_m V_i dx \int_0^b \frac{dU_n}{dy} V_j dy \right\}\right\} \quad \text{(B6)}$$

$$L_{IJ}^{13} = \sum_{m=1}^{M}\sum_{n=1}^{N} \left\{ \sum_{i=1}^{M}\sum_{j=1}^{N} \left\{ \int_0^L A_{15} \frac{dU_m}{dx}\frac{dW_i}{dx} dx \int_0^b U_n W_j dy + \int_0^L A_{56} U_m \frac{dW_i}{dx} dx \int_0^b \frac{dU_n}{dy} W_j dy \right.\right.$$
$$+ \int_0^L A_{14} \frac{dU_m}{dx} W_i dx \int_0^b U_n \frac{dW_j}{dy} dy + \int_0^L A_{46} U_m W_i dx \int_0^b \frac{dU_n}{dy}\frac{dW_j}{dy} dy$$
$$+ \int_0^L A_{12} \frac{1}{R}\frac{dU_m}{dx} W_i dx \int_0^b U_n W_j dy - \frac{1}{2}\int_0^L B_{56} \frac{c_1}{R} U_m \frac{dW_i}{dx} dx \int_0^b \frac{dU_n}{dy} W_j dy$$
$$\left.\left. - \frac{1}{2}\int_0^L B_{46} \frac{c_1}{R} U_m W_i dx \int_0^b \frac{dU_n}{dy}\frac{dW_j}{dy} dy \right\}\right\} \quad \text{(B7)}$$

where c_1 and c_2 are the tracer coefficients used to express the strain and curvature fields that correspond to different shell theories. In a similar manner, the equations for rest of the coefficients L_{IJ}^{st} (s, t = 1, 2, 3, 4, 5) can be written.

G_{IJ}^{st} can be expressed as:

$$G_{IJ}^{22} = \sum_{m=1}^{M}\sum_{n=1}^{N} \left\{ \sum_{i=1}^{M}\sum_{j=1}^{N} \left\{ \int_0^L \frac{dV_m}{dx}\frac{dV_i}{dx} dx \int_0^b V_n V_j dy \right\}\right\} \quad \text{(B8)}$$

$$G_{IJ}^{33} = \sum_{m=1}^{M}\sum_{n=1}^{N} \left\{ \sum_{i=1}^{M}\sum_{j=1}^{N} \left\{ \int_0^L \frac{dW_m}{dx}\frac{dW_i}{dx} dx \int_0^b W_n W_j dy \right\}\right\} \quad \text{(B9)}$$

where L and b are the length and the width of a plate respectively and L denotes the total length of a plate, that is, $L = L_{tap}$ for taper configurations A and B, and L = L for hybrid configuration (see Fig. 1.4).

APPENDIX C

Shape Functions for the Nine-node Lagrange Element

$$\overline{N}_1 = 4(\overline{x} - \frac{1}{2}\overline{L})(\overline{x} - \overline{L})/\overline{L}^2\ (\overline{y} - \frac{1}{2}\overline{b})(\overline{y} - \overline{b})/\overline{b}^2 \qquad \overline{N}_2 = -8(\overline{x} - \frac{1}{2}\overline{L})(\overline{x} - \overline{L})/\overline{L}^2\ \overline{y}(\overline{y} - \overline{b})/\overline{b}^2$$

$$\overline{N}_3 = 4(\overline{x} - \frac{1}{2}\overline{L})(\overline{x} - \overline{L})/\overline{L}^2\ \overline{y}(\overline{y} - \frac{1}{2}\overline{b})/\overline{b}^2 \qquad \overline{N}_4 = -8\overline{x}(\overline{x} - \overline{L})/\overline{L}^2\ (\overline{y} - \frac{1}{2}\overline{b})(\overline{y} - \overline{b})/\overline{b}^2$$

$$\overline{N}_5 = 16\overline{x}(\overline{x} - \overline{L})/\overline{L}^2\ \overline{y}(\overline{y} - \overline{b})/\overline{b}^2 \qquad \overline{N}_6 = -8\overline{x}(\overline{x} - \overline{L})/\overline{L}^2\ \overline{y}(\overline{y} - \frac{1}{2}\overline{b})/\overline{b}^2 \qquad \text{(C1)}$$

$$\overline{N}_7 = 4\overline{x}(\overline{x} - \frac{1}{2}\overline{L})/\overline{L}^2(\overline{y} - \frac{1}{2}b)(\overline{y} - \overline{b})/\overline{b}^2 \qquad \overline{N}_8 = -8\overline{x}(\overline{x} - \frac{1}{2}\overline{L})/\overline{L}^2\ \overline{y}(\overline{y} - \overline{b})/\overline{b}^2$$

$$\overline{N}_9 = 4\overline{x}(\overline{x} - \frac{1}{2}\overline{L})/\overline{L}^2\ \overline{y}(\overline{y} - \frac{1}{2}\overline{b})/\overline{b}^2$$

where $\overline{L}$ and $\overline{b}$ are the length and the width of an element respectively with respect to local coordinates; and $(\bar{x}, \bar{y})$ is the set of local coordinates.

$$\left[B_L^i\right] = \begin{bmatrix} \frac{dN_i}{dx} & 0 & 0 & 0 & 0 \\ 0 & \frac{dN_i}{dy} & \frac{N_i}{R} & 0 & 0 \\ \frac{dN_i}{dy} & \frac{dN_i}{dx} & 0 & 0 & 0 \\ 0 & 0 & 0 & \frac{dN_i}{dx} & 0 \\ 0 & 0 & 0 & 0 & \frac{dN_i}{dy} \\ -\frac{c_1}{2R}\frac{dN_i}{dy} & \frac{c_1}{2R}\frac{dN_i}{dx} & 0 & \frac{dN_i}{dy} & \frac{dN_i}{dx} \\ 0 & -\frac{c_2}{R}N_i & \frac{dN_i}{dy} & 0 & N_i \\ 0 & 0 & \frac{dN_i}{dx} & N_i & 0 \end{bmatrix} \qquad \text{(C2)}$$

$$\left[g_L^i\right] = \begin{bmatrix} 0 & 0 & 0 & 0 & 0 \\ 0 & 0 & 0 & 0 & 0 \\ 0 & 0 & \frac{dN_i}{dx} & 0 & 0 \\ 0 & 0 & 0 & 0 & 0 \\ 0 & 0 & 0 & 0 & 0 \end{bmatrix} \qquad \text{(C3)}$$

Boundary Conditions for First-order Shear Deformation Shell Theory

S3:

at x = 0, L (C4)
$w = M_{xx} = \varphi_y = N_{xx} = v_o = 0$
at y = 0, b
$w = M_{yy} = \varphi_x = N_{yy} = u_o = 0$

S4:

at x = 0, L (C5)
$w = M_{xx} = \varphi_y = u_o = v_o = 0$
at y = 0, b
$w = M_{yy} = \varphi_x = u_o = v_o = 0$

C3:

at x = 0, L (C6)
$w = \varphi_x = \varphi_y = N_{xx} = v_o = 0$
at y = 0, b
$w = \varphi_x = \varphi_y = N_{yy} = u_o = 0$

C4:

at x = 0, L (C7)
$w = \varphi_x = \varphi_y = u_o = v_o = 0$
at y = 0, b
$w = \varphi_x = \varphi_y = u_o = v_o = 0$

where (u_o, v_o, w_o) constitute the mid-plane displacement field that refers to the global coordinate system (x, y, z) as shown in Fig. 2.1; L and b are the length and width of a plate respectively; N_{ij} and M_{ij} are the resultant forces and moments respectively, where i, j = x, y.

Different Edge Conditions of the Curved Plates

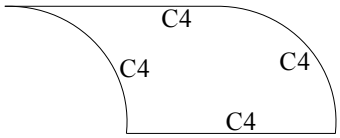

Clamped-Clamped (C4-C4)

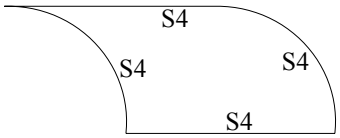

Simply-Supported (S4-S4)

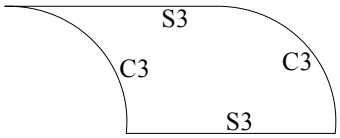

Clamped-Simply Supported (C3-S3)

The details about the boundary conditions S3, S4, C3 and C4 are, respectively, given by the Eqs. (C4) through (C7).

Calculation of the Weight Savings and the Gain of Strengths

To calculate the weight of a tapered laminate, the laminate is divided into several segments based on the horizontal distribution of resin pockets. For example, taper configuration A has only one segment but the taper configuration B has three segments. The weight of all the segments is combined to get the weight of the laminate. The resin pocket is considered (imagined) to be made up of layers of isotropic resin material and the height of the resin pocket is equivalent to the number of drop-off plies.

The weight of the uniform flat laminate which is to be made into the tapered one is:

$$W_{ul} = \sum_{n=1}^{N} [n \times (PDO \times \rho_r + NURP \times \rho_r + NCP \times \rho_c) \times L_{rp} \times t_{cp} \times b] \tag{C8}$$

The weight of the tapered flat laminate can be expressed as:

$$W_{tl} = \sum [n \times (\tfrac{1}{2} \times DOP \times \rho_r + NURP \times \rho_r + NCP \times \rho_c) \times L_{rp} \times t_{cp} \times b] \tag{C9}$$

The weight of the tapered curved laminate can be expressed as:

$$W_{tcl} = \sum [n \times (\tfrac{1}{2} \times DOP \times \rho_r + NURP \times \rho_r + NCP \times \rho_c) \times L_{rp} \times t_{cp} \times R \times \zeta] \tag{C10}$$

where ‘n’ denotes the number of segments, ‘PDO’ denotes the plies to be dropped-off, ‘DOP’ denotes the dropped-off plies, ρ_r denotes the density of resin, ‘NURP’ denotes the number of uniform (imagined) resin plies, ‘NCP’ denotes the number of composite plies, ρ_c denotes density of composite, L_{rp} denotes the length of the resin pocket, t_{cp} denotes the thickness of the composite plies, ‘b’ denotes the width of the flat plate, ‘R’ denotes the radius of the curved plate, and ‘ζ’ denotes the center angle of the curved plate.

The properties mentioned in the Eqs. (C8) and (C9) for the plate with one segment used in the Fig. 4.6 are:

n = 1, PDO = 18, ρ_r = 1050 kg/m^3, NURP = 6, NCP = 12, ρ_c = 1480 kg/m^3, L_{rp} = 0.8594 m, t_{cp} = 0.000125 m and b = 0.8594 m.

Therefore, the weight of the uniform flat plate corresponding to the point ‘P’ in the Fig. 4.6 is:

$$W^P = (18\times1050 + 6\times1050 + 12\times1480)\times0.8594\times.000125\times0.8594$$
$$W^P = 3.96 \text{ Kg} \tag{C11}$$

And the weight of the tapered plate corresponding to the point 'Q' in the Fig. 4.6 is:

$$W^Q = (1/2\times18\times1050 + 6\times1050 + 12\times1480)\times.8594\times.000125\times.8594$$
$$W^Q = 3.09 \text{ Kg} \tag{C12}$$

The weight savings of the tapered plate with respect to the uniform plate is expressed as:

$$W_s = (W^P - W^Q)/W^P \times 100\% \tag{C13}$$

From the Eqs. (C11) through (C13), the weight savings of the plate used in the Fig. 4.6 with 18 drop-off plies is **21.96 %.**

The gain of strength of a curved tapered plate with respect to a flat tapered plate can be expressed as:

$$G_s = (S^R - S^Q)/S^R \times 100\% \tag{C14}$$

From the Eq. (C14), the gain of strength of the plate used in the Fig. 4.6 with 18 drop-off plies is **82.47 %.**

APPENDIX D

Strain-Nodal Displacement Matrix

$$\left[B_L^i\right] = \begin{bmatrix} \frac{dN_i}{dx} & 0 & 0 & 0 & 0 \\ 0 & \frac{dN_i}{dy} & \frac{N_i}{R} & 0 & 0 \\ \frac{dN_i}{dy} & \frac{dN_i}{dx} & 0 & 0 & 0 \\ 0 & 0 & 0 & \frac{dN_i}{dx} & 0 \\ 0 & 0 & 0 & 0 & \frac{dN_i}{dy} \\ 0 & 0 & 0 & \frac{dN_i}{dy} & \frac{dN_i}{dx} \\ 0 & -\frac{c_1}{R}N_i & \frac{dN_i}{dy} & 0 & N_i \\ 0 & 0 & \frac{dN_i}{dx} & N_i & 0 \end{bmatrix} \tag{D1}$$

Matrices Required to Calculate $\{\boldsymbol{\varepsilon_N}\}$

$$[H]=\begin{bmatrix} 0 & \frac{dw_o}{dx} & 0 \\ -\left(\frac{dw_o}{dy}-\frac{c_1 v_o}{R}\right) & 0 & \left(\frac{dw_o}{dy}-\frac{c_1 v_o}{R}\right) \\ -\frac{dw_o}{dx} & \left(\frac{dw_o}{dy}-\frac{c_1 v_o}{R}\right) & \frac{dw_o}{dx} \\ 0 & 0 & 0 \\ 0 & 0 & 0 \\ 0 & 0 & 0 \\ 0 & 0 & 0 \\ 0 & 0 & 0 \end{bmatrix} \tag{D2}$$

$$[S]=\begin{bmatrix} 0 & \frac{c_1 N_i}{R} & 0 & 0 & 0 \\ 0 & 0 & \frac{dN_i}{dx} & 0 & 0 \\ 0 & 0 & \frac{dN_i}{dy} & 0 & 0 \end{bmatrix} \tag{D3}$$

Matrices Required to Calculate $[\boldsymbol{K_{eT}}]$

$$[N_L]=\begin{bmatrix} N_{L2} & -N_{L3} & -N_{L2} \\ -N_{L3} & N_{L1} & N_{L3} \\ -N_{L2} & N_{L3} & N_{L2} \end{bmatrix} \tag{D4}$$

$$[N_N]=\begin{bmatrix} N_{N2} & -N_{N3} & -N_{N2} \\ -N_{N3} & N_{N1} & N_{N3} \\ -N_{N2} & N_{N3} & N_{N2} \end{bmatrix} \tag{D5}$$

$$\{N_{Li}\}_{8\times1}=\{N_{L1},\quad N_{L2},\quad \ldots\ldots\quad N_{L8}\}^t=[E']_{8\times8}\{\varepsilon_L\}_{8\times1} \tag{D6}$$

$$\{N_{Ni}\}_{8\times1}=\{N_{N1},\quad N_{N2},\quad \ldots\ldots\quad N_{N8}\}^t=[E']_{8\times8}\{\varepsilon_N\}_{8\times1} \tag{D7}$$

Boundary Conditions for First-order Shear Deformation Shell Theory

For first-order shear deformation shell theory, the BCs of clamped-clamped (C4-C4) plate are mentioned below:

at x = 0
$w = \varphi_x = \varphi_y = u_o = v_o = 0$

at x = L
$w = \varphi_x = \varphi_y = v_o = 0;\ u_o \neq 0$ (D8)

at y = 0, b
$w = \varphi_x = \varphi_y = u_o = v_o = 0$

where (u_o, v_o, w_o) denotes the mid-plane displacement field that refers to the global coordinate system (x, y, z) as shown in Fig. 2.1; L and b are the length and width of the plate respectively; N_{ij} and M_{ij} are the resultant force and moment respectively, where i, j = x, y.

APPENDIX E

The following Fig. E-1 is the re-plot of Fig. 5.3 of chapter five from which the stability limit load is calculated at the point where the transverse deflection increased significantly with the small increment of compressive load and this value is to be equal to 129 MPa.

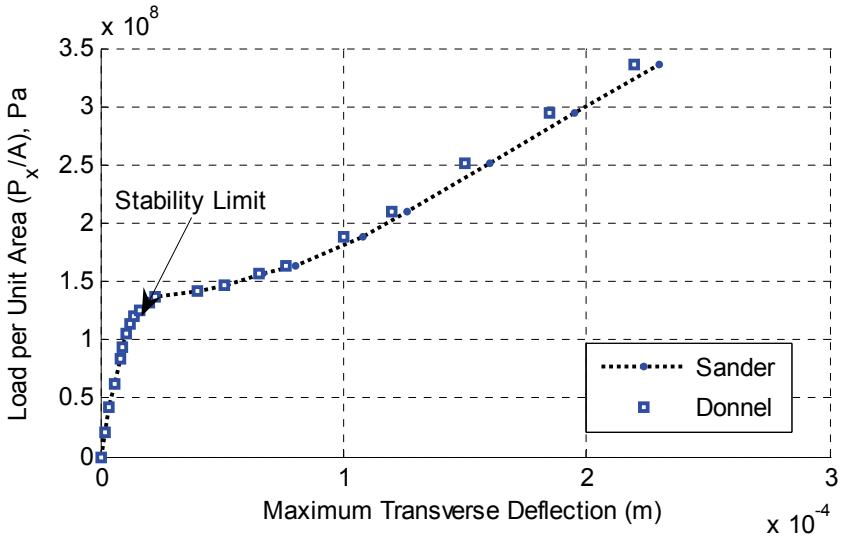

Figure E-1: Load-deflection curve for uniform-thickness curved plate with ply configuration $[0_2/90_2]_s$.

The neighborhood of limit load of the Fig. E-1 is plotted in the Fig. E-2 to show the critical point where the transverse deflection increased significantly with the small change of compressive load.

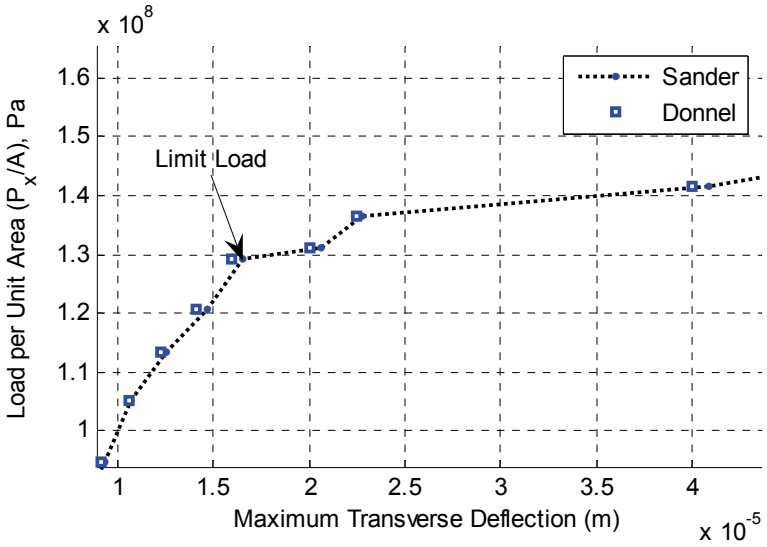

Figure E-2: Neighborhood of limit load for uniform-thickness curved plate with ply configuration $[0_2/90_2]_s$.

ACKNOWLEDGEMENT

The author of the present thesis and the supervisor would like to acknowledge the support provided for the present work by the Natural Sciences and Engineering Research Council of Canada (NSERC) and Concordia University.

REFERENCES

1. He, K., Hoa, S. V. and Ganesan, R., "The Study of Tapered Laminated Composite Structures: A Review", Composites Science and Technology, Vol. 60, 2000, pp. 2643-2657.
2. Curry, J. M., Johnson, E. R. and Starnes Jr., J. H., "Effect of Dropped Plies on the Strength of Graphite-epoxy Laminates", AIAA Journal, Vol. 30(2), 1992, pp. 449-456.
3. Hoa, S. V., Du, B. L. and Vu-Khanh, T., "Interlaminar Stresses in Tapered Laminates", Polymer Composites, Vol. 9(5), 1988, pp. 337-344.
4. Daoust, J. and Hoa, S. V., "Parameters Affecting Interlaminar Stresses in Tapered Laminates Under Static Loading Conditions", Polymer Composites, Vol. 10(5), 1989, pp. 374-83.
5. Llanos, A. S. and Vizzini, A. J., "The Effect of Film Adhensive on the Delamination Strength of Tapered Composites", Journal of Composite Materials, Vol. 26(13), 1992, pp. 1968-1983.
6. Thomas, D. M. and Webber, P. H., "A Design Study into the Delamination Behavior of Tapered Composites", Composite Structures, Vol. 27, 1994, pp. 379-88.
7. Piskunov, V. G. and Sipetov, V. S., "Calculation of Tapered Laminated Shells Consisting of Anisotropic Composite Materials for Static and Thermal Loads", Kiev Highway Institute, Translated from Problemy Prochnosti, No. 10, October 1987, pp. 79-82.

8. Kee, Y. and Kim, J., "Vibration Characteristics of Initially Twisted Rotating Shell Type Composite Blades", Composite Structures, Vol. 64, 2004, pp. 151-159.
9. Lars, A. S. and Eggwertz, S., "*Shell stability handbook*", Elsevier Science Publishers Ltd., London, 1992.
10. Lorenz, R., "Achsensymetrische Verzerrungen in Dunnwandigen Holzylindern", Zeitschrift VDI, Bd 52, S 1706-1713, 1908, (Cross referenced from many other references).
11. Timoshenko, S., "Einige Stabilitatsprobleme der Elasticitatstheorie", Zeitschrift Mathematik und Physik,, Bd 58, S 337-385, 1910, (Cross referenced from many other references).
12. Ambartsumyan, S.A., "On the Theory of Anisotropic Shallow Shells", NACA Technical Memorandum- 1424, USA, Original in 1948 and Translated in 1956.
13. Viswanathan, A.V., Tamekuni, M. and Baker, L.L., "Elastic Stability of Laminated, Flat and Curved, Long Rectangular Plates Subjected to Combined In-plane Loads", NASA CR-2330, USA, 1974.
14. Hilburger, M. W. and Starnes Jr., J. H., "Buckling Behavior of Compression-loaded Composite Cylindrical Shells with Reinforced Cutouts", NASA/TM-2004-212656, Langley Research Center, Hampton, Virginia, USA, Sept 2004.
15. Michael, P. N., "Non Dimensional Parameters and Equations for Buckling of Symmetrically Laminated Thin Elastic Shallow Shells", Langley Research Center Hampton, Virginia 23665, NASA, USA, March 1991.
16. Tennyson, R. C., "Buckling Of Laminated Composite Cylinders: A Review", Composites, Vol. 6(17), 1975, pp. 17-24.

17. Simitses, G. J., “Buckling Of Moderately Thick Laminated Cylindrical Shells: A Review”, Composites Part B, Vol. 27b, 1996, pp. 581-587.
18. Buragohain, M. and Velmurugan, R., “Buckling Analysis of Composite Hexagonal Lattice Cylindrical Shell using Smeared Stiffener Model**”,** Defense Science Journal, Vol. 59 (3), May 2009, pp. 230-238.
19. Wong, W. H., Ip, K. H. and Tse, P. C., “Buckling Stresses of Composite Tubes Under Biaxial Compressive Loads”, Experimental Mechanics, Vol. 38(2), June 1998, pp. 126-131.
20. Rao, K. M. and Meyer-Piening, H.-R., “Buckling Analysis of FRP Faced Cylindrical Sandwich Panel under Combined Loading”, Composite Structures, Vol. 14, 1990, pp. 15-34.
21. Jaunky, N. and Knight Jr., N. F., “An Assessment of Shell Theories For Buckling of Circular Cylindrical Laminated Composite Panels Loaded in Axial Compression”, International Journal Of Solids and Structures, Vol. 36, 1999, pp 3799-3820.
22. Barai, A. and Durvasula, S., “Vibration and Buckling of Hybrid Laminated Curved Panels”, Composite Structures, Vol. 21, 1992, pp. 15-27.
23. Yang, H. T. Y., Saigal, S. and Liaw, D. G., “Advances of Thin Shell Finite Elements and Some Applications-Version I”, Computers and Structures, Vol. 35(4), 1990, pp. 481-504.
24. Kapania, R. K., “A Review on the Analysis of Laminated Shells”, Journal of Pressure Vessel Technology, Vol. 111, 1989, pp. 88-96.
25. Gilewski, W., “A Survey of Finite Element Models for the Analysis of Moderately Thick Shells”, Finite Elements in Analysis and Design, Vol. 9, 1991, pp. 1-21.

26. Noor, A. K. and Burton, W. S., “Assessment of Computational Models for Multilayered Composite Shells”, Applied Mechanics Review, Vol. 43(4), 1990, pp. 67- 97.
27. Reddy, J. N. and Robbins Jr., D. H., “Theories and Computational Models for Composite Laminates”, Applied Mechanics Review, Vol. 47(6), 1994, pp. 147-169.
28. Mackerle, J., “Finite Element Linear and Nonlinear, Static and Dynamic Analysis of Structural Elements: A Bibliography (1992-1995)”, Engineering Computations, Vol. 14(4), 1997, pp. 347-440.
29. Yang, H. T. Y., Saigal, S., Masud, A. and Kapania, R. K., “A Survey of Recent Shell Finite Elements”, International Journal for Numerical Methods in Engineering, Vol. 47, 2000, pp. 101-127.
30. Macneal, R. H. and Harder, R. L., “Eight Nodes or Nine”, International Journal for Numerical Methods in Engineering, Vol. 33, 1992, pp. 1049-1058,
31. Parisch, H., “A Critical Survey of the 9-Node Degenerated Shell Element with Special Emphasis on Thin Shell Application and Reduced Integration”, Computer Methods in Applied Mechanics and Engineering, Vol. 20, 1979, pp. 323-350.
32. Belytschko, T., Liu, W.-K., Ong, J. S.-J. and Lam, D., “Advances in Finite Element Technology - Implementation and Application of a 9-Node Lagrange Shell Element with Spurious Mode Control”, Computers and Structures, Vol. 20(l-3), 1985, pp. 121-128.
33. Lee, C. K. and Hobbs, R. E., “Automatic Adaptive Refinement for Shell Analysis Using Nine-Node Assumed Strain Element”, International Journal for Numerical Methods in Engineering, Vol. 40, 1997, pp. 3601-3638.

34. Chang, T.Y., Saleeb, A.F. and Graf, W., "On the Mixed Formulation of a 9-Node Lagrange Shell Element", Computer Methods in Applied Mechanics and Engineering, Vol. 73, 1989, pp. 259-281.
35. Kebari, H. and Cassell, A. C., "Non-Conforming Modes Stabilization of A Nine-Node Stress-Resultant Degenerated Shell Element With Drilling Freedom", Computers and Structures, Vol. 40(3), 1991, pp. 569-580.
36. Yeom, C. H., Scardera, M. P. and Lee, S. W., "Shell Analysis With A Combination of Eight Node and Nine Node Finite Elements" Computers and Structures, Vol. 28(2), 1988, pp. 155-163.
37. Jayasankar, S., Mahesh, S., Narayanan, S. and Padmanabhan, C., "Dynamic Analysis of Layered Composite Shells Using Nine Node Degenerate Shell Elements", Journal of Sound and Vibration, Vol. 299(1-2), 2007, pp. 1-11.
38. MacNeal, R. H., *Finite elements: their design and performance*, Published by Marcel Dekker, 1994.
39. Chapellet, D. and Bathe, K. J., "Fundamental Considerations for the Finite Element Analysis Of Shell Structures", Computers and Structures, Vol. 66(1), 1998, pp. 19-36.
40. Reddy, J. N. and Pandey, A. K., "A First-Ply Failure Analysis of Composite Laminates", Computers and Structures, Vol. 25, 1987, pp. 371-393.
41. Tsai, S. W., "A Survey of Macroscopic Failure Criteria for Composite Materials", Journal of Reinforced Plastics and Composites, Vol. 3, January 1984, pp. 40-62.

42. Nahas, M.N, “Survey of Failure and Post-Failure Theories of Laminated Fiber-reinforced Composites”, Journal of Composites Technology & Research, Vol. 8(4), December 1986, pp. 138-153.
43. Soden, P.D., Kaddour, A.S. and Hinton, M.J., “Recommendations for Designers and Researchers Resulting from the World-Wide Failure Exercise”, Composites Science And Technology, Vol. 64, 2004, pp. 589-604.
44. Mortensen, F., “Development of Tools for Engineering Analysis and Design of High Performance FRP-Composite Structural Elements”, Ph.D. Thesis, Institute of Mechanical Engineering, Alborg University, Denmark, 1998.
45. He, K., Ganesan, R. and Hoa, S. V., “Interlaminar Stress and Delamination Analysis of Internally-Tapered Composite Laminates”, Journal of Reinforced Plastics and Composites, Vol. 23(7), 2004, pp. 707-727.
46. Fish, J. C. and Lee, S. W., “Delamination of Tapered Composite Structures”, Engineering Fracture Mechanics, Vol. 34, No. 1, 1989, pp. 43-54.
47. Kassapoglou, C., “Determination of Interlaminar Stresses in Composite Laminates under Combined Loads”, Joumal of Reinforced Plastics and Composites, Vol. 9, January 1990, pp.
48. Waltz, T. L. and Vinson, J. R., “Interlaminar Stresses in Laminated Cylindrical Shells of Composite Materials”, AIAA Journal, Vol. 14, No. 9, September 1976, pp.
49. Pipes, R. B. and Pagano, N.J., “Interlaminar Stresses in Composite Laminates Under Uniform Axial Extension” Journal of Composite Materials, Vol. 4, 1970, pp: 538.

50. Curry, J. M., "Effect of Dropped Plies on The Strength of Graphite-Epoxy Laminates", *AIAA Journal*, Vol. 30, No. 2, February 1992, pp. 449-456.

51. Ganesan, R. and Liu, D. Y., "Progressive Failure and Post-Buckling Response of Tapered Composite Plates under Uni-Axial Compression", Journal of Composite Structures, Vol. 82, 2008, pp. 159-176.

52. Reddy, J. N., "A Generalization of Two-Dimensional Theories of Laminated Composite Plates". Communication Applied Numerical Methods, Vol. 3, 1987, pp. 173-180.

53. Kant, T. and Swaminathan, K., "Estimation of Transverse/Interlaminar Stresses in Laminated Composites-A Selective Review and Survey of Current Developments", Composite Structures, Vol. 49, 2000, pp. 65-75.

54. Salamon. N. J., "An Assessment of the Interlaminar Stress Problem in Laminated Composites", Journal of Composite Materials Supplement, Vol. 14, 1980, pp. 177-194.

55. Resnyansky, A.D., "The Impact Response of Composite Materials Involved in Helicopter Vulnerability Assessment: Literature Review - Part 2", DSTO-TR-1842 Part 2, Defense Science and Technology Organization, Australia, 2006.

56. Bolotin, V. V., "Delaminations in Composite Structures: its Origin, Buckling, Growth and Stability", Composites: Part B, Vol. 27(2), 1996, pp. 129-145.

57. Bolotin. V. V., "Mechanics of Delaminations in Laminate Composite Structures", Translated From Mekhanika Kompozitnykh Materialov, Vol. 37, Nos. 5/6, 2001, pp. 585-602.

58. Donnell, L. H. and Wa, C. C., “Effect of Imperfections on Buckling of Thin Cylinders and Columns under Axial Compression”, Journal of Applied Mechanics, Vol. 17, 1950, pp 73-83.

59. von Kármán, T., "Festigkeitsproblem im Maschinenbau", Encyl. der Mathematische Wissenschaften, IV, 311–385, 1910, (Cross referenced from many other references).

60. Reddy, J. N., “Geometrically Nonlinear Transient Analysis of Laminated Composite Plates”, AIAA Journal, Vol. 21(4), 1983, pp.621-629.

61. Liao, C. L. and Reddy, J. N., “Continuum-Based Stiffened Composite Shell Element for Geometrically Nonlinear Analysis”, AIAA Journal, Vol. 27(1), 1989, pp. 95-101.

62. Reddy, J. N., *An introduction to nonlinear finite element analysis*, Oxford University Press, Oxford, UK, 2004.

63. Kayuk, Ya. F., *Problems in Parameter Expansion Methods*, Naukova Dumka, Kiev, 1980 (Cross referenced from many other references).

64. Kayuk, Ya. F., *Geometrically Nonlinear Problems in the Theory of Plates and Shells*, Naukova Dumka, Kiev, 1987 (Cross referenced from many other references).

65. Vorovich, I. I., "Direct methods in the nonlinear theory of flat shells”, Prikl. Mat.Mekh., Vol. 20(4), 1956, pp. 449-474 (Cross referenced from many other references).

66. Vorovich, I. I., *Mathematical Problems in the Nonlinear Theory of Flat Shells*, Nauka, Moscow, 1989 (Cross referenced from many other references).

67. Newton, I., "De analysis per aequationes infinitas (1690)", in The Mathematical papers of Isaac Newton, Vol. 11 (1667-1670), D.T. Whiteside (ed), Cambridge University Press, Cambridge, UK, 1968, pp. 207-247 (Cross referenced from many other references).

68. Raphson, J., "Analysis Aequationum universalis seu ad aequationes algebricas resolvendas methods generalis et expedica, ex nove infinitarum serierum doctorina deducta ac demonstrata", London, 1690 (Cross referenced from many other references).

69. Bellman, R. E. and Kalaba, R. R., *Quasilinearization and Nonlinear Boundary-Value Problems*, American-Elsevier, New York, 1965.

70. Grigorenko, Ya. M. and Kryukov, N. N., *Numerical Solution of Static Problems of Flexible Layered Shells with Varying Parameters*, Naukova Dumka, Kiev, 1988 (Cross referenced from many other references).

71. Thurston, G. A., "Newton's Method Applied to Problems in Nonlinear Mechanics", Journal of Applied Mechanics, Vol. 32, 1965, pp. 383-388.

72. Haeseler, F. V. and Peitgen, H. O., "Newton's Method and Complex Dynamical System", Acta Applicandae Mathematicae, Vol. 13, 1988, pp 3-58.

73. Riks, E., "The Application of Newton's Method to the Problem of Elastic Stability", Journal of Applied Mechanics, Vol. 39, 1972, pp. 1060-1066.

74. Wempner, G. A., "Discrete Approximations Related to Non-Linear Theories of Solids", International Journal of Solids and Structures, Vol. 7, 1971, pp. 1581-1589.

75. Zhu, Ju-fen and Chu, Xiao-ting, "An Improved Arc-length Method and Application in the Post-buckling Analysis for Composite Structures", Applied Mathematics and Mechanics, Vol. 23(9), 2002, pp. 1081-1088.

76. Bruce, W. R. and Siegfried, F., "Improved Arc Length Orthogonality Methods for Non-linear Finite Element Analysis", Computers and Structures, Vol. 27(5), 1987, pp. 625-630.

77. Crisfield, M. A., *Non-linear Finite Element Analysis of Solids and Structures, Volume -1*, John Wiley and Sons Ltd., England, 2000.

78. Carrera, E., "A study on Arc-length-type Methods and Their Operation Failures Illustrated by a Simple Model", Computers and Structures, Vol. 50(2), 1994, pp. 217-229.

79. Galerkin, B. G., "Rods and Plates: Series Occurring in Various Questions Concerning the Elastic Equilibrium of Rods and Plates". Vestnik Inzhenerov I Tekhnikov (Petrograd), Vol. 19, 1915, pp. 897-908 (in Russian) (Cross referenced from many other references).

80. Vol'mir, A. S., *Stability of Deformable Systems*, Nauka, Moscow, 1967 (Cross referenced from many other references).

81. Karman, Th. and Tsien, H. S., "The Buckling of Thin Cylindrical Shells Under Axial Compression", Journal of the **Aeronautical** Sciences, Vol. 8(8), 1941, pp. 303-312.

82. Grigolyuk, E. I. and Kabanov, V. V., *Stability of Shells*, Nauka, Moscow, 1978 (Cross referenced from many other references).

83. Riks, E., “Some Computational Aspects of Stability Analysis of Nonlinear Structures”, Computer Methods in Applied Mechanics and Engineering, Vol. 47, 1984, pp. 219-259.

84. Ramm, E., “Strategies for Tracing Non-Linear Responses Near Limit Points”, Non-linear Finite Element Analysis in Structural Mechanics, Springer, New York, 1981.

85. Sze, K. Y., Liu, X. H., and Lo, S. H., “Popular Benchmark Problems for Geometric Non-Linear Analysis of Shells”, Finite Elements in Analysis and Design, Vol. 40, 2004, pp. 1551-1569.

86. Andrade, L.G., Awruch, A.M. and Morsch, I.B., “Geometrically Nonlinear Analysis of Laminate Composite Plates and Shells Using the Eight-Node Hexahedral Element With One-Point Integration”, Composite Structures, Vol. 79, 2007, pp. 571–580.

87. Han, S.-C., Tabiei, A. and Park, W.-T., “Geometrically Nonlinear Analysis of Laminated Composite Thin Shells Using a Modified First-Order Shear Deformable Element-Based Lagrangian Shell Element”, Composite Structures, Vol. 82, 2008, pp. 465–474.

88. Pradyumna, S., Nanda, N. and Bandyopadhyay, J. N., “Geometrically Nonlinear Transient Analysis of Functionally Graded Shell Panels Using a Higher-Order Finite Element Formulation”, Journal of Mechanical Engineering Research, Vol. 2(2), March 2010, pp. 39-51.

89. Chang, S. C. and Chen, J.-J., "Effectiveness of Linear Bifurcation Analysis for Predicting the Nonlinear Stability Limits of Structures", International Journal for Numerical Methods in Engineering, Vol. 23, 1986, pp. 831-846.

90. Li, L.-Y., "Improved nonlinear buckling analysis of structures", Computational Mechanics Vol. 6, 1990, pp. 457-462.

91. Bathe, K.-J., *Finite Element Procedures*, Prentice Hall, New Jersey, 1996.

92. Batdorf, S. B., "A Simplified Method of Elastic Stability Analysis for Thin Cylindrical Shells", NACA RT-No. 874, Washinton DC, USA, 1947.

93. Croll, J. G. A., "Towards Simple Estimates of Shell Buckling Load", Der Stahlbau, 1975 (Cross referenced from many other references).

94. Brush, D. O., "Prebuckling rotations and Cylindrical Buckling Analysis", Proceedings of the Third Engineering Mechanics Division Specialty Conference, Austin, TX, USA, Sept. 17-19, 1979.

95. Almroth, B. O. and Brogan, F. A., "Bifurcation Buckling as an Approximation of the Collapse Load for General Shells", AIAA journal, Vol. 10(4), April 1972, pp. 463- 470.

96. Brendel, B. and Ramm, E., "Linear and Nonlinear Stability Analysis of Cylincrical Shells", Computer and Structures, Vol. 12(4), 1980, pp. 549-558.

97. Leissa, A. W. *Vibrations of shells*, NASA SP-288, USA, 1973.

98. Love, A. E. H. "*A Treatise on the Mathematical Theory of Elasticity*", 3rd ED, Dover Publication, New York, USA, 1927.

99. Vlasov, V. Z., *General Theory of Shell and Its Application in Engineering*, NASA technical translation, USA, 1964.

100. Sanders Jr., J. L. “An Improved First Approximation Theory for Thin Shells”, NASA Report R-24, USA, 1959.

101. Koiter, W. T. “A Consistent First Approximation in General Theory of Thin Elastic Shells. The Theory of Thin Elastic Shells”, Proceedings IUTAM Symposium, Delft, North-Holland, Amsterdam, Netherlands, 1959.

102. Novozhilov, V. V., *Thin Shell Theory*, P. Noordhoff Ltd., Netherlands, 1964.

103. Bertholet, J. M., *Composite Materials - Mechanical Behavior and Structural Analysis*, Springer Verlag, New York, USA, 1999.

104. Jaunky, N. Norman, F. K. Jr. and Ambur, D. R. “Buckling Analysis of Anisotropic Variable-Curvature Panels and Shells”, Composite Structures, Vol. 43, 1999, pp: 321-329.

105. Zhang, Y. and Matthewst, F. L. “Initial Buckling of Curved Panels of Generally Layered Composite Materials”, Composite Structures, Vol. 1, 1983, pp: 3-30.

106. Wilkins, D. J. “Compression Buckling Tests of Laminated Graphite-Epoxy Curved Panels”, AIAA J., Vol. 13, April 1975, pp: 465-470.

107. Becker, M. L. “Analytical/Experimental Investigation of the Instability of Composite Cylindrical Panels”, MS Thesis, Wright-Patterson AFB, OH." Air Force Institute of Tech., USA, Dec. 1979.

108. Jaunky, N and Knight, Jr. NF., “An Assessment of Shell Theories for Buckling of Circular Cylindrical Laminated Composite Panels Loaded in Axial Compression”, International Journal of Solids and Structures, Vol. 36, 1999, pp: 3799-3820.

109. Morley LSD. An Improvement on Donnell’s Approximation for Thin-Walled Circular Cylinders. Quart. J. Mech. and Appl. Math., Vol. 12, 1959, pp: 89-99.

110. Loo TT. An Extension of Donnell's Equation for a Circular Cylindrical Shell. J. Aero. Sci., Vol. 24, 1957, pp: 390-391.

111. Akhlaque-E-Rasul S and Ganesan R. Buckling Response of Tapered Curved Composite Plates Based on Classical Shell Theories. Proceedings of ICCM-17 Edinburgh, UK; IF3: 3, 2009.

112. Akhlaque-E-Rasul, S. and Ganesan, R., "The Compressive Response of Thickness-Tapered Shallow Curved Composite Plates Based on Classical Shell Theory", The Journal of Advanced Materials, in Press.

113. Akhlaque-E-Rasul S and Ganesan R. The Buckling Response of Tapered Curved Composite Plates-II. Proceedings of the American Society for Composites: Twenty-Fourth Technical Conference, Newark, DE, USA, September 15–17, 2009, CD-ROM—paper No: 09.

114. Akhlaque-E-Rasul, S. and Ganesan, R. (2010) "Buckling Analysis of Tapered Curved Laminates Using ANSYS". Paper has been accepted in the World Journal of Engineering.

115. Reddy, J. N., *Mechanics of laminated composite plates and shells: theory and analysis*, 2nd edition, CRC Press LLC, USA, 2004.

116. Akhlaque-E-Rasul, S., and Ganesan, R. "The compressive response of tapered curved composite plates". Proceedings of the American Society for Composites: Twenty-Fourth Technical Conference, Newark, DE, USA, September 15–17, 2009, CD-ROM- paper No: 10.

117. Lee, S. J., "Nonlinear Analysis of Smart Composite Plate and Shell Structures", Ph.D. Dissertation, Texas A&M University, USA, May 2004.

118. Kweon, J. H. and Hong, C. S., "Postbuckling Analysis of Composite Laminated Cylindrical Panels Under Axial Compression", AIAA Journal. Vol. 31(8), 1993, pp. 1535-1537.

119. Viscotchi F., "Aviation Operational Measures for Fuel and Emissions Reduction", Workshop, Bombardier Aircraft Panel, Montreal, Canada, Sept 20-21, 2006.

END